Analysis of proton exchange membrane fuel cell (PEMFC) design parameters by simulation using OpenFCST

by

David Caballero Flores

A thesis submitted in partial fulfillment of the requirements for the degree of

Master's Degree in Industrial Engineering by
Universitat Politècnica de Catalunya

Department of Mechanics Engineering

University of Alberta

Abstract

Improving proton exchange membrane fuel cells technology, together with hydrogen production and storage, can make these devices an important element in the energy transition puzzle. A multi-dimensional, non-isothermal, two-phase flow numerical full MEA model is used to simulate a real experiment. Once the results are validated, the same experimental model is used as a baseline to study the effect of parallel channel and current collector widths in the PEMFC behavior. Further, the performance response is also evaluated for different cathode catalyst layer compositions, varying the platinum and electrolyte loadings. A part from these concrete studies, the model response to an individual parameter variation is evaluated, under wet and dry conditions, for parameters such as oxygen dissolution rate and water sorption constants, thermal and electrical conductivities and contact angle in the different media inside the cathode. The results show that keeping the baseline cathode catalyst layer thickness, 3.75 μm, modifying channel widths to 0.13 cm and discretely through-plane grading the Pt/C content, the maximum power is increased by 15% with the same platinum loading when reactants are supplied with 90% relative humidity. In the case of 75%RH, the improving is around the 20% by just changing to 0.13 cm the channel width respect to the baseline.

To my parents,

they definitely deserve this line.

The proper use of science is not to conquer nature but to live in it.

– Barry Commoner.

Acknowledgements

First of all, I want to thank Marc Secanell for giving me the opportunity, guiding my effort and catching me with his enthusiasm. Further, I want to thank Jie Zhou for his indications about his mathematical model and OpenFCST. Without doubt, I need to mention here the full Energy Systems Design Laboratory team (ESDLab) and thank them for welcoming me as well.
Finally, I would also like to thank the reader and all the people interested in research areas with the aim of making possible the energy transition.

Table of Contents

List of Tables

List of Figures

Nomenclature

$\bar{H}_i$ Specific enthalpy of spices i

A Superficial area

$a(r)_c$ Liquid invaded cross-section area per unit volume of cylindrical pores

a_{lv} Gas-liquid interfacial surface area per unit of volume, $[cm^2/cm^3]$

a_{max} Total cross-section area per unit volume

$a_{v,\text{wall}}$ Lateral area per unit volume

ACL_{thk} Anode catalyst layer thickness, $[\mu m]$

c_g Total gas mixture concentration

CCL_{thk} Cathode catalyst layer thickness, $[\mu m]$

CCM_{thk} Catalyst-coated membrane thickness, $[\mu m]$

CL_{thk} Catalyst layer thickness, $[\mu m]$

D_{λ}^{eff} Sorbed water membrane diffusion coeficient

D_{T}^{eff} Thermo-osmosis membrane diffusion coeficient

$D_{i,j}^{eff}$ Effective diffusivity of spices i in j

D_{ij} Binary molecular diffusion coefficient

e Thickness, $[\mu m]$

$ECSA_{mass}$ Electrochemical active surface area per unit of mass of Pt; $[\frac{cm^2_{Pt}}{g_{Pt}}]$

$ECSA_V$ Electrochemical active surface area per unit of volume; $[\frac{cm^2_{Pt}}{cm^3_{CL}}]$

EW Equivalent weight of the ionomer

F_{HI} Hydrophilic pores volume fraction

F_{HO} Hydrophobic pores volume fraction

$f_{i,k}$ Partial contribution of sub-distribution functions from mode k in either hydrophilic or hydrophobic network (i)

G_{thk} Gasket thickness, $[\mu m]$

GDL_{thk} Gas diffusion layer thickness, $[\mu m]$

H_l Molar enthalpy of liquid water

H_{lv} Exchange molar latent heat in vaporization or condensation of water, $[kJ/mol]$

j Volumetric current density, $[A/cm^3]$

J_l Liquid water flux

k_g Gas permeability, $[cm^2]$

k_{BT} Constant capillary pressure current flux boundary condition $[Pa]$

k_c Volumetric condensation rate constant, $[mol \cdot cm^{-2}\ s^{-1}]$

k_e Volumetric evaporation rate constant, $[mol \cdot cm^{-2}\ s^{-1}]$

$k_{g,HI}$ Gas permeability corresponding to unfilled hydrophilic pores

$k_{g,HO}$ Gas permeability corresponding to unfilled hydrophobic pores

k_{H_2} Hydrogen dissolution rate constant, $[m/s]$

k_l Liquid permeability

k_{O_2} Oxygen dissolution rate constant, $[m/s]$

k_{rg} Relative gas permeability

k_{rl} Relative liquid permeability

k_{sat} Absolute permeability

K_{sorp} Water sorption time constant, $[1/s]$

L Length of the cylindrical pores, estimated as $4r$

l Length in the conduction direction, $[\mu m]$

L_{thk} Lamination thickness, $[\mu m]$

M_{H2O} Molar mass of water

M_i Molar mass of species

MPL_{thk} Micro-porous layer thickness, $[\mu m]$

n Characteristic exponent; 3.5 and 2.5 in tne through-plane and in-plane direction, respectively

$p^{\mathrm{sat}}(T)$ Uncorrected saturated vapour pressure of water

$p_{\mathrm{K}}^{\mathrm{sat}}(p_c, T)$ Effective saturated vapour pressure in a capillary

p_i i pressure. l; liquid water, g; air pressure, v; vapour pressure, $[Pa]$

P_{abs} Absolute pressure

p_{BT} Breakthough capillary pressure at GDL/channel interface, $[Pa]$

PEM_{thk} Proton exchange membrane thickness, $[\mu m]$

Pt/C Platinum on carbon ratio, [%]

Pt_{load_S} Platinum superficial loading, $[g_{Pt}/cm^2_{CL}]$

Pt_{load_V} Platinum volumetric loading, $[g_{Pt}/cm^3_{CL}]$

R_g Universal gas constant

R_i Electrical or thermal resistance in the i-media

R_c Contact electrical or thermal resistance

r_c Critical radius

R_{eq} Equivalent electrical or thermal resistance

$r_{i,k}$ Characteristic pore size of sub-distribution from mode k

S Saturation

s Local saturation

S_x e x h; area perpendicular to the conduction direction

$s_{i,k}$ Standard desviation

T Temperature, $[K]$

u_g Gas velocity based on Darcy's law

V_T Total pore volume

V_p Void or porous part volume

V_s Solid part volume

V_{tot} Total physical volume

$w_{electrolyte}$ Electrolyte weight loading fraction, [%]

x_i Molar fractions of spices i

$\mathbf{N}_i$ Total, convective and diffusive flux of spices i

Greek letters

ρ_g Density of water vapour, $[g/cm^3]$

γ	Exponent which accounts for the loss of mass transport due to liquid water
κ_j^i	i-direction thermal conductivity in the j-media. IP; in-plane, TP; through plane, $[W/cm \cdot K]$
λ_{eq}	Ionomer equilibrium water content at a given water vapor
λ_{PSD}	PSD porous interconnectivity
μ_i	Dynamic vicsosity of spices i
ϕ_m	Electrolyte potential
ϕ_s	Electronic potential
ϕ_{HI}	Hydrophilic contact angle, $[^\circ]$
ϕ_{HO}	Hydrophobic contact angle, $[^\circ]$
ρ_{dry}	Density of the dry polymer, $[g/cm^3]$
ρ_i	Density of i, $[g/cm^3]$
σ	Electrical conductivity, $[S/cm]$
σ_m^{eff}	Effective ionic conductivity
σ_s^{eff}	Effective electronic conductivity
σ_j^i	i-direction electrical conductivity in the j-media. IP; in-plane, TP; through-plane, $[S/cm]$
τ	Turtuosity
ε_V^{cl}	Volume fraction of void space in CL
ε_i	i-volume fraction
ε_o	Porosity
$\varepsilon_{void}^{'}$	Real void volume fraction in the catalyst layer highest saturated area.

Acronyms

ACL Anode Catalyst Layer. 19

CCL Cathode Catalyst Layer. 19

CCM Catalyst-Coated Membrane. 20

CL Catalyst Layer. 16

ECSA Electrochemical Active Surface Area. 19

GDL Gas Difussion Layer. 3

HI Hydrophilic. 19

HO Hydrophobic. 19

ICCP Ionomer Covered Catalyst Particle. 28, 74

IJP Ink-Jet Printing. 28

IPA Isopropanol. 20

MEA Membrane Electrode Assembly. 3

MIP Mercury Intrusion Porosimetry. 24

MPL Micro-Porous Layer. 4

OOR Oxygen Reduction Reaction. ix

PEM Proton Exchange Membrane or Polymer Electrolytre Membrane. 3

PEMFC Proton Exchange Membrane Fuel Cell or Polymer Electrolyte Membrane Fuel Cell. ii

PG Propylene Glycol. 20

PSD Porous Size Distribution. 12

PTFE Polytetrafluoroethylene. 21

RH Relative Humidity. 18

Chapter 1

Introduction

1.1 Motivation

Global energy consumption systematically increases every year. As its environmental impact is a world wide concerning topic, the sustainable energy production and consumption has emerged as a wide research area. Hydrogen fuel cells appeared as an alternative to the internal combustion engine that has only water vapor as a direct by-product. The hydrogen fuel can be produced from, among others, clean sources as solar energy however, it is fair to remark that currently most H_2 is produced from steam methane reforming leading to CO_2 emissions along the hydrogen fuel production process. However, the H_2 obtaining process is not the topic of this Thesis. Taking into account the actual zero local emission advantage of the hydrogen fuel cells –e.g., improving air quality in large populated areas or indoor spaces, the goal of this Thesis is to increase the knowledge about how different design parameters affect the fuel cell response. Thus, enhance and ease future improvements in the performance-cost ratio for polymer electrolyte fuel cells (PEMFC's) devices in order to make them more competitive in front of other less sustainable substitute products.

One of the most important parts of a PEMFC is the cathode catalyst layer, where the limiting reaction takes part. Its platinum content makes the catalyst layer, together with the bipolar plates mechanical channel process, significant components in the final cost. Due to its impact on performance and cost issue, the catalyst layer and the channel geometry are the main focus of this study.

1.2 Proton Exchange Membrane Fuel Cell (PEMFC)

Proton exchange membrane fuel cells are energy conversion devices that produce electricity via an electrochemical process when fed by hydrogen and have only water vapor as a by-product. In some respects, its operation principle is similar to a conventional battery except that the reactants are stored outside the cell. Therefore, the capacity of the device is limited only by the availability of the fuel and oxidant supply and not by the cell design. For this reason, fuel cells are rated by their power output (kW) rather than by their capacity (kWh). The present section will introduce the basic concepts of these devices, also called polymer electrolyte membrane fuel cells, PEMFC henceforth.

1.2.1 Overview

The PEMFC was developed for the first time in the United States in 1960s. The main purpose of the design was to be used in a manned spacecraft by NASA[1]. The solid proton exchange membrane that gives the name to the device was made of electrolytes based on polymers such as polyethylene or polystyrene. However, in 1967, a novel fluorinated polymer based on a polytetrafluoroethylene (PTFE) structure was introduced in the marked under the trademark Nafion^{TM}. Nowadays, this material is simply referred as Nafion and has become an industry standard for cells operating at temperatures below 80^{o}C due to its necessity to be hydrated for a better protonic conductivity.

The PEMFC is able to function in any orientation. They are compact with high power densities and very robust and suitable for use in road vehicles and as a portable power source for electrical and electronic applications. Its technology is being developed mainly for transport applications, as well as for stationary fuel-cell applications and portable fuel-cell applications.

[1]National Aeronautics and Space Administration

1.2.2 PEMFC basic components

Throughout this thesis, the name and concept of different components in the fuel cell appears in the explanations. In order to ease the future comprehension and consultation, this section briefly summarizes the basic components and its function in a PEMFC. Some of them can be identified in Figure 1.2, that shows an overview of how a PEMFC works, complementing the explanation in Section 1.2.3.

1. **Proton exchange membrane (PEM)** or just membrane, is made out of electrolyte material –e.g., Nafion. This membrane allows the proton flux from anode to cathode and bidirectional flux of water vapor while avoiding electron and gas exchange between anode and cathode.

2. **Bipolar plates** are responsible for transporting the fuel (hydrogen) and the reactant (oxygen) throughout the fuel cell via the gas channels. Further, bipolar plates are responsible for collecting the electrons in the anode and delivering them to the cathode. The heat produced in the PEMFC is also transported to the environment and to the cooling section of the stack through the bipolar plates.

3. **Gas channels** are small grooves made by engraving or milling the bipolar plate surface. Their responsibility is to transport the fuel and reactant throughout the cell. Gas channels also play an important role in water management by controlling the fuel and reactant pressure drop. There are different types of gas channel geometries. Each generate a different flow field through the bipolar plates. Two examples of gas channel geometries, parallel and serpentine, are represented in Figure 1.1.

4. **Gas diffusion layers (GDLs)** have several functions. First of all, they are responsible for the fuel and reactant transport from the gas channels to the catalyst layers (where the reactions take place). Further, they are responsible for the electron transport between the catalyst site and the bipolar plates and also provide structural support to the MEA. Finally,

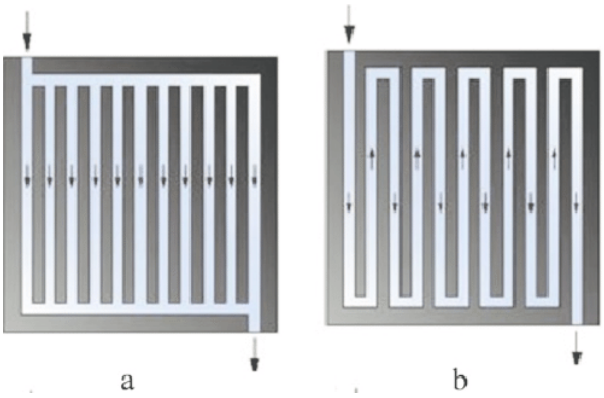

Figure 1.1: Different flow fields in PEMFC depending on channel configuration: (a) parallel channels, (b) serpentine channels. Reproduced from [2].

GDLs are also the transport media of the water out of the catalyst layer. Because of its functions, GDLs are usually highly porous composites made of an electron conducting material such as carbon fibers.

5. **Micro porous layers (MPLs)** is a porous thin layer fabricated by intermixing a hydrophobic agent –i.e., PTFE[2], with carbon black and located between the catalyst layer (CL) and gas diffusion layer (GDL). It is known that MPL improves the fuel cell performance, especially under wet conditions.

6. **Catalyst layers (CL)** are the place where the reactions occur inside the PEMFCs. CLs are porous media layers made out of carbon black supporting platinum particles and mixed together with an electrolyte. Its mixed composition is due to the multipurpose of this layer, responsible of promoting the reaction kinetics, transporting fuel and reactants, electrons and protons and also transporting water to the GDL or membrane.

7. **Membrane electrode assembly (MEA).** It is the assembly formed by two GDLs, two CLs and the PEM.

8. **Gaskets** are located between the bipolar plates and MEA. They ensure a correct compression when stacking and minimize the fuel potential leaks.

[2]Polytetrafluoroethylene.

The gasket thickness determines how much the flow fields are allowed to pinch into the electrode.

1.2.3 Operating principles

The overall reaction in the PEMFC results as the hydrogen combustion reaction that has water as a final product:

$$2H_2 + O_2 \rightarrow 2H_2O + heat$$

However, in a PEMFC, the fuel combustion reaction is divided in two separate steps in order to allow for the collection of electrons and production of electrical current in the process. These reactions are hydrogen oxidation and oxygen reduction. Both reactions are separated from each other with a proton exchange membrane that allows the proton but not the electron flux from the anode to the cathode.

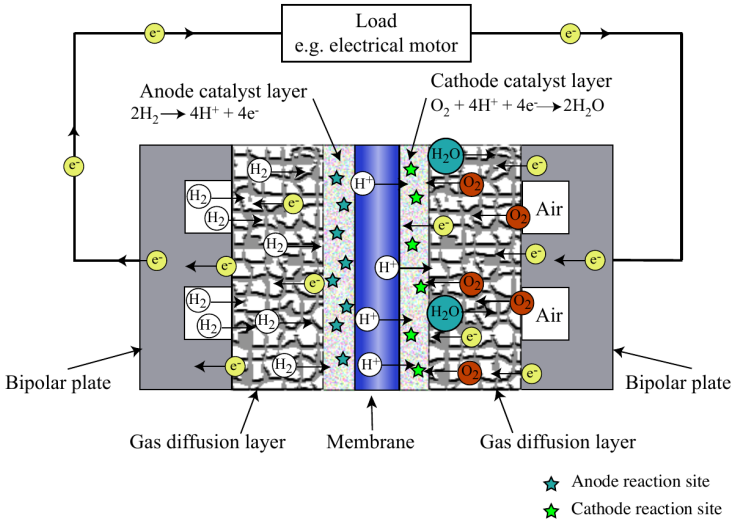

Figure 1.2: Schematic showing the various layers in a PEMFC and the main transport processes and electrochemical reactions. Figure from [4].

The hydrogen oxidation reaction occurs at the anode catalyst layer. In this process, the hydrogen is broken down into protons (H^+) and electrons (e^-) following the next chemical reaction:

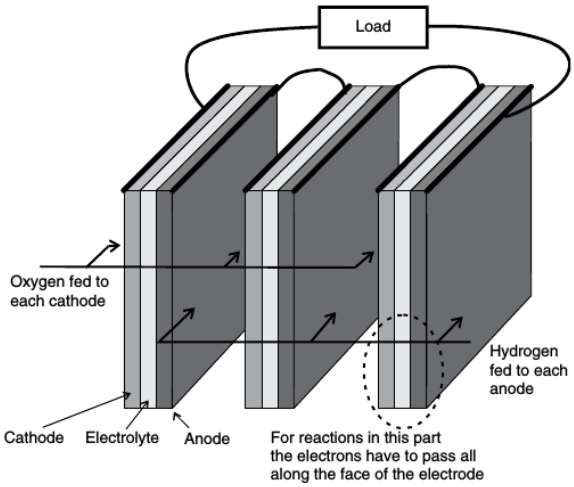

Figure 1.3: Three-cell stack schematic. The anode of one cell is connected to the cathode of its neighbor. Figure from [3].

$$2H_2 \rightarrow 4H^+ + 4e^-$$

While the produced electrons are collected by the bipolar plates and transported by an external electrical system to produce DC current, the protons are transported through the PEM to the cathode side. Once reached the cathode catalyst layer, the protons and the electrons take part in the oxygen reduction reaction occurring in the cathode catalyst layer as follows:

$$O_2 + 4H^+ + 4e^- \rightarrow 2H_2O$$

1.2.4 Stacking process

A fuel cell produces a low voltage, i.e., less than 1V. To build up the voltage to higher levels, a bunch of fuel cells are electrically connected in series to form a stack. The stack voltage is controlled by the number of connected fuel cells. Figure 1.3 shows a schematic of a three-cell stack electrically connected in series; alternatively anode and cathode. This connexion is showed as a wire in the schematic. However, as shown in Figure 1.4, this connection is actually done through the bipolar plates responsible, among others, for the electron transport through the stack.

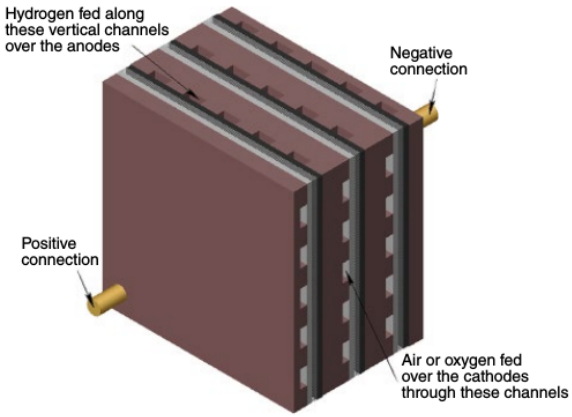

Figure 1.4: Three-cell stack. Figure from [3].

In this Thesis, a single cell is studied. However, the process of compressing the MEA between the bipolar plates is referenced as stacking process. This can be understood as a single cell stack.

1.3 Background, state of the art and objective

In his dissertation, [4], Marc Secanell contributed in 2007 with an open source computational modeling framework for fuel cell analysis and optimization called OpenFCST. Using the original OpenFCST framework and latter improvements implemented by the *Energy Systems Design Laboratory*[3] team, Jie Zhou et. al., [5] and [6], developed in 2017 a multi-dimensional (2D), non-isothermal, two-phase flow mathematical model for a full MEA. Its model is able to predict the local water saturation and its consequences in mass transport. It has been used to study the role of the microporous layer in improving polymer electrolyte fuel cell performance; [1].

The cathode catalyst layer has been widely studied and optimized in the literature. Centibas et al. [7] made a bidirectionally-graded platinum, electrolyte and carbon loading distribution optimization in the catalyst layer. Z.Jie et al. [8] studied also the CL graded composition. In this case, the study is fo-

[3]ESDLab. Department of Mechanical Engineering. Faculty of Engineering. University of Alberta.

cused on unidirectionally electrolyte (Nafion) graded composition along the catalyst layer. Secanell et al. [9] reported a multi-variable optimization that also include the platinum loading as design variable.
The channel and land widths were also numerically studied in 2007 by M.Muthukumar et. al., [10], relating the results with the water management and performance response of the cell.

All these previous modeling studies were based on a PEMFC model that contained less detailed physics than the current model in OpenFCST. Therefore, this Thesis aims at using OpenFCST's new model to reproduce these studies in order to analyze the impact of the more detailed physical description.

1.4 Contributions

The main contributions reported in this work are achieved in different phases of the study, from the modeling to the results

- a sensitivity study is reported for different parameters that define the modeled PEMFC in the non-isothermal two-phase flow mathematical model.
- an experimental PEMFC is modeled and its model is validated by comparing the solution with empirical results in order to establish a reliable baseline for futures studies.
- some topics treated in this Thesis, as the cathode catalyst layer platinum and electrolyte loading, have been previously studied and reported in the literature. However, it is the first time that is is done with a full MEA two-phase flow model as the one used for the present work.
- by studying the effect of channel and current collector widths, together with the graded platinum distribution inside the CCL affectation, conclusions about the reactants humidity conditions and channel geometry are reported.

Chapter 2

Theory

2.1 Mathematical model

A multi-dimensional, non-isothermal, two-phase numerical full MEA model, essentially developed by J.Zhou et. al., [5], and extended in 2017, [1], to include the gas pressure transport and gas convection, is used for the purpose of this thesis. The model is already implemented in the OpenFCST, the computational aided simulation framework developed originally by M. Secanell in his dissertation, ref. [4].

2.1.1 Assumptions

1. The fuel cell is at steady-state.
2. Liquid water transport is dominated by surface tension.
3. The representative element volume (REV) contains homogeneous hydrophilic and hydrophobic pore-networks.
4. Gas and liquid are considered incompressible.
5. The membrane is impermeable to liquid water.
6. Phase change in the pore-network is driven by the gradient between partial pressure of water vapor and saturation water vapor pressure.
7. The two-dimensional computational domain contains an anode GDL, an anode MPL, an anode CL, an PEM, a cathode CL, a cathode MPL and a

cathode GDL. Symmetry is used to reduce the domain to half the width of gas channel and bipolar plate.

8. The oxygen reduction reaction (ORR) is characterized by the double trap kinetic model described in ref. [11].

9. The hydrogen oxidation reaction (HOR) is characterized by the dual path kinetic model described in ref. [12].

2.1.2 Governing equations

The overall system of equations is:

$$\nabla \cdot \left(c_g \; D^{\text{eff}}_{O_2,N_2} \nabla x_{O_2}\right) - \nabla \cdot (c_g x_{O_2} \mathbf{u}_g) = S_{O_2} \ ,$$

$$\nabla \cdot \left(c_g \; D^{\text{eff}}_{H_2O(vapor),N_2 \text{ or } H_2} \nabla x_{H_2O(vapor)}\right) - \nabla \cdot (c_g x_{H_2O} \mathbf{u}_g) = S_w \ ,$$

$$\nabla \cdot \left(\sigma_m^{\text{eff}} \nabla \phi_m\right) = S_{H^+} \ ,$$

$$\nabla \cdot \left(\sigma_s^{\text{eff}} \nabla \phi_s\right) = S_{e^-} \ ,$$

$$\nabla \cdot \left(n_d \frac{\sigma_m^{\text{eff}}}{F} \nabla \phi_m + \frac{\rho_{\text{dry}}}{EW} D_\lambda^{\text{eff}} \nabla \lambda + \frac{D_T^{\text{eff}}}{M_{H_2O}} \nabla T\right) = S_\lambda$$

$$\nabla \cdot \left(k^{\text{eff}} \nabla T\right) + \nabla \cdot \left(\sum \bar{H}_i \mathbf{N}_i\right) = S_T \ ,$$

$$\nabla \cdot \left(\frac{\rho_l k_l}{\mu_l} \nabla p_l\right) = S_{liquid} \ ,$$

$$\nabla \cdot \left(\frac{\rho_g k_g}{\mu_g} \nabla p_g\right) = S_{gas}$$

Where,

$$\mathbf{N}_i = c_g x_i \mathbf{u}_g - c_g D_{i,j}^{\text{eff}} \nabla x_i$$

The capillary pressure, p_c, is defined as:

$$p_c = p_l - p_g$$

2.1.3 Source terms

The source or sink terms for the governing equations are given in Tables 2.1 and 2.2.

Table 2.1: Source terms in ACL and PEM for governing equations

Parameters	ACL	PEM
S_{O2}		
S_w	$S_{H2O(\text{evap/cond})} - S_\lambda$	
S_{gas}	$-M_{H2O} S_{H2O(\text{evap/cond})} + \frac{j}{2F} M_{H2} + S_\lambda M_{H2O}$	
S_{liquid}	$M_{H2O} S_{H2O(\text{evap/cond})}$	
S_{H^+}	$-j$	
S_{e^-}	j	
S_λ	$-k_{O_2} \frac{\rho_{\text{dry}}}{EW} (\lambda_{eq} - \lambda)$	
S_T	$H_{lv} S_{H2O(\text{evap/cond})} - j(\phi_s - \phi_m - E_{HOR}) + \frac{j}{2F}(T(1 - f_{ORR})\Delta \overline{S}_{\text{overall}})$	$-\sigma_m^{\text{eff}}(\overrightarrow{\nabla}\phi_m \cdot \overrightarrow{\nabla}\phi_m)$
	$-\sigma_m^{\text{eff}}(\overrightarrow{\nabla}\phi_m \cdot \overrightarrow{\nabla}\phi_m) - \sigma_s^{\text{eff}}(\overrightarrow{\nabla}\phi_s \cdot \overrightarrow{\nabla}\phi_s) - k_{O_2} \frac{\rho_{dry}}{EW}(\lambda_{eq} - \lambda)\bar{H}_{\text{sorption}}$	

Table 2.2: Source terms in GDL, MPL and CCL for governing equations

Parameters	GDL,MPL	CCL
S_{O2}		$\frac{j}{4F} M_{O2}$
S_w	$S_{H2O(\text{evap/cond})}$	$S_{H2O(\text{evap/cond})} - S_\lambda$
S_{gas}	$-M_{H2O} S_{H2O(\text{evap/cond})}$	$-M_{H2O} S_{H2O(\text{evap/cond})} + \frac{j}{4F} M_{O2} + S_\lambda M_{H2O}$
S_{liquid}	$M_{H2O} S_{H2O(\text{evap/cond})}$	$M_{H2O} S_{H2O(\text{evap/cond})} - \frac{j}{2F} M_{H2O}$
S_{H^+}		
S_{e^-}		$-j$
S_λ		$-k_{O_2} \frac{\rho_{dry}}{EW}(\lambda_{eq} - \lambda)$
S_T	$H_{lv} S_{H2O(\text{evap/cond})}$	$H_{lv} S_{H2O(\text{evap/cond})} + j(\phi_s - \phi_m - E_{ORR}) + \frac{j}{2F}(T f_{ORR} \Delta \overline{S}_{\text{overall}})$
		$-\sigma_m^{\text{eff}}(\overrightarrow{\nabla}\phi_m \cdot \overrightarrow{\nabla}\phi_m) - \sigma_s^{\text{eff}}(\overrightarrow{\nabla}\phi_s \cdot \overrightarrow{\nabla}\phi_s) - k_{O_2} \frac{\rho_{\text{dry}}}{EW}(\lambda_{eq} - \lambda)\bar{H}_{\text{sorption}}$

The volumetric current density, j, is computed using the ionomer coated catalyst particle (ICCP) model [13]. Figure 2.1 represents the ICCP idealized structure where oxygen is assumed to first dissolve into the ionomer film, and then diffuse through the film to the surface of the platinum that covers the carbon particle. It then reacts with the platinum.

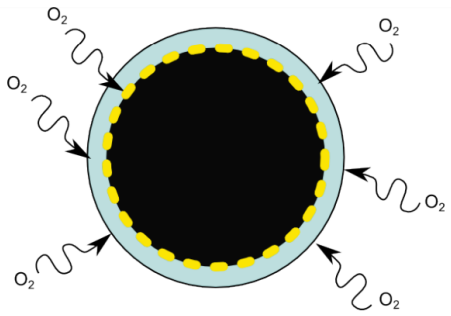

Figure 2.1: Figure reproduced from [13]. Diagram of ICCP. The assumed structure is a spherical carbon particle (black) with an even distribution of platinum on the exterior carbon surface (yellow), surrounded by a thin ionomer film (green).

The water source term, $S_{H_2O(evap/cond)}$, governed by the evaporation-condensation phenomena is defined as follows:

$$S_{H_2O(evap/cond)}(p_c,T) = \begin{cases} k_e a_{lv}\left(\dfrac{p_v - p_{\mathrm{K}}^{\mathrm{sat}}(p_c,T)}{p_{\mathrm{K}}^{\mathrm{sat}}(p_c,T)}\right), & \text{if } \; p_v > p_{\mathrm{K}}^{\mathrm{sat}}(p_c,T) \\ k_c a_{lv}\left(\dfrac{p_v - p_{\mathrm{K}}^{\mathrm{sat}}(p_c,T)}{p_{\mathrm{K}}^{\mathrm{sat}}(p_c,T)}\right), & \text{otherwise} \end{cases}$$

Where $p_{\mathrm{K}}^{\mathrm{sat}}(p_c,T)$, is determined by considering the Kelvin effect and the Young-Laplace equation as follows:

$$p_{\mathrm{K}}^{\mathrm{sat}}(p_c,T) = p^{\mathrm{sat}}(T) exp\left(\frac{p_c M_{H2O}}{R_g T \rho_g}\right) \tag{2.1}$$

The thermal equation has an additional term to account for the enthalpy transport of liquid water:

$$f(p_c) = -\nabla \cdot (H_l J_l) \tag{2.2}$$

2.1.4 Internal equations

Internal equations are included in the model in order to define the effective properties used in liquid and gas transport equations.

Pore size distribution

The model uses PSD and wettability as input parameters for estimate the transport properties such as saturation, absolute permeability, gas-liquid in-

terfacial surface area and relative permeability. The PSD is divided into two individual log-normal distributions over the pore sizes representing the hydrophilic and hydrophobic pore networks respectively.

The expanded PSD model takes the form:

$$\frac{dX}{dr} = \left\{ F_{\mathrm{HI}} \sum_k \left[\frac{f_{\mathrm{HI},k}}{r\, s_{\mathrm{HI},k}\sqrt{2\pi}} E_{\mathrm{HI},k} \right] + F_{\mathrm{HO}} \sum_k \left[\frac{f_{\mathrm{HO},k}}{r\, s_{\mathrm{HO},k}\sqrt{2\pi}} E_{\mathrm{HO},k} \right] \right\} \tag{2.3}$$

where $E_{\mathrm{HI},k}$ and $E_{\mathrm{HO},k}$ are:

$$E_{\mathrm{HI},k} = \exp\left(- \left[\frac{\ln(r) - \ln(r_{\mathrm{HI},k})}{s_{\mathrm{HI},k}\sqrt{2}} \right]^2 \right) \tag{2.4}$$

$$E_{\mathrm{HO},k} = \exp\left(- \left[\frac{\ln(r) - \ln(r_{\mathrm{HO},k})}{s_{\mathrm{HO},k}\sqrt{2}} \right]^2 \right) \tag{2.5}$$

Saturation

Saturation is estimated by integrating the contributions from all pores in the porous media as follows:

$$S = S_{\mathrm{HI}} + S_{\mathrm{HO}} = \int_0^{r_{c,\mathrm{HI}}} \frac{dX(r)_{\mathrm{HI}}}{dr}\, dr + \int_{r_{c,\mathrm{HO}}}^{\infty} \frac{dX(r)_{\mathrm{HO}}}{dr}\, dr \tag{2.6}$$

The critical radius, r_c, is estimated using the capillary pressure and Washburn equation [14]. The limit of integration takes into account that, in a hydrophilic media, small pores would be invaded by water first, followed by the larger pores. The opposite occurs in a hydrophobic material. Analytically solving the integral above, an explicit equation for saturation is obtained:

$$\begin{aligned} S = {} & F_{\mathrm{HI}} \sum_k \frac{f_{\mathrm{HI},r,k}}{2} \left[1 + \mathrm{erf}\left(\frac{\ln(r_{c,\mathrm{HI}}) - \ln(r_{\mathrm{HI},k})}{s_{\mathrm{HI},k}\sqrt{2}} \right) \right] \\ & + F_{\mathrm{HO}} \sum_k \frac{f_{\mathrm{HO},k}}{2} \left[1 - \mathrm{erf}\left(\frac{\ln(r_{c,\mathrm{HO}}) - \ln(r_{\mathrm{HO},k})}{s_{\mathrm{HO},k}\sqrt{2}} \right) \right] \end{aligned} \tag{2.7}$$

Permeability

Absolute permeability The absolute permeability is calculated using Hagen-Poiseuille equation and integrating the contributions from all pores in the layer:

$$k_{\text{sat}} = \left[\frac{\varepsilon_o}{\lambda_{\text{PSD}}}\right]^2 \int_0^\infty \frac{r^2}{8}\frac{dX}{dr}dr \tag{2.8}$$

Combining with previous equation (2.8) and solving the integrals, the absolute permeability in a fully saturated porous medium is:

$$k_{\text{sat}} = \frac{1}{8}\left[\frac{\varepsilon_o}{\lambda_{\text{PSD}}}\right]^2 \sum_k r_k^2 f_k \, \exp\left(-2\, s_k^2\right) \tag{2.9}$$

Relative liquid permeability The relative liquid permeability is determined as the ratio between the effective liquid permeability and the absolute permeability as follows:

$$k_{r,L} = \frac{1}{8k_{sat}}\left[\frac{\varepsilon_o\, S}{\lambda_{\text{PSD}}}\right]^2 \left[\int_0^{r_{c,\text{HI}}} r^2 \frac{dX(r)_{\text{HI}}}{dr}dr + \int_{r_{c,\text{HO}}}^\infty r^2 \frac{dX(r)_{\text{HO}}}{dr}dr\right] \tag{2.10}$$

Relative gas permeability The relative gas permeability, defined as the ratio of gas permeability and absolute permeability, is estimated using,

$$k_{rg} = \frac{k_{g,\text{HI}} + k_{g,\text{HO}}}{k_{\text{sat}}}$$

$$= \frac{1}{8k_{\text{sat}}}\left[\frac{\varepsilon_o\,(1-S)}{\lambda_{\text{PSD}}}\right]^2 \left[\int_{r_{c,\text{HI}}}^\infty r^2 \frac{dX(r)_{\text{HI}}}{dr}dr + \int_0^{r_{c,\text{HO}}} r^2 \frac{dX(r)_{\text{HO}}}{dr}dr\right] \tag{2.11}$$

Liquid-Gas Interfacial Surface Area

To account for the possibility of having a common area for liquid and gas between filled and empty capillaries, a probability density function is defined:

$$\text{P}_\text{b} = \frac{a(r_c)_c}{a_{\max}}\left(1 - \frac{a(r_c)_c}{a_{\max}}\right) \tag{2.12}$$

$$a_{\max} = \sum_k \frac{f_k \exp\left(\frac{s_k^2}{2}\right)}{4\, r_k} \tag{2.13}$$

The probability function forces the liquid-gas interfacial surface area to be zero either when the layer is fully dry or saturated, whereas when the layer is

partially saturated, there exists a maximum value for the interfacial surface area.

The cross sectional area per unit volume is determined by taking the ratio between the cross-section area (πr^2) of the pore and its volume ($\pi r^2 L$):

$$a(r_c)_c = \frac{a(r_c)}{V_T} = \int_0^{r_{c,\mathrm{HI}}} \frac{1}{L}\frac{dX_{\mathrm{HI}}}{dr}dr + \int_{r_{c,\mathrm{HO}}}^{\infty} \frac{1}{L}\frac{dX_{\mathrm{HO}}}{dr}dr \tag{2.14}$$

The overall expression for the interfacial surface area per unit volume is:

$$a_v(r_c) = \mathrm{P_b} \cdot a_{\max} \tag{2.15}$$

Diffusion

The average capillary radius, average Knudsen radius, is estimated as follows:

$$r_{\mathrm{Kn}} = 2\frac{V(r_c)}{a_{\mathrm{wall}}(r_c)} = 2\frac{\int_{r_{c,\mathrm{HI}}}^{\infty} \frac{1}{V_T}\frac{dV_{\mathrm{HI}}(r_{c,\mathrm{HI}})}{dr}dr + \int_0^{r_{c,\mathrm{HO}}} \frac{1}{V_T}\frac{dV_{\mathrm{HO}}(r_{c,\mathrm{HO}})}{dr}dr}{\int_{r_{c,\mathrm{HI}}}^{\infty} \frac{1}{V_T}\frac{da_{\mathrm{wall,HI}}(r_{c,\mathrm{HI}})}{dr}dr + \int_0^{r_{c,\mathrm{HO}}} \frac{1}{V_T}\frac{da_{\mathrm{wall,HO}}(r_{c,\mathrm{HO}})}{dr}dr} \tag{2.16}$$

$$a_{v,\mathrm{wall}} = \int_0^{\infty} \frac{a_{\mathrm{Lateral}}}{V_T} = \int_0^{r_{c,\mathrm{HI}}} \frac{2}{r}\frac{dX(r)_{\mathrm{HI}}}{dr}\,dr + \int_{r_{c,\mathrm{HO}}}^{\infty} \frac{2}{r}\frac{dX(r)_{\mathrm{HO}}}{dr}\,dr \tag{2.17}$$

The radius calculated for Knudsen diffusion accounts for the collision between gas molecules and pore walls. Therefore, the limits of the integral over the pores are switched to estimate the volume of gas pores.

Diffusivity

The Knudsen diffusion coefficient of species i is estimated as:

$$D_i^K = \frac{2\,r_{\mathrm{Kn}}}{3}\sqrt{\frac{8\,R_g\,T}{\pi\,M_i}} \tag{2.18}$$

The effects of molecular and Knudsen diffusivity are combined using the Bosanquet equation [15]:

$$D_i = \left[\frac{1}{D_{ij}} + \frac{1}{D_i^K}\right]^{-1} \tag{2.19}$$

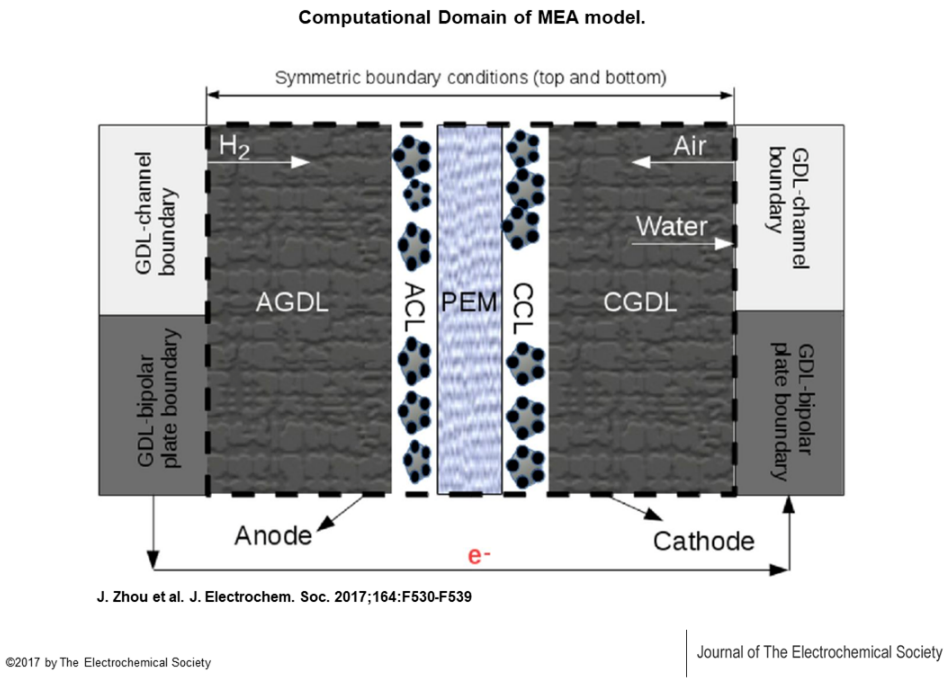

Figure 2.2: Computational domain of MEA model. Reproduced from [5].

In the GDL, the partially-saturated carbon fiber diffusion layer model proposed by Garcia-Salaberri et al. [16] is used for both in plane and through plane directions. The effective gas diffusivity is:

$$D_g^{\text{eff}} = \frac{\varepsilon_o D_i}{\tau}(1-s)^n \tag{2.20}$$

The effective diffusivity of the CL is estimated using percolation theory [17]:

$$D_g^{\text{eff}} = D_i(1-s)^\gamma \left(\frac{\varepsilon_V^{cl} - \epsilon_{th}}{1-\epsilon_{th}}\right)^\mu \theta(\epsilon_V(1-s) - \epsilon_{th}) \tag{2.21}$$

where ϵ_{th} and μ are constants that depend on the orientation of the components in CL and the function $\theta(\epsilon_V(1-s)-\epsilon_{th})$ is the Heaviside unit step function. For this thesis, the constant values are the same as J.Zhou et. al., used in [5].

2.1.5 Boundary conditions

The computational domain is shown in Figure 2.2, reproduced from [5]. The boundary conditions used for oxygen, water vapour and temperature are given in ref. [18]. Molar fractions and gas pressure at channel-GDL interface and elec-

trical potential and temperature at GDL-land interface have Dirichlet boundary conditions. There are no flux conditions defined anywhere else in the domain. The boundary conditions used for oxygen, water vapour and temperature are given in ref. [18].

A dynamic boundary condition which relates liquid pressure to liquid water flux is implemented in the model. If the capillary pressure is below a given threshold value, i.e., a breakthrough pressure, a zero liquid water flux is imposed. Once the capillary pressure reaches a given breakthrough pressure, p_{BT}, a flux proportional to the liquid pressure is applied, i.e.,

$$\rho_l \vec{u}_l \cdot \vec{n} = -\left(\frac{\rho_l k_{rl}}{\mu_l} \nabla p_l\right) \cdot \vec{n} = k \left(\frac{p_l - p_{l,\text{channel}}}{p_0}\right) g(p_l) \tag{2.22}$$

where

$$g(p_l) = \left[\frac{\tanh((p_l - p_{\text{l,channel}})/p_0) + 1}{2}\right] \theta(p_l - p_{\text{BT}}) \ , \tag{2.23}$$

where k is an unknown proportionally constant that controls the flux of water as a function of the liquid pressure. $\theta(p_l - p_{\text{BT}})$ is a step function, i.e., it is set to be zero until $p_l > p_{\text{BT}}$ is satisfied in the Newton solver loop and not modified further in order to maintain numerical stability. For this thesis a value of 0.002 Pa is selected as k value. No liquid flux boundary conditions are applied at the PEM/CL and GDL/land interfaces and at symmetric boundaries, i.e., upper and lower faces in Figure 2.2. It is assumed in the model that the dominant water transport mechanisms through the membrane are back diffusion, electro-osmotic drag and thermo-osmosis. Liquid water permeation through the membrane is not considered.

The solution strategy and the post processing routines can be found, besides more detailed mathematical description of the model, in reference [5].

2.2 Model general parameters sensitivity

Knowing the model parameters sensitivity improves the understanding of the model, helps in the calibration process, allows us to highlight the parameters in need of high accuracy and to select the most influential parameters for further

study. That is the reason for this section. However, in order to avoid extend the thesis excessively, the parameter sensitivity study details are reported in Appendix A.

Using the mathematical model described in Section 2.1 and the input parameters shown in Tables A.1 and A.2 as a baseline for the study, the model general parameter sensitivity is reported in Table 2.3. Notice in the table are shown all the parameters and its grade of influence in the polarization and cell resistance curves, depending on the case; dry, referred to 80^{o}C and 30% RH, and wet case, referred to 60 ^{o}C and 90% RH. Further, even though in Table A.3 are reported all the parameter values that perform the study, Table 2.3 shows only the effective range of values for each parameter in the study. The values studied but out of this range, either do not affect the performance or introduce numerical instabilities to the system.

Some graphical results from the sensitivity study and considered interesting can be found in Appendix A.1. Figure A.1 shows how the oxygen dissolution rate value, k_{O_2}, mainly affects the mass transport part either in dry or wet case. Further, as it governs the oxygen dissolution and thus, the kinetic reaction, it is found to be proportional in the range of values studied; the larger dissolution ratio, the better performance at high current densities. The ECSA also proportionally affects the performance and it is reflected in the activation and ohmic part of the polarization curve. The mass transport zone and cell resistance remains pretty invariable to the ECSA value. Figure A.2 shows this fact.

Cell resistance is highly affected by GDL and MPL through-plane electrical conductivity, as shown in Figure A.5. It affects the polarization curve that shows a better performance as the electrical conductivity increases; see Figures A.3 and A.4. However, the effect of varying the through-plane thermal conductivity is nontrivial, as it depends on the relative humidity condition. Increasing the TP thermal conductivity increases the performance at high current densities when the fuel cell is fed with 30%RH, however, decreases the

same performance at 90%RH.This phenomena can be found in Figure A.6. Cell resistance is also sensible to the TP thermal conductivity at high current densities for dry cases, as shown in FigureA.7.

Table 2.3: Model parameters sensitivity.

Parameter	Case	Polarization curve			Cell Resistance
		Activation	Ohmic	Mass transport	
kO_2	Dry	-	•	• • •	• • →
(0.0005 - 0.005) $[m/s]$	Wet	-	•	• • •	-
ECSA	Dry	• • •	• •	-	-
(50000 - 250000) $[cm^2_{Pt}/cm^3_{CL}]$	Wet	• • •	• •	-	-
p_{BT}	Dry	-	-	-	-
(2000 - 5000) $[Pa]$	Wet	-	-	-	-
k_{BT}	Dry	-	-	-	-
(0.0001 - 0.0025)	Wet	-	-	• • •	-
Collector/channel width	Dry	-	• •	• • •	• •
(0.5 - 1.3) $[mm]$	Wet	-	•	• • •	-
k_{sorp}	Dry	-	-	• • •	• • • →
(1.0 - 500) $[1/s]$	Wet	-	-	• • •	• • • →
ACL and CCL					
κ_{CL}	Dry	-	-	-	-
(0.0003 - 0.08) $[W/cm \cdot K]$	Wet	-	-	-	-
HI vol.fraction	Dry	-	-	-	-
(0.20 - 0.35)	Wet	-	-	-	-
HI contact angle	Dry	-	-	-	-
(82 - 92) [°]	Wet	-	-	• •	-
HO contact angle	Dry	-	-	-	-
(85 - 97) [°]	Wet	-	-	• •	-
GDL					
Porosity	Dry	-	• •	• •	• • •
(50 - 70) [%]	Wet	-	•	-	•
σ^{TP}	Dry	-	• • •	•	• •
(1.3 - 18) $[S/cm]$	Wet	-	• • •	-	• •
σ^{IP}	Dry	-	-	-	•
(105 - 420) $[S/cm]$	Wet	-	-	-	•
κ^{TP}	Dry	-	-	•	• →
(0.0009 - 0.1) $[W/cm \cdot K]$	Wet	-	-	•	-
κ^{IP}	Dry	-	-	•	• →
(0.002 - 20) $[W/cm \cdot K]$	Wet	-	-	•	-
HI vol. fraction	Dry	-	-	-	-
(0.01-0.16)	Wet	-	-	• •	• ←→

HI contact angle	Dry	-	-	-	-
(60 - 80) [°]	Wet	-	-	-	-
HO contact angle	Dry	-	-	-	-
(110 - 134) [°]	Wet	-	-	-	-
MPL					
Porosity	Dry	-	-	• •	• •
(40 - 60) [%]	Wet	-	-	• • •	•
σ^{TP}	Dry	-	• •	• •	• • •
(0.25 - 270) $[S/cm]$	Wet	-	• •	• •	• • •
σ^{IP}	Dry	-	-	-	-
(10.5 - 270) $[S/cm]$	Wet	-	-	-	-
κ^{TP}	Dry	-	•	• • •	• • →
(0.00008 - 0.008) $[W/cm \cdot K]$	Wet	-	-	• • •	-
κ^{IP}	Dry	-	-	•	• →
(0.0039 - 0.39) $[W/cm \cdot K]$	Wet	-	-	• •	• ←
HI contact angle	Dry	-	-	-	-
(83 - 95) [°]	Wet	-	-	-	-
HO contact angle	Dry	-	-	-	-
(100 - 120) [°]	Wet	-	-	-	-

Efectiveness: - nule, • low, • • middle, • • • high; →← curve side of the effect

Table 2.3: Parameter grade of effectiveness on changing the PEMFC performance. Dry case: 80°C, 30%RH. Wet case: 60°C, 90%RH.

2.3 Experimental validation and input parameters

An experiment made in-house is modeled in OpenFCST under the equations presented in Section 2.1. The goal is to validate the model to have a reliable baseline for future studies.

2.3.1 Experiment conditions

The PG/IPA based ink is prepared using 40%wt Pt/C HyPlat and 30%wt Nafion. The CCM is fabricated using the Dimatix printer (ink-jet printed technology). Thus, the ink is deposited forming a $4\,cm^2$ surface directly over the Nafion NR-211 membrane. Once printed, the platinum loading is determined; $0.049\,mg/cm^2$ for the anode and $0.105\,mg/cm^2$ for the cathode. The

CCM is assembled between the diffusion media (GDLs and MPLs) and bipolar plates, using a 135 μm thickness rigid PTFE coated fiberglass gaskets. As a diffusion media, SIGRACET® 25BC is used. The channel configuration is parallel and the current collector and channel width, measured in-house with Stereo Microscope Leica (see Appendix B.1), are 0.83 and 0.82 mm, respectively.

The experiment is executed keeping the cell temperature at 80 $°C$ and under potentiostatic mode, which changes 20 mV each 45 s. The channels are fed with H_2 and air at 50 kPa of backpressure, resulting in 1.5 atm of absolute pressure (151325.0 Pa). The anode side is fed with H_2 and H_2O. The cathode side is fed with O_2, N_2 and H_2O. The gas flow rate wet stoichiometry (anode/cathode) is 2/8 and the relative humidity is set up to be 30%. The same experiment is done, under the same conditions, for 50% RH. Higher relative humidities, when using parallel channel, resulted in flooding problems, making the experimental results unreliable. This is the reason for not having experimental data for higher humidity conditions. Table 2.4 summarizes the experimental conditions.

Table 2.4: Experimental conditions.

Parameter		**Value**
Channels configuration		Parallel channels
Potentiostatic mode		20 mV each 45 s
Gas flow rate wet stoichiometry (Anode/Cathode)		2/8
Cell area,	A	4 cm^2
Cell temperature,	T	353.15 K (80 ^{o}C)
Absolute pressure,	P_{abs}	151325 Pa (1.5 atm)
Relative humidity,	RH%	30 and 50%
Gasket thickness,	G_{thk}	135 μm (0.006 $inch$)
Lamination thickness,	L_{thk}	160 μm
Pt/C (%wt)		40%
Cathode Pt loading,	$Pt_{load_S}^{cathode}$	0.105 mg/cm^2
Anode Pt loading,	$Pt_{load_S}^{anode}$	0.049 mg/cm^2
Electrolyte loading,	$w_{electrolyte}$	30%

2.3.2 Input parameters

This section discusses the input parameter values selected to model the Section 2.3.1 experiment. All the parameter and references are summarized in Tables 2.8 and 2.9. The OpenFCST parameter files is reported in Appendix C.

Catalyst layers; ACL and CCL From ESDLab experience and old data referred to ink-jet printed catalyst layers, a value of 280 mg_{Pt}/cm^3_{CL} is assumed as a platinum density in the printed catalyst layer when 40%wt Pt/C, 0.1 mg_{Pt}/cm^2_{CL} and 30%wt Nafion is used. Thus, the cathode catalyst layer thickness is computed as the cathode Pt loading reported in Table 2.4, 0.105 mg_{Pt}/cm^2_{CL}, divided by the platinum density in CL media assumed before, 280 mg_{Pt}/cm^3_{CL}. The same ink is used for anode and cathode fabrication. The Pt loading reported in Table 2.4 for the anode is 0.049 mg_{Pt}/cm^2_{CL}. Even though the differences in thickness (between anode and cathode) could affect the layers compression while printing, this effect is considered negligible at the range of values treated. Thus, same Pt density is used in anode and cathode media, resulting thickness of 3.75μm and 1.75μm for CCL and ACL, respectively. These values can be compared in order of magnitude with literature; Shukla et. al., [19], reported 4.7±1.2μm for 50%Pt/C and 0.15 mg/cm^2. Also, in [20], reported 1.76±0.29 for 20%Pt/C and 0.026 mg/cm^2.

The catalyst layers solid, electrolyte and void volume fractions; ε_{solid}, $\varepsilon_{electrolyte}$ and ε_{void}, are computed by OpenFCST. The expressions used for the computation are reported in Appendix B.2. Again, as anode and cathode have the same composition (same ink recipe), the volume fractions are identical. The densities of platinum, ρ_{Pt}, and electrolyte, $\rho_{electrolyte}$, are integrated in OpenFCST, based on physical properties, as 21.5 and 2.0 g/cm^3, respectively. The carbon black used in this thesis is *Ketjenblack* supplied by *HyPlat*. Due to its powder form, its density can vary easily through the CCM fabrication process. For this thesis, to accomplish with the estimated volume fractions, the carbon density, ρ_{carbon}, is 1.65 g/cm^3.

The electrochemical surface area is calculated from in-house data. ECSA val-

ues of 162250 $\frac{cm^2_{Pt}}{cm^3_{CL}}$ and 134850 $\frac{cm^2_{Pt}}{cm^3_{CL}}$ are justified in Appendix B.4.
The catalyst layers thermal conductivity value, 0.0027 $W/cm \cdot K$, reported in [21] was also used in J.Zhou model in [1]. Even this value could be questioned because of its low accuracy, as proved in the parametric study and reported in Table 2.3, the model has very few sensibility to catalyst layer thermal conductivity.
Secanell et. al., [13], define the ICCP model and report the anode and cathode dissolution rate constants, k_{H_2} and k_{O_2}, 0.1 and 0.001 m/s, respectively. The anode dissolution rate constant is selected such that it has a negligible effect on performance predictions while the cathode dissolution rate constant is fitted with experimental data. Further, the ICCP catalyst particles radius value, 50 nm, is reported.

The ink-jet printed catalyst layers PSD characterization is basically extracted from the literature reported by J.Zhou et. al., [5] and [1]. The PSD interconnectivity value, λ_{PSD}, is fitted in order to evoke the desired absolute permeability in the modeled CL, $1.0 \cdot 10^{-14}$ cm^2. The hydrophilic (HI) volume fraction, 0.3, is reported by J.Zhou et. al., [1], who used a model with same Pt/C, platinum and Nafion loading for the CLs as the experiment modeled in this thesis. The hydrophilic (HI) static contact angle, 81.5 °, is calibrated to ensure the model numerical convergence. The value is in the range of values reported in the literature; 79°, reported in [22] and 84° used in [5]. The hydrophobic (HO) static contact angle, 92.5° is also calibrated according to convergence criteria, keeping the value between 93° and 91°, from [5] and [1], respectively. Lastly, the characteristic PSD pore radius, fraction and widths values; r_i, f_i and s_i are referred to J.Zhou study in [1]. Note, even the PSD definition plays a critical role in two-phase flow simulation models, the individual accuracy in each parameter do not affect excessively the model performance, as shown in Table 2.3.
The water sorption time constant value, K_{sorp}, utilized is 500 1/s. The value is established during the calibration process to fit the experimental and model

curves limiting the current through this value.

Proton exchange membrane; PEM The proton exchange membrane used is the NRE 211. Its properties are already implemented in OpenFCST. The parameter values are summarized in Table 2.5, extracted directly from J. Zhou work in [1].

Table 2.5: Membrane NRE 211 parameters. Reproduced from [1]

PEM	Literature	Value/direction/equation
Water diffusion	Motupally et al. [23]	$0.000417\lambda(1.0+161.0exp(-\lambda))exp(-\frac{-2436.0}{T})$, $\lambda > 3.0$
Electro-osmotic drag coefficient	Makota et al. [24]	1.0
Sorption isotherm	Mittelsteadt and Liu [25]	$(1.0+0.2352a_w^2\frac{(T-303.15)}{30.0}(14.22a_w^3-18.92a_w^2+13.41a_w))$, $a_w = RH$
Proton conductivity	NRE 211 [26]	$(-0.000120125\lambda^2+0.01052\lambda-0.020634)exp(751.5412(\frac{1}{303}-\frac{1}{T}))$
Thermal-osmosis	Kim and Mench [27]	Cold to hot
Thermal conductivity $(W/(cm\cdot K))$	Khandelwal and Mench [28]	0.0013

Gas diffusion and micro-porous layers; GDL and MPL The gas diffusion media utilized in the experiment is SGL 25BC. However, nowadays SGL 25BC is not supplied by the manufacturer anymore. Due to its wide physical similitudes with SGL 28BC, this is the gas diffusion media selected to take part in the modeled MEA. Further, ESDLab recently characterized the SGL 28BC unstacked properties using mercury intrusion porosimetry (MIP) with PoreMaster 33 Quantachrome device. The data is summarized in Table 2.6. Future experiments will prove how reliable is to neglect the few differences between 25BC and 28BC.

From Table 2.6, note that GDL (28BA) thickness, $138.8\mu m$, added to MPL thickness, $114.7\mu m$, results $253.5\mu m$. This value is larger than the actual 28BC (MPL+GDL) thickness, $228.6\mu m$. This is because, during its fabrication, the MPL penetrates into the GDL media forming an interface made out of both materials. In this case, the thickness of this interface is $24.9\mu m$. Due to its mixed composition and randomly distribution in the space, its conductivity properties remain as unknown values for modelers. For this Thesis, as pure GDL conductivity properties are known, it is decided to preserve the known properties in the region where the GDL is not overlapped with the MPL and

group all the uncertainties in the MPL media. Thus, the pure GDL thickness is the part of the SGL 28BC that not contains any MPL; GDL_{thk}= 113.9μm. The rest is considered MPL; MPL_{thk}=114.7μm

During the stacking process, the CCM is compressed between the bipolar plates. It is fair to assume the membrane, the catalyst layers and the MPLs as incompressible media. Thus, MPLs porosity is directly the one reported in Table 2.6, 74.4%. However, the GDLs are the component that change its thickness and therefore its porosity during the stacking process. Taking into account the gasket size used, 135 μm, the GDL thickness after stacking becomes 85.1μm and its porosity, 71.34%. The discussions and equations to get this values are reported in Appendix B.3.

SIGRACET® in its catalog, [29], provides a range of values for SGL 28AA and 28BC conductivity properties. This range is averaged and reported in Table 2.7. It is assumed that SGL 28AA is representative of GDL properties (thickness, electrical and thermal conductivity) –i.e., PTFE does not significantly modify said properties. Further, it is assumed that GDL electrical conductivity at 1MPa fairly describes the actual GDL conductivity under the operating conditions (stacked state). About thermal conductivity properties, Nitta et. al., [30], reported non dependence between compressed and uncompressed GDL thermal conductivity. Thus, values from Table 2.7 are considered reliable for the GDL properties; σ^{TP}_{GDL}, σ^{IP}_{GDL} and κ^{TP}_{GDL}. The MPL electrical properties are estimated assuming the diffusion media, GDL and MPL, as a electrical circuit. The estimated values for σ^{TP}_{MPL} and σ^{IP}_{MPL}, 1.93 and 173.43 S/cm respectively, are justified in Appendix B.5. The through-plane electrical conductivity values, σ^{TP}_{GDL} and σ^{TP}_{MPL}, do not take into account the contact resistance with the catalyst layer and the bipolar plates. Fitting the cell resistance and polarization curves, σ^{TP}_{GDL}=1.3S/cm and σ^{TP}_{MPL}=0.5S/cm are established.

The through-plane MPL thermal conductivity, κ^{TP}_{MPL}=0.0065$W/cm \cdot K$, is estimated assuming same series resistance circuit as for electrical conductivity. Detailed procedure can be found in Appendix B.6. The estimation to

determine the in-plane diffusion media thermal conductivity; $\kappa^{IP}_{GDL+MPL} = 12 \cdot \kappa^{TP}_{GDL+MPL}$ is based on results from [31], [32] and [33]. The expression to estimate the in-plane MPL thermal conductivity, function of its porosity, $\kappa^{IP}_{MPL} = f(\varepsilon_{MPL})$=0.007 $W/cm \cdot K$, is taken from [34]. Finally, the κ^{IP}_{MPL}=0.1597 $W/cm \cdot K$, is estimated with the circuit theory. The procedure is also reported in Appendix B.6.

The PSD characterization parameter values for the gas diffusion media, GDL and MPL, are partly found in the literature or directly measured with mercury intrusion porosimetry. The characteristic PSD pore radius, fraction and widths values; r_i, f_i and s_i for GDL and MPL, and also the absolute permeability for GDL are directly taken from Table 2.6. Absolute permeability value for MPL, $1.39 \cdot 10^{-9}$, is reported in [35] and used in [1]. Note that PSD characterization is assumed to be identical (r_i, f_i and s_i) for hydrophilic and hydrophobic fraction. The PSD porous interconnectivity, λ_{PSD}, is fitted in order to evoke the desired absolute permeability in the model. Thus, 1.605 and 0.227 are chosen as GDL and MPL λ_{PSD}, respectively. The hydrophilic volume fraction, 0.08, and static contact angle, 70°, for the GDL, are both extracted from J.T. Gostick work with SGL 34BA, [36]. J.T. Gostick et. al., [37] reported the hydrophobic static contact angle for SGL 34BA, 122°, used in this thesis as a approximate value for SGL 28BA. Micro porous layer is actually highly hydrophobic, however, introducing a null value as hydrophilic volume fraction deals with numerical instabilities that are solved assigning 0.01 to this parameter. The hydrophilic contact angle for MPL, 84°, with few influence in the model due to the insignificant hydrophilic volume fraction in the MPL media, is used before by J.Zhou in [5] and [1]. The same models used 120° and 110° for the hydrophobic contact angle. For this thesis, this value is averaged; 115°.

Current collector and channel width, 0.083 and 0.082cm, are measured with in-house microscopy technology as discussed in Section 2.3.1. The breakthrough capillary pressure in the GDL/channel interface, p_{BT}=2000Pa, is the

Table 2.6: SGL 28BC and 28BA unstacked properties measured with mercury intrusion porosimetry in ESDLab. PoreMaster 33 Quantachrome.

Parameter		**SGL 28BC**	**SGL 28BA**	**MPL SGL 28**
Thickness	(μm)	228.6	138.8	114.7
Porosity	$(\%)$	69.0	78.6	74.4
Absolute permeability	(cm^2)	$7.3 \cdot 10^{-8}$	$4.6 \cdot 10^{-8}$	
Characteristic pore radius	(μm)			
r_1		0.00525	0.748	0.00525
r_2		0.748	29.2	
r_3		29.2	48.5	
r_4		48.5		
Characteristic pore widths				
s_1		0.606	0.455	0.367
s_2		0.455	2.354	
s_3		2.354	0.367	
s_4		0.367		
Characteristic pore fraction				
f_1		0.284	0.214	1.0
f_2		0.153	0.492	
f_3		0.353	0.294	
f_4		0.210		

value used by J.Zhou in [5]. The water surface tension, γ, is a water physical parameter function of the temperature. For $80°C$ its value is $0.063 N/m$. Finally, the boundary condition for constant capillary pressure, k_{BT}, is $0.002 Pa$. This value controls the moment when the modeled fuel cell starts to evacuate the water from the porous media. The value is extracted from ESDLab experience. Due to its exclusive effect in wet cases, this value is not possible to calibrate with the experimental data.

Table 2.7: Conductivity properties in 2D for SGL 28BC and 28BA. Data extracted from [29]. In-plane properties averaged from X/Y directions.

Parameter		**SGL 28BC**	**SGL 28AA**
Electrical conductivity *	$[S/cm]$		
Through-plane,	σ^{TP}	2.55	4.5
In-plane,	σ^{IP}	190	212.5
Thermal conductivity **	$[W/cm \cdot K]$		
Through-plane,	κ^{TP}	0.006	0.0055

* Measured under 1MPa compression ** Measured at non-compress state

Table 2.8: Model parameters.

Parameter		**Value**	**Reference**
Conditions			
Breakthrough capillary press. GDL/channel interface;	p_{BT}	2000 Pa	[5]
Constant cap. press. BC,	k_{BT}	0.002 Pa	ESDLab
Water surface tension,	γ	0.063 N/m	Value for 80 ^oC.
Carbon black density,	ρ_{carbon}	1.65 g/cm^3	ESDLab HyPlat
Platinum density,	ρ_{Pt}	21.5 g/cm^3	Physical constant
Electrolyte density,	$\rho_{electrolyte}$	2.0 g/cm^3	Nafion®
Dimensions			
Current collector width		0.083 cm	Measured. Appendix B.1.
Channel width		0.082 cm	Measured. Appendix B.1.
Cathode CL thickness	CCL_{thk}	3.75 μm	Estimated
Anode CL thickness	ACL_{thk}	1.75 μm	Estimated
GDL thickness	GDL_{thk}	$0.851 \cdot 10^{-2}$ cm	In-house. Appendix B.3
MPL thickness	MPL_{thk}	$1.147 \cdot 10^{-2}$ cm	In-house. Table 2.6
Membrane thickness	PEM_{thk}	$2.5 \cdot 10^{-3}$ cm	NRE 211
Anode and cathode CL (IJP)			
Pt/C	(%wt)	40%	Baseline condition
Volumetric Pt loading,	Pt_{load_V}	280 mg/cm^3	Estimated ESDLab
Cathode Pt loading,	Pt_{load_S}	0.105 mg/cm^2	Baseline condition
Anode Pt loading,	Pt_{load_S}	0.049 mg/cm^2	Baseline condition
Electrolyte loading,	$w_{electrolyte}$	30%	Baseline condition
Anode $ECSA_V$		134850 cm^2_{Pt}/cm^3_{CL}	In-house. Appendix B.4
Cathode $ECSA_V$		162250 cm^2_{Pt}/cm^3_{CL}	In-house. Appendix B.4
Thermal conductivity,	κ_{CL}	0.0027 $W/cm \cdot K$	[21]
ε_{solid}		0.2676	Appendix B.2
$\varepsilon_{electrolyte}$		0.1506	Appendix B.2
ε_{void}		0.5824	Appendix B.2
ICCP radius		50 nm	[13]
k_{O_2} (O_2 dissolution rate)		0.001 m/s	[13] (80 ^{o}C, 50%RH)
k_{H_2} (H_2 dissolution rate)		0.1 m/s	[13] (80 ^{o}C, 50%RH)
k_{sorp}		500 $1/s$	Calibrated
PEM (NR-211)			
Electrolyte type		Nafion	NR-211
Thermal conductivity,	κ_{PEM}	0.0013 $W/cm \cdot K$	NR-211; [21]
GDL (SGL 28BC)			
Porosity		71.35%	Estimated. Appendix B.3
Electrical conductivity (TP),	σ^{TP}_{GDL}	1.3 S/cm	Calibrated
Electrical conductivity (IP),	σ^{IP}_{GDL}	212.5 S/cm	[29] (SGL 28AA)
Thermal conductivity (TP),	κ^{TP}_{GDL}	0.0055 $W/cm \cdot K$	[29] (SGL 28AA)

Thermal conductivity (IP),	κ_{GDL}^{IP}	0.1597 $W/cm \cdot K$	Estimated. Appendix B.6.2
MPL (SGL 28BC)			
Porosity		74.4%	Measured in-house B.3
Electrical conductivity (TP),	σ_{MPL}^{TP}	0.5 S/cm	Calibrated
Electrical conductivity (IP),	σ_{MPL}^{IP}	173.43 S/cm	Estimated. Appendix B.5
Thermal conductivity (TP),	κ_{MPL}^{TP}	0.0065 $W/cm \cdot K$	Estimated. Appendix B.6.1
Thermal conductivity (IP),	κ_{MPL}^{IP}	0.0070 $W/cm \cdot K$	Estimated. Appendix B.6.2

Table 2.9: Model PSD parameters.

Parameter		**Value**	**Reference**
Anode and cathode CL (IJP)			
Absolute permeability,	k_{sat}	$1.00{\cdot}10^{-14}$ cm^2	[38]
PSD interconnectivity,	λ_{PSD}	2.35	Fitted for abs. perm.
HI volume fraction,	F_{HI}	0.3	[1]
HI static contact angle,	ϕ_{HI}	81.5°	Calibrated; [22]
HO static contact angle,	ϕ_{HO}	92.5°	Calibrated; [5], [1]
Characteristic:			
Pore radius,	r_i $[\mu m]$	0.02, 0.025, 0.075	[1]
Pore fraction,	f_i	0.65, 0.28, 0.07	[1]
Pore widths,	s_i	0.55, 0.45, 1.2	[1]
GDL (SGL 28)			
Absolute permeability,	k_{sat}	$4.6{\cdot}10^{-8}$ cm^2	In-house MIP
PSD interconnectivity,	λ_{PSD}	1.605	Fitted for abs. perm. [1].
HI volume fraction,	F_{HI}	0.08	[36]
HI static contact angle,	ϕ_{HI}	70°	[36]
HO static contact angle,	ϕ_{HO}	122°	[37]
Characteristic:			
Pore radius,	r_i $[\mu m]$	0.748, 29.2, 48.5	In-house MIP
Pore fraction,	f_i	0.214, 0.492, 0.294	In-house MIP
Pore widths,	s_i	0.455, 2.354, 0.367	In-house MIP
MPL (SGL 28)			
Absolute permeability,	k_{sat}	$1.39{\cdot}10^{-9}$ cm^2	[35]
PSD interconnectivity,	λ_{PSD}	0.227	[1]
HI volume fraction,	F_{HI}	0.01	[1]
HI static contact angle,	ϕ_{HI}	84°	[5], [1]
HO static contact angle,	ϕ_{HO}	115°	Averaged [39], [36]
Characteristic:			
Pore radius,	r_i	0.0525 μm	In-house MIP
Pore fraction,	f_i	1	In-house MIP
Pore widths,	s_i	0.606	In-house MIP

2.3.3 Model validation

The OpenFCST application used to run the simulations is *meaTwoPhaseNITcapillary*. When cell resistance is computed, this application takes into account the proton ohmic heat generated at the anode and cathode catalyst layers. However, in ESDLab experimental cell resistance determination, this two resistances are not measured. In order to avoid this difference in the validation and futures comparisons, the code is modified and proton ohmic heat generated in ACL and CCL is not computed as cell resistance in this Thesis.

As discussed in section 2.3.2, some parameters are calibrated while fitting the curves. Figures 2.3 and 2.4 show the result for the two cases, 30 and 50%RH. It is important to keep in mind the experimental data was extracted from a cell that used quite different MPL and GDL so the results will never match completely. Further, the studies proposed for this Thesis are based on the differential of performance with respect to a baseline. Thus, the present model is accepted as a reliable baseline for future studies.

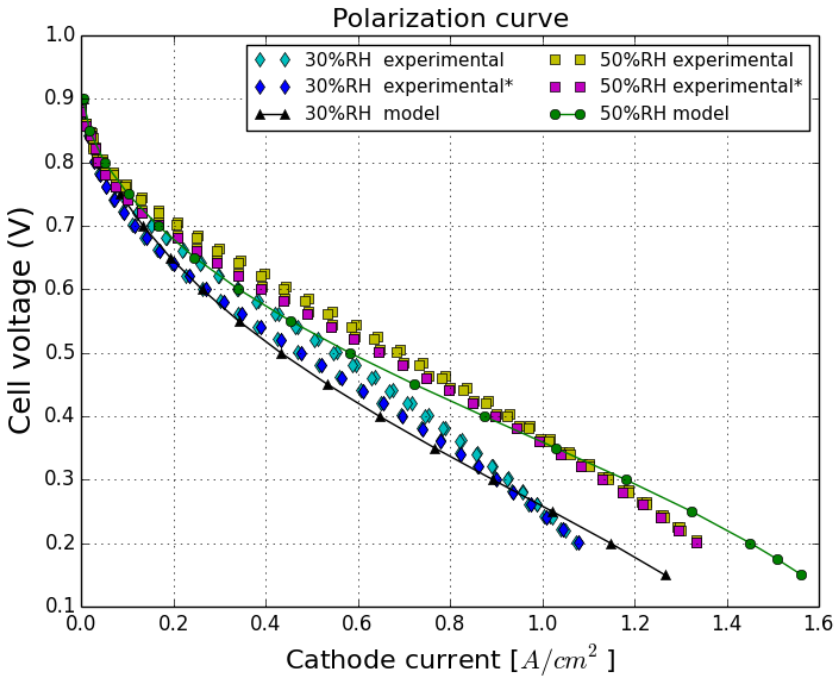

Figure 2.3: Overlapped experimental and model polarization curves curves under 30% and 50% RH.

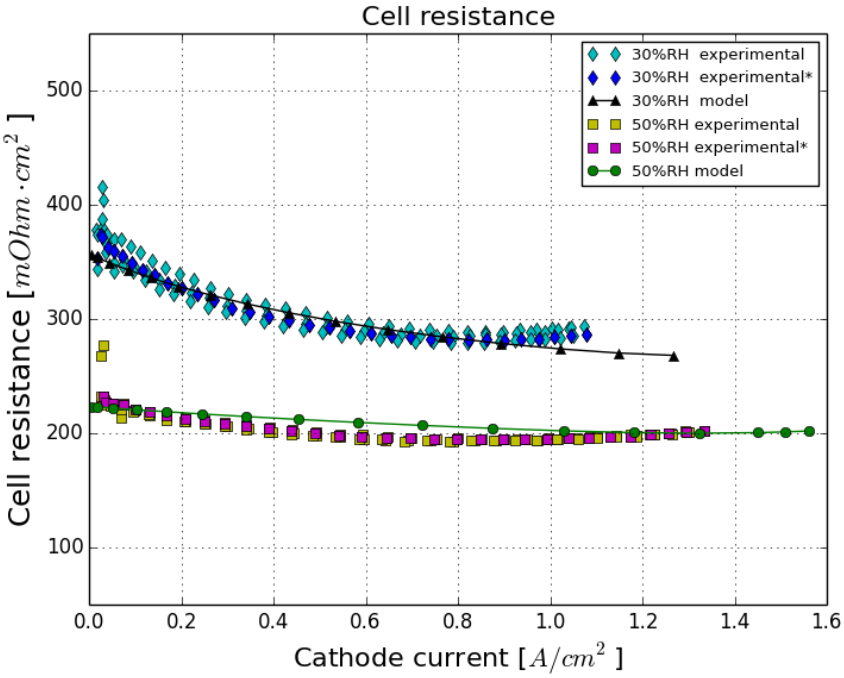

Figure 2.4: Overlapped experimental and model cell resistance curves under 30% and 50% RH.

Chapter 3

Results and discussions

The model presented in Section 2.3 is used as a baseline for different studies. For each case, few parameters are changed in order to compare the results and better understand the PEMFC physics and behavior.

3.1 Model response to different humidity conditions

Both anode and cathode are fed through the channels with hydrogen, H_2, and oxygen-nitrogen mixture, O_2 and N_2, respectively. Further, water vapor, H_2O, mixed with the reactants, is introduced in the PEMFC and its quantity affects the cell behavior and performance. This section is intended to show how the model responds to different reactants humidity conditions. Concretely; 30, 50, 75 and 90%RH.

The solutions for the four experiments have convergence problems when the channels are fed with high humidity conditions. The points that define the curves are not as equidistant as desired. This is because the solver cannot find a numerical solution at some specific current range. Thus, the curves do not have a reliable shape. This convergence instability is a problem that reappears in futures sections. However, the convergence issue is solved by slightly modifying the catalyst layer porous interconnectivity; λ_{PSD}. Using $\lambda_{\text{PSD}} = 6$ for high humidity cases instead of 2.35 (see Table 2.9) improves the convergence without affecting the results, i.e., the cell performance. Figures 3.1 and 3.2 show the polarization and cell resistance curves for all the experiments

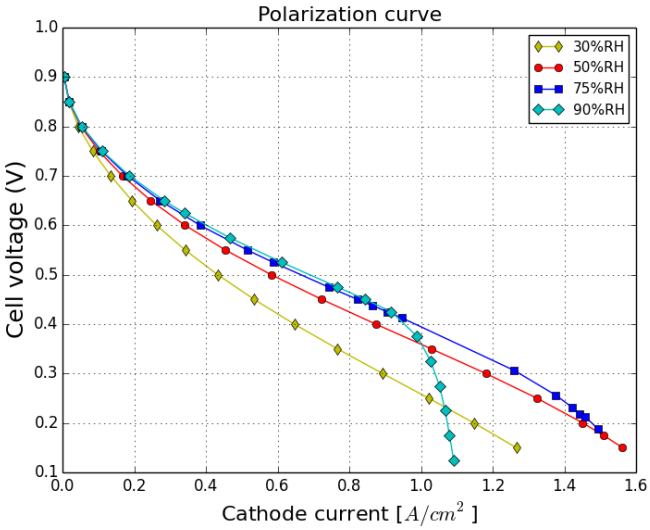

Figure 3.1: Polarization curves for the model response under different relative humidities feeding conditions; 30, 50, 75 and 90%RH. Improved convergence by using λ_{PSD}=6 for 75 and 90%RH.

when $\lambda_{\text{PSD}} = 6$ for wet cases.

It is observed an important decrease of cell resistance with higher humidity values and subsequently, an increase in performance in the ohmic part. The decrease in cell resistance is due to the proton conductivity improvement under wet conditions. However, when the channels are fed with high humid reactants (90%RH in this case), the performance decreases rapidly for current density values over 1.0 A/cm^2. This phenomena is also observed in real experiments in ESDLab. In order to understand the reason for this performance decrease, the cathode catalyst layer saturation at 1.0 A/cm^2 is compared between the 50 and 90 %RH simulations. As expected, saturation levels are quite different. Figure 3.3 shows higher saturation level in the case of 90%RH. This liquid water fills the porous media in the catalyst layer. Thus, the oxygen flux decrease and less reactant reach the reaction per unit of time. Figure 3.4 demonstrate this fact by comparing the oxygen molar fraction distribution in the CCL. Finally, relating this decrease of oxygen with the performance, Figure 3.5 shows the oxygen reduction reaction (ORR) volumetric current density generated in the cathode catalyst layer. Notice how, in the 50%RH case, the reaction occurs

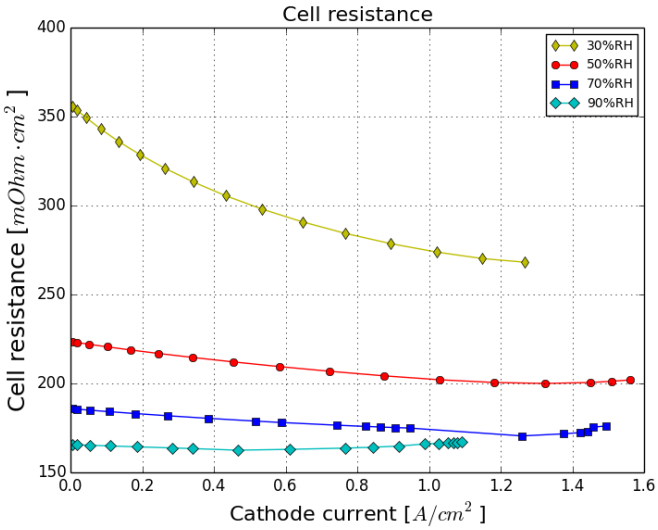

Figure 3.2: Cell resistance curves for the model response under different relative humidities feeding conditions; 30, 50, 75 and 90%RH.

Table 3.1: Maximum power (W), and power per unit of Pt mass (W/mg_{Pt}) offered by the experimented PEMFCs under the specified humidity conditions; 30, 50, 75 and 90%RH.

Experiment	P_{max}	30%RH	50%RH	75%RH	90%RH
Baseline	(W/mg_{Pt})	2.56	3.43	3.72	3.71
	(W)	1.07	1.44	1.56	1.56

next to the membrane and is quite uniform all over the CCL. However, in the 90%RH case, the reaction occurs next to the channel and is concentrated in this zone. Due to the high saturation level, protonic conductivity is increased and, together with the difficulty for the oxygen to cross, favor the displacement of the reaction to the MPL-CL interface. This phenomena auto limits the reaction and that is why the curve have this vertical shape at high current densities. The normalized water balance inside the catalyst layer is shown in Figure 3.6. Notice how liquid water in the cathode starts to show up over 0.5 A/cm^2 and increase till the performance collapse.

In order to have a numerical value to compare the PEMFCs performance and goodness through the different cells and experiments, the maximum power and the maximum power per unit of platinum mass is used. Table 3.1 summarizes these values for the baseline studied in this section.

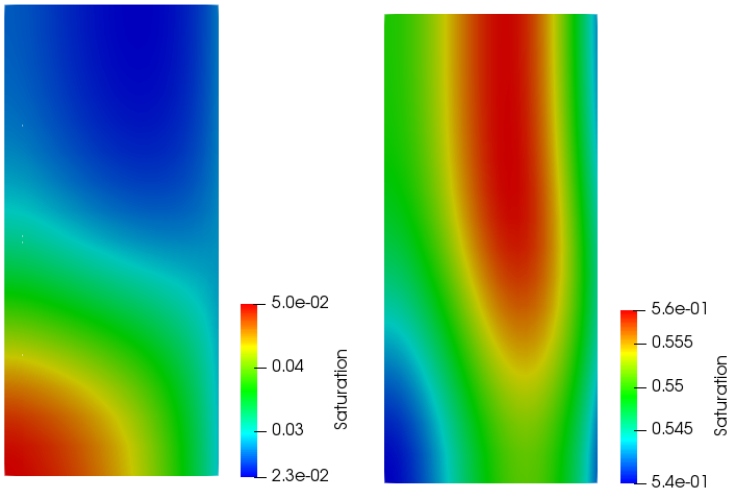

Figure 3.3: Cathode catalyst layer saturation level at 1.0 A/cm^2 for cases; 50%RH (left) and 90%RH (right).

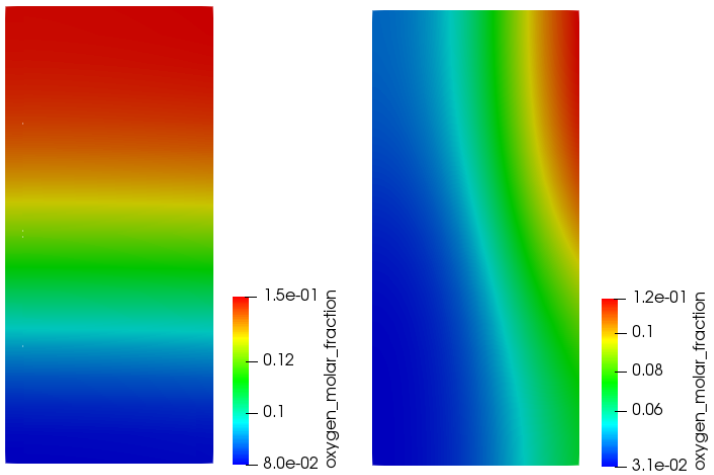

Figure 3.4: Cathode catalyst layer oxygen molar fraction at 1.0 A/cm^2 for cases; 50%RH (left) and 90%RH (right).

3.2 Cathode catalyst layer variable %Pt/C and constant thickness

Platinum is the catalyst that accelerates the reactions in the cell. Due to its importance and elevated cost, it is an interesting parameter to study. This section and the next one, Section 3.3, study the platinum loading in the cathode catalyst layer as is the one that limits the cell performance.

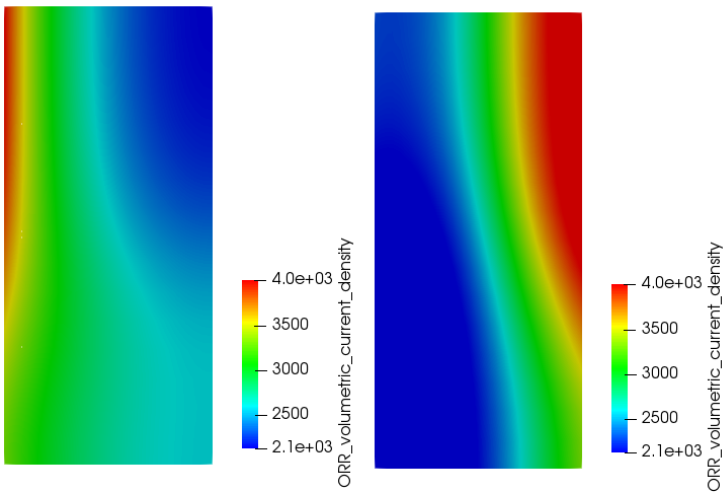

Figure 3.5: Cathode catalyst layer oxygen reduction reaction volumetric current density at 1.0 A/cm^2 for cases; 50%RH (left) and 90%RH (right).

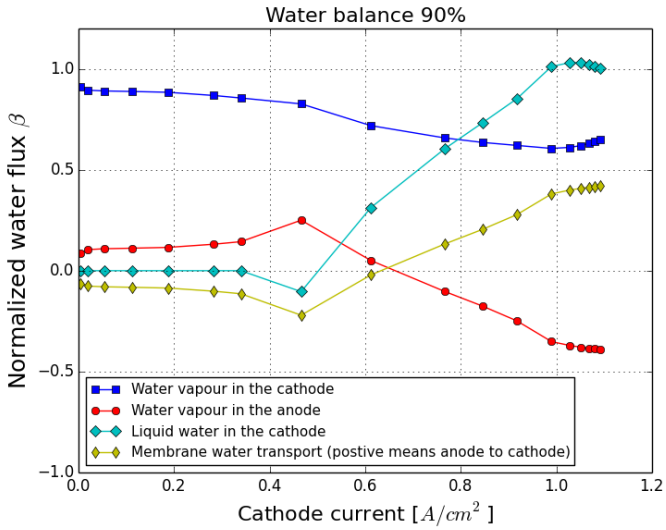

Figure 3.6: Water fluxes inside the cell for 90%RH case. Positive when the water is leaving the MEA.

3.2.1 Study

Three different cells are modeled for this study. All of them have, as the only difference, the cathode catalyst layer. Keeping a constant thickness of 3.75 μm in all three CCL, the %Pt/C content is the variable parameter. Thus, 20, 40 and 60%Pt/C are the values selected for this study. Table 3.2 summarizes the differences (all of them induced by the platinum loading) between the three

catalyst layers.

Table 3.2: Cell's cathode catalyst layer properties for the study. Variable %Pt/C and constant thickness.

	Case 1	Case 2 (BL)	Case 3
Thickness, μm	3.75	3.75	3.75
Pt/C, %	20	40	60
Pt_{load_S}, mg_{Pt}/cm^2	0.0525	0.1050	0.1575
Pt_{load_V}, mg_{Pt}/cm^3	140	280	420
$ECSA_V$, cm^2_{Pt}/cm^3_{CL}	76272	162250	243375
ϵ_{solid}	0.3459	0.2676	0.1892
$\epsilon_{electrolyte}$	0.1500	0.1500	0.1500
ϵ_{void}	0.5041	0.5824	0.6608

$ECSA_V$ value for the case with 20%Pt/C is based on S.Shukla et.al., [40], who reported 54,48 m^2/g for 0.056 mg/cm^2 platinum loading. This value is computed with equation B.4 taking 0.0525 mg/cm^2 as Pt loading and 3.75 μm as CL thickness, resulting 76272 cm^2_{Pt}/cm^3_{CL}.

The $ECSA$ value for the 60% Pt/C case is estimated multiplying the active area corresponding to 40% Pt/C by 1.5, resulting $ECSA_V = 243375 cm^2_{Pt}/cm^3_{CL}$

3.2.2 Results

Dry, 30%RH

The polarization and cell resistance curves for each platinum loading case are shown in Figures 3.7 and 3.8, respectively. Even though the amount of platinum in the third experiment is three times larger than in the first one, its effect on the cell performance is not very large. Figure 3.9 shows the ORR volumetric current density in the cathode catalyst layer for cases 1 and 2 when the cells are producing 0.8 A/cm^2. The reaction mainly occurs just next to the membrane, using the platinum deposited next to the diffusion media to a lesser degree. Merging this idea with the short improvement in performance, it can be thought that protonic flux is too low and H^+ is consumed before it can reach the O_2 richest part; next to the channels. Thus, the platinum deposited equally all over the layer ends up being unused.

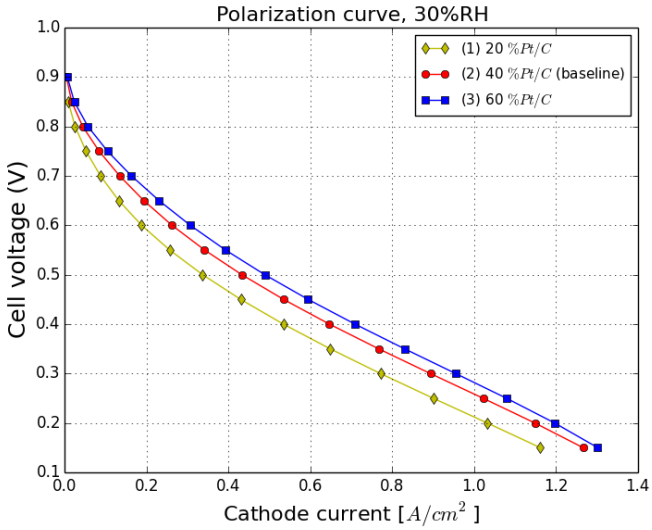

Figure 3.7: Polarization curves from PEMFCs with different %Pt/C in the cathode catalyst layer. 30%RH.

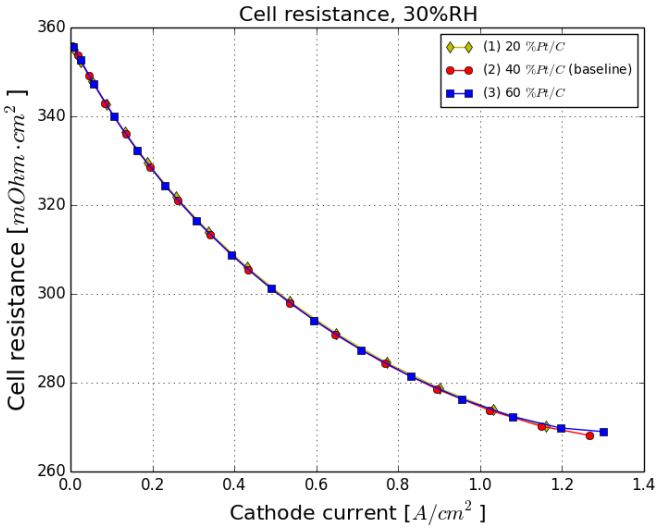

Figure 3.8: Cell resistance curves from PEMFCs with different %Pt/C in the cathode catalyst layer. 30%RH.

It is interesting to note the invariant shape of the cell resistance curve. Even the platinum has no direct affectation to ohmic conductivity, modifying the ink composition also modifies the catalyst layer volume fractions, as shown in Table 3.2. It implies different solid and void volumes in the media that is expected to affect in the electrical conductivity and mass transport. However, the effect in the overall cell resistance seems to be negligible even the solid part

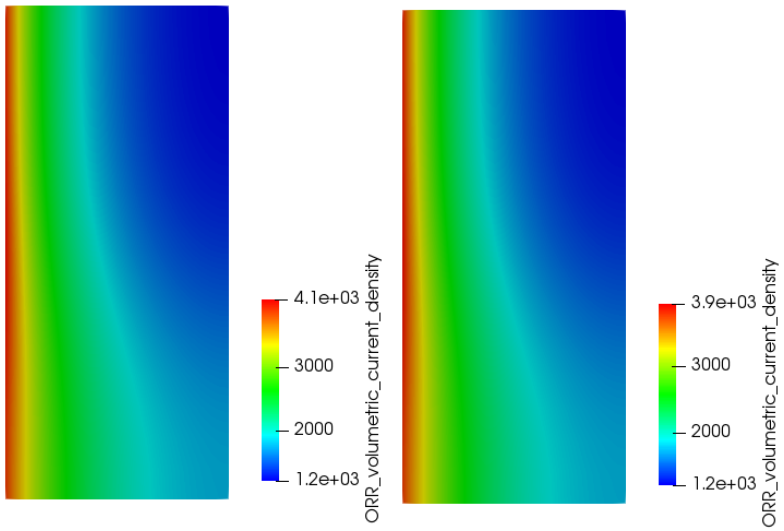

Figure 3.9: Cathode catalyst layer oxygen reduction reaction volumetric current density for the cells (1)-20%Pt/C (left) and (2)-40% Pt/C (right) at 0.8 A/cm^2. 30%RH.

is reduced up to 45% between first and third experiment. The electronical electrical potential, shown in Figure 3.10, is uniform in both cases. Even though the electrons have to cross all the catalyst layer to reach the reaction, there is no potential gradient through the media. It means that negligible ohmic losses are induced by the electrons flux. The increase of void part does not improve the performance either as the mass transport is not a limiting issue in dry case due to the low saturation of the porous media.

Wet, 90%RH

The wet case convergence also has to be adjusted like in Section 3.1. The porous connectivity parameter is established $\lambda_{\text{PSD}} = 3.3$ for experiment (1) and $\lambda_{\text{PSD}} = 6$ for experiments (2) and (3). The performance is verified to be the same with the baseline value. The experiments performance and cell resistance curves are shown in Figures 3.11 and 3.12, respectively. In this case, it is interesting to note the limiting current gets higher values when the %Pt/C increases. It is probably due to the increase of void part in the media, delaying the onset of limiting current.

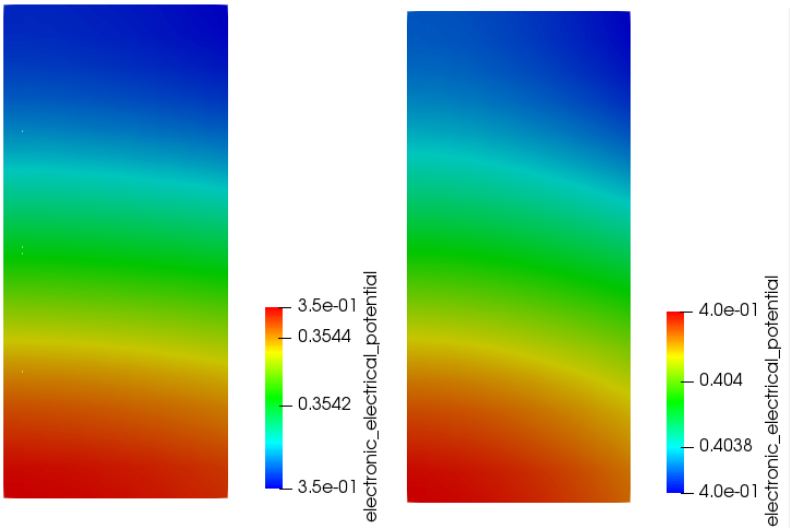

Figure 3.10: Cathode catalyst layer electronical electrical potential for the cells (1)-20%Pt/C (left) and (2)-40% Pt/C (right) at 0.8 A/cm^2. 30%RH.

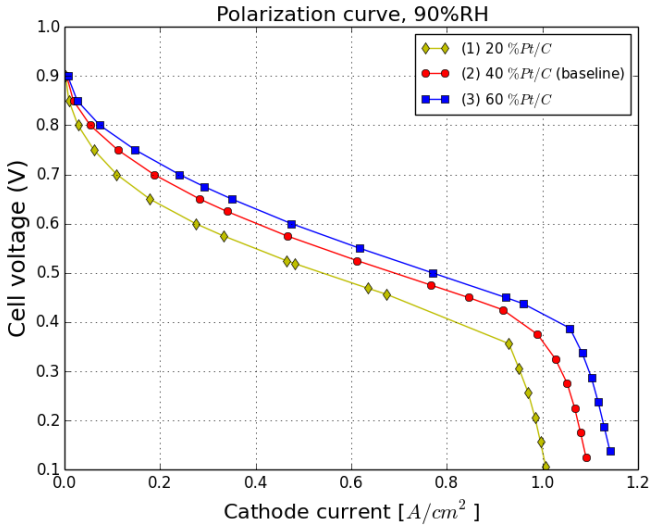

Figure 3.11: Polarization curves from PEMFCs with different %Pt/C in the cathode catalyst layer. 90%RH.

Initially, the performance is limited by the reaction kinetics, then ohmic losses. Finally, mass transport losses lead to a sudden performance limitation. From the results in this Thesis, it seems a maximum saturation level exist, for each catalyst layer and high influenced by its void fraction. Once the maximum saturation level is reached next to the gas diffusion media, it acts as a wall for the oxygen flow and the performance starts to decay drastically. Then, the

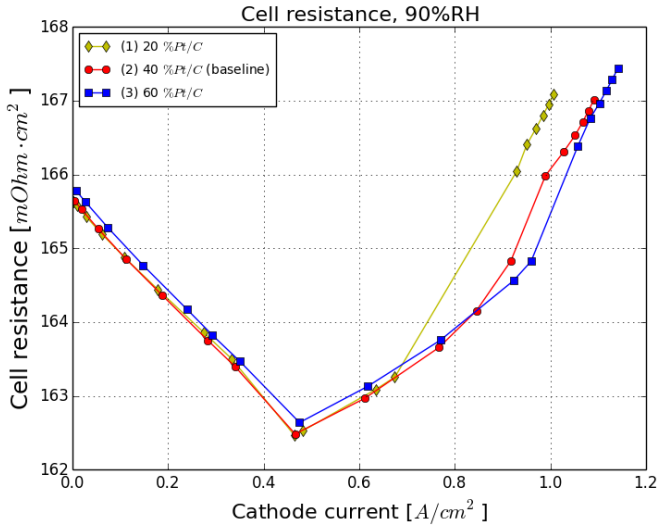

Figure 3.12: Cell resistance curves from PEMFCs with different %Pt/C in the cathode catalyst layer. 90%RH.

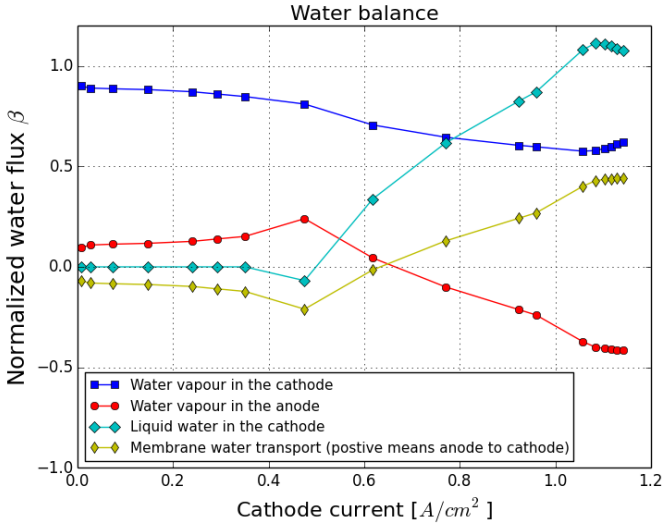

Figure 3.13: Normalized water balance inside the cell for experiment (3) with 60%Pt/C and wet case; 90%RH.

reaction evolves without increasing this maximum saturation level, especially next to the GDL and MPL. Thus, the reaction progress highly depends on how fast the liquid water can be evacuated from the porous media. It is proved capturing, for the three experiments, the saturation level around 0.38V, when the performance starts to decay, and at 0.1V, when the reaction is limited by mass transport. Figures 3.14 and 3.15 show this two points. Note how

the saturation map inside the catalyst layer tends to a constant distribution, independent of the voltage (in the specified range). The ORR kinetic seems to be the one that equilibrate the water produced by the reaction with the water that leaves the cell.

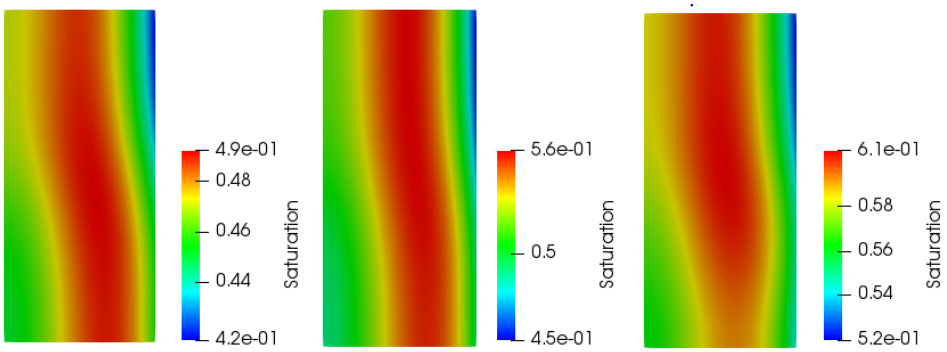

Figure 3.14: Cathode catalyst layer saturation level at 0.38V for the 20, 40 and 60% Pt/C from left to right, respectively. 90% RH.

The experiment (3), with 60% Pt/C, is the one that has better performance response. Further, it is the cell that has the highest limiting current, reaching $1.14 A/cm^2$ at 0.1V. A part from the higher platinum loading, this improvement is also due to the larger void fraction, ϵ_{void}, that allows to reach higher saturation levels by keeping constant the actual void fraction, ϵ'_{void} defined as the void part that is not filled by liquid water in the highest saturated area; the one that forms the "water-wall" for the oxygen.

$$\epsilon'_{void} = \epsilon_{void} \cdot (1 - Saturation)$$

Table 3.3 summarizes, for each case, the ϵ_{void}, maximum saturation reached during the experiment and ϵ'_{void}. It seems that ϵ'_{void} is characteristic for each MEA and it could be related with ability of the cell to evacuate the water.

Table 3.3: Actual void part when maximum saturation level is reached in experiments (1), (2) and (3).

Experiment	ϵ_{void}	Max. saturation	ϵ'_{void}
(1) 20% Pt/C	0.5041	0.51	0.257
(2) 40% Pt/C	0.5824	0.57	0.250
(3) 60% Pt/C	0.6608	0.61	0.257

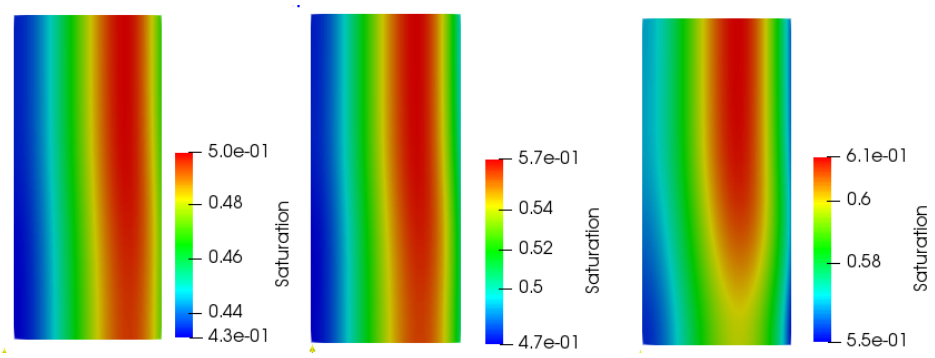

Figure 3.15: Cathode catalyst layer saturation level at 0.1V for the cases 20, 40 and 60% Pt/C from left to right, respectively. 90%RH.

Table 3.4: Maximum power (W), and power per unit of Pt mass (W/mg_{Pt}) offered by the experimented PEMFCs under the specified humidity conditions; 30, 50, 75 and 90%RH.

Experiment	P_{max}	30%RH	90%RH
(1)-20%Pt/C	(W/mg_{Pt})	4.41	6.12
	(W)	0.93	1.28
(2)- 40%Pt/C (BL)	(W/mg_{Pt})	2.56	3.71
	(W)	1.07	1.56
(3)-60%Pt/C	(W/mg_{Pt})	1.85	2.68
	(W)	1.16	1.69

Finally, Table 3.4 summarizes the maximum power reached for the cells in the experiments of this section. It is interesting to note even the 60%Pt/C is the configuration that offers higher power values it is also the one with the worst ratio W/mg_{Pt}.

3.3 Cathode catalyst layer constant %Pt/C and variable thickness

As in the previous Section, the main goal of this one is to study the platinum loading in the cathode catalyst layer. In this case, the Pt/C content is the same in all the experiments. The variable parameter that changes the Pt loading is the catalyst layer thickness.

3.3.1 Study

Five cells are modeled for this study. All of them have, as the only difference, the cathode catalyst layer. Keeping a constant Pt/C=40%, the thickness is variated from 3.75 μm to 12 μm. Table 3.5 summarizes the differences between the five catalyst layers. Notice, in this case volumetric ECSA and volume fractions are identical in all the cases due the fact that all of them are made of the same ink compositions. Thus, assuming no-compression during fabrication (due to its own weight), the only difference is the thickness and the platinum loading.

Table 3.5: Cell's cathode catalyst layer properties for the study. Variable thickness and constant %Pt/C.

	Case 1 (baseline)	Case 2	Case 3	Case 4	Case 5
Thickness, μm	3.75	6.0	8.0	10.0	12.0
Pt/C, %	40	40	40	40	40
Pt_{load_S}, mg_{Pt}/cm^2	0.105	0.168	0.224	0.280	0.336
Pt_{load_V}, mg_{Pt}/cm^3	280	280	280	280	280
$ECSA_V$, cm^2_{Pt}/cm^3_{CL}	162250	162250	162250	162250	162250

3.3.2 Results

Dry, 30%RH

The overall results for the dry case, as a performance and cell resistance curves, are shown in Figures 3.16 and 3.17, respectively. In this case, even the differences in the platinum content are larger than in simulations presented in Section 3.2, the performance variation is less significant. For example, catalyst layer platinum loading in the fifth experiment is more than three times larger than in the first one. However, there is very few difference between both polarization curves.

About the cell resistance, it is still invariant through the five experiments even though the catalyst layer thickness is increasing and its electronic and protonic resistance could be affected due to the larger path for the electrons to reach the reaction. However, the electronical electrical distribution is equipotential

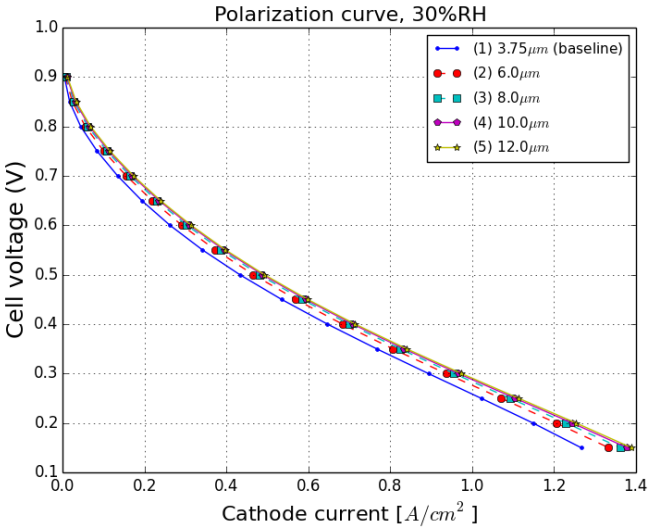

Figure 3.16: Polarization curves from PEMFCs with different thickness and platinum loading cell's cathodes. 30%RH.

in all the cathode catalyst layer media and most of the reaction occurs at PEM-CL interface such that H^+ does not reach to travel the length of the CL.

In order to understand the internal effects of the thickness, simulations (2), (3) and (5) solutions are compared at 1.2 A/cm^2. The oxygen molar fraction distribution its identical in all three layers (Figure 3.18). Thus, oxygen transport seems to be independent of the thickness. However, Figure 3.19 shows a different ORR distribution with less parts of the CL being used for thicker CL. This shows proton transport into the CL is limiting. The lack of Pt utilization will elevate the PEMFC cost by increasing the platinum content without improving the performance, at least under dry conditions.

Wet, 90%RH

Independently of the catalyst layer thickness, all the experiments show that performance starts to decay when the current density is 0.95 A/cm^2. At 0.44V, the saturation level inside the CLs reaches the 55% next to the channels (Figure 3.21). It evolves to a more stable saturation distribution at 0.1V (Figure 3.22). Notice the saturation next to the channels, acting like a wall for the oxygen flux, keeps the value around 56%. This is the same maximum value found in Section 3.2 for the baseline case (with identical ink composition). Further,

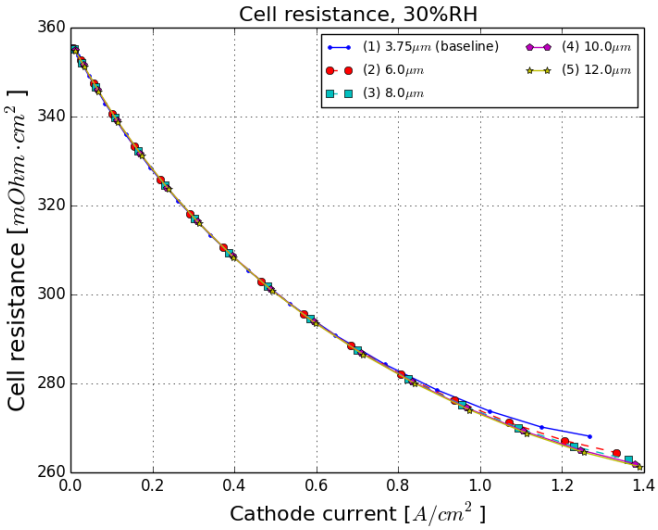

Figure 3.17: Cell resistance curves from PEMFCs with different thickness and platinum loading cell's cathodes. 30%RH.

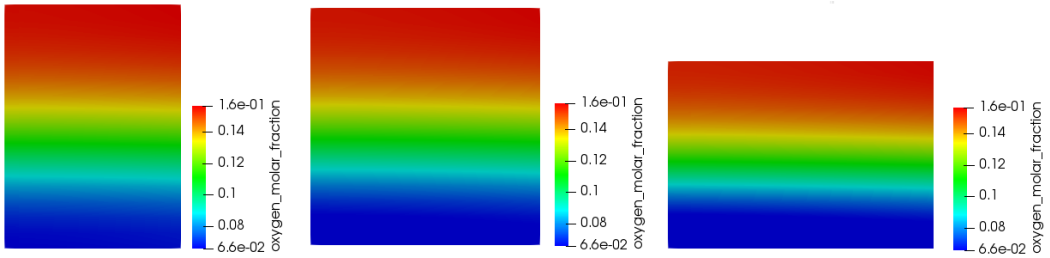

Figure 3.18: Oxygen molar fraction inside the cathode catalyst layers of experiments (2)-left, (3)-middle and (5)-right, at 1.2 A/cm^2. 30%RH.

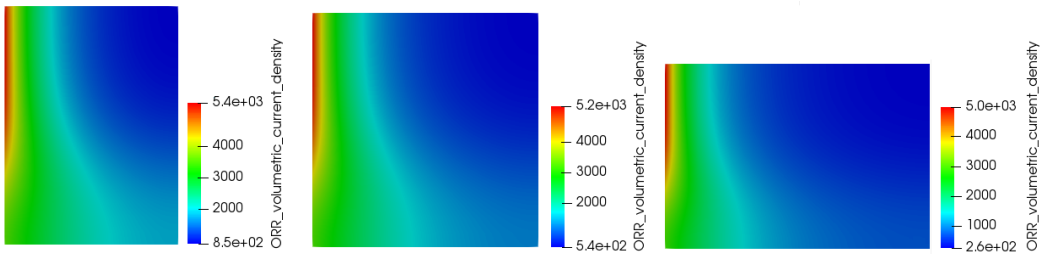

Figure 3.19: Oxygen reduction reaction volumetric current density generated inside the cathode catalyst layers of experiments (2)-left, (3)-middle and (5)-right, at 1.2 A/cm^2. 30%RH

notice how the saturation gradient inside the layer evolves differently when different thickness. When the ORR starts to decrease its kinetic, especially next to the membrane, less water is produced. Thus, the porous in this area

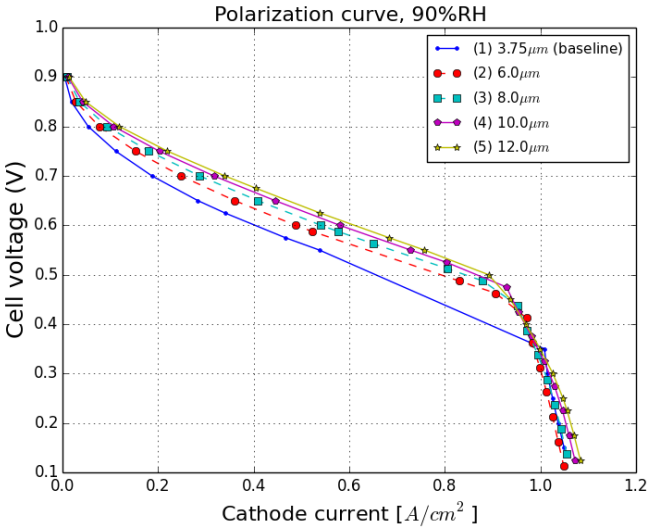

Figure 3.20: Polarization curves from PEMFCs with different thickness and platinum loading cell's cathodes. 90%RH.

starts to evacuate the liquid water stored, helped by the protonic drag. This effect makes the porous media next to the membrane to be less saturated at 0.1V and it is more significant when thicker CCLs.

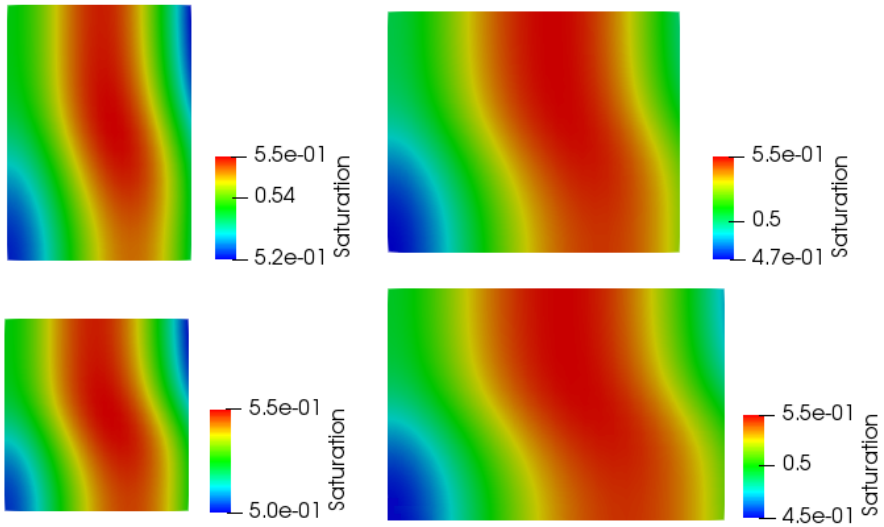

Figure 3.21: Cathode catalyst layer saturation level at 0.44V for the experiments (2);up-left, (3); down-left, (4); up-right and (5); down-right. 90% RH.

A part from the performance decay, Figure 3.20 also shows the convergence instabilities due to the two phase problem. In this case, all the simulations

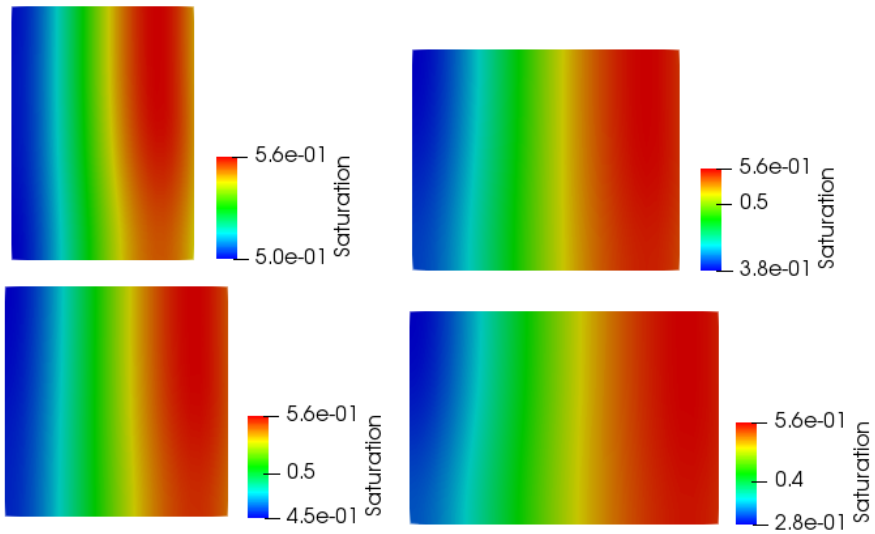

Figure 3.22: Cathode catalyst layer saturation level at 0.1V for the experiments (2);up-left, (3); down-left, (4); up-right and (5); down-right. 90% RH.

have the baseline λ_{PSD} value; no convergence-adjust is done. Thus, it is interesting to note the better convergence when the catalyst layer is thicker, i.e., experiments (1) and (2), with thinner CLs, are the ones that start to have convergence problems over 0.55 A/cm^2. No evidence is found to justify this phenomena. Parameters as saturation, relative humidity, temperature, volumetric evaporation and condensation, gas pressure are compared through the five cells and none of them can explain the instability. Liquid pressure, shown in Figure 3.24, has higher values in the first and second experiment. It could be the reason that explains the liquid water flux from cathode to anode, observed in experiments (1) and (2). The normalized water balance plot for experiment (1) is shown in Figure 3.23. However, this phenomena cannot be related with the convergence stability, as it is observed even in experiments with good convergence solutions.

Finally, numerical values for the maximum power produced by the experimented cells are summarized in Table 3.6. Again, increasing the platinum loading (in this case, by depositing more layers of ink in the CCM), just slightly increases the performance. However this change is not proportional to the amount of platinum deposited. Thus, the maximum power per unit of platinum mass decreases when increasing the cathode catalyst layer thickness.

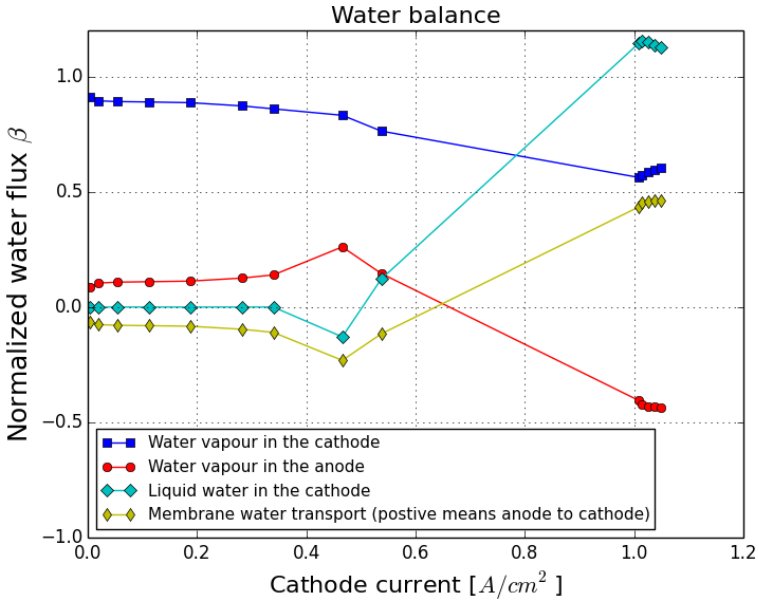

Figure 3.23: Water balance inside the cell for the experiment (1), with 3.75 μm catalyst layer thickness. 90%RH.

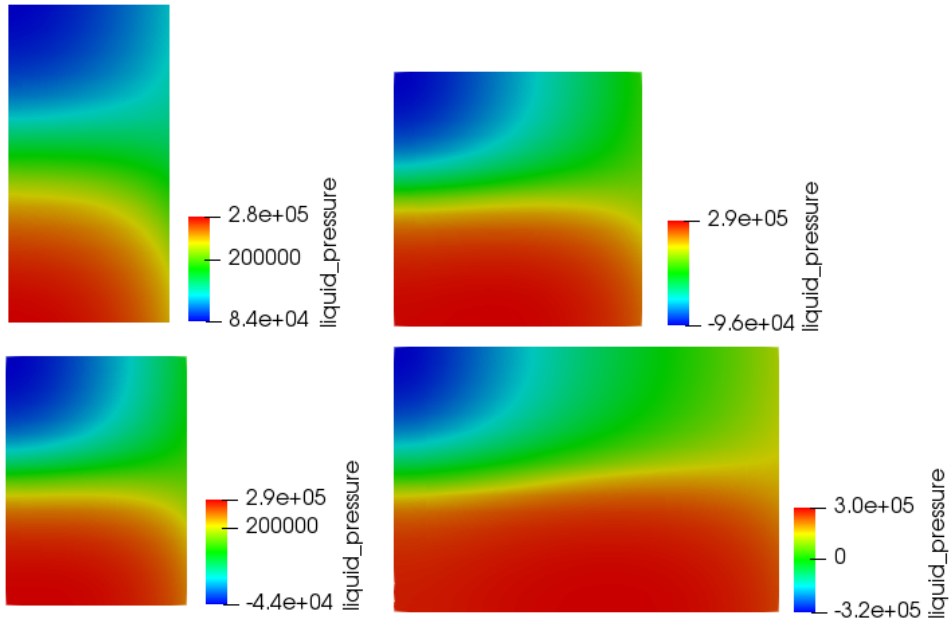

Figure 3.24: Liquid pressure in the cathode catalyst layer at 0.55 A/cm^2 for experiments (1);up-left, (2);down-left, (3);up-right and (5); down-right. 90%RH.

Table 3.6: Maximum power (W), and power per unit of Pt mass (W/mg_{Pt}) offered by the experimented PEMFCs under the specified humidity conditions; 30, 50, 75 and 90%RH.

	P_{max}	30%RH	90%RH
Case (1)- 3.75μm (BL)	(W/mg_{Pt})	2.56	3.71
	(W)	1.07	1.56
Case (2)- 6μm	(W/mg_{Pt})	1.68	2.50
	(W)	1.13	1.68
Case (3)- 8μm	(W/mg_{Pt})	1.29	1.91
	(W)	1.15	1.72
Case (4)- 10μm	(W/mg_{Pt})	1.04	1.58
	(W)	1.17	1.77
Case (5)- 12μm	(W/mg_{Pt})	0.88	1.33
	(W)	1.18	1.78

3.4 Current collector and channel width

The channel geometry does not only affect the air and hydrogen flow fields in the diffusion layers, they also influence the cell electronic conductivity as they are responsible for the electron collection and distribution in the anode and cathode, respectively. Further, they add structural integrity to the cell.

In this Thesis, a parallel channel configuration is used. The two main parameters that characterize its geometry are the channel and current collector widths. Figure 3.25 shows an schematic to clarify the meaning of this dimensions. The multi purpose of the bipolar plates and the different role of each part, leads to an interesting trade of between each dimension which is the purpose of this section to study.

3.4.1 Study

Eight different cells are modeled for this study. All of them have an identical MEA but different cathode channel and current collector widths, introducing to each model different boundary conditions. Table 3.7 shows the channel dimensions selected for each cell. The same experiment conditions described in Section 2.3.1, but different hydrogen and air relative humidities, are reproduced over the eight cells. In order to compare the trade off importance under wet and dry cell conditions, 30%RH and 90%RH conditions are applied to the

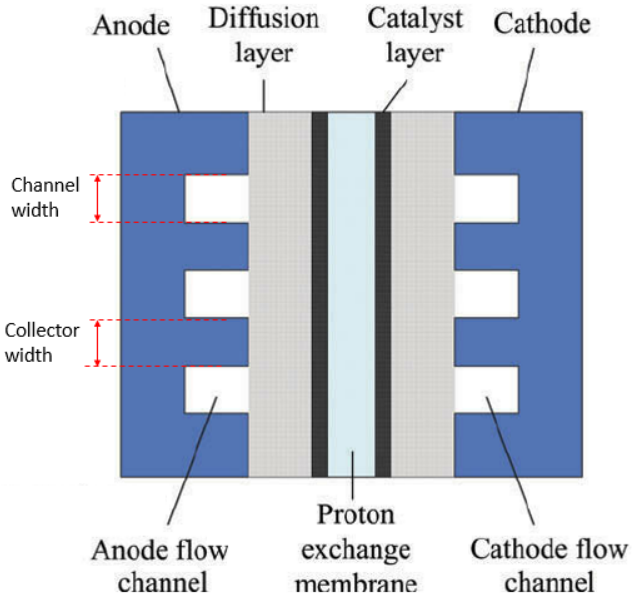

Figure 3.25: Parallel channel PEMFC schematic.

reactants in each experiment. The results are discussed below.

Table 3.7: Channel and current collector widths used in the eight different cells.

Experiment	Current col. (cm)	Channel (cm)
0 (baseline)	0.083	0.082
1	0.05	0.1
2	0.1	0.05
3	0.05	0.05
4	0.13	0.13
5	0.07	0.07
6	0.05	0.13
7	0.08	0.13

3.4.2 Results

Dry, 30%RH

The polarization and cell resistance curves from the experiments in Table 3.7 are shown in Figures 3.26 and 3.27. The cell performance is very similar even though the cell resistance is quite affected. The differences in the cell resistance are influenced by the electronic conductivity variations induced by the current collector or land width.

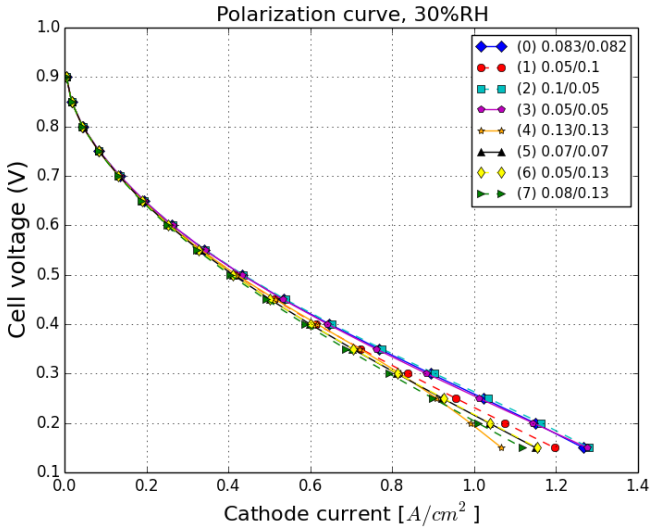

Figure 3.26: Different channel geometries cell's polarization curves for an experiment with 30%RH condition.

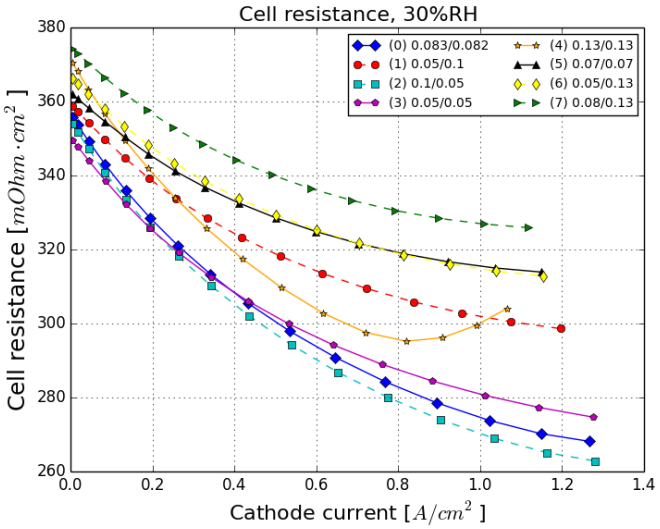

Figure 3.27: Different channel geometries cell's resistance curves for an experiment with 30%RH condition.

The oxygen molar fraction distribution in the catalyst layer, Figure 3.28, is strongly dependent on the channel geometry. Between experiment (3) and (7) it is easy to identify that channel is thicker in experiment (7) so the area with high oxygen concentration is larger. Further, between experiments (4) and (5), even the ratio channel/land is 1 in both cases, experiment (5) reach more uniformity in the oxygen distribution thanks to the narrower channels

and collectors.

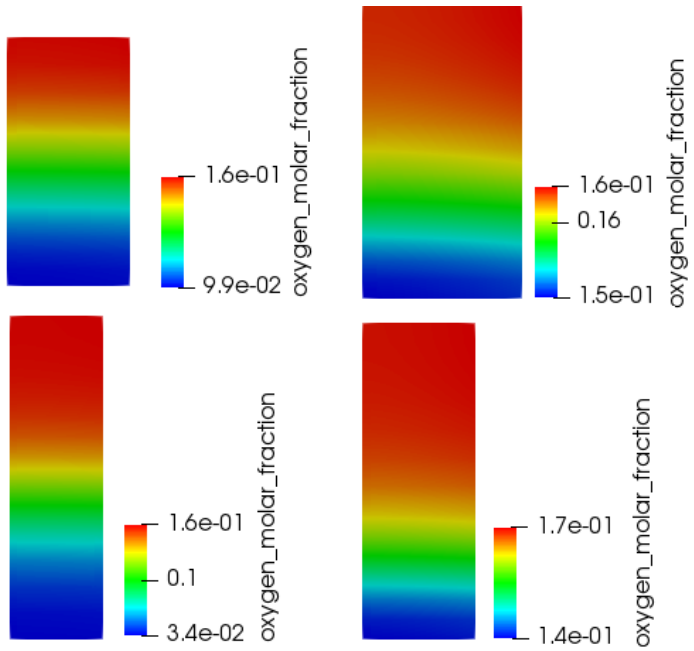

Figure 3.28: Oxygen molar fraction in the catalyst layer for the experiments (2); up-left, (4); down-left, (5); up-right and (7); down-right at 0.9 A/cm^2. 30%RH.

Wet, 90%RH

The current collector and channel widths seem to have a larger influence at high relative humidity. In this case, 90%RH. Figures 3.29 and 3.30 show the polarization and cell resistance curves of all the experiments overlapped in order to compare the results. At high current densities, the mass transport zone differences are significant. Again, the convergence is reached by adjusting the catalyst layer porous interconnectivity. The value used to all the experiments except case (7) is λ_{PSD}=3. For case (7); λ_{PSD}=4.5.

Discussions in this section are based on the mass transport region; where the saturation introduces a limiting current in the performance that make interesting the study. Experiments (1), (3) and (6), all of them having same current collector width; 0.05 cm, are compared at 0.25V in order to see the role of the channel width. Firstly, taking a look into the saturation level (Fig-

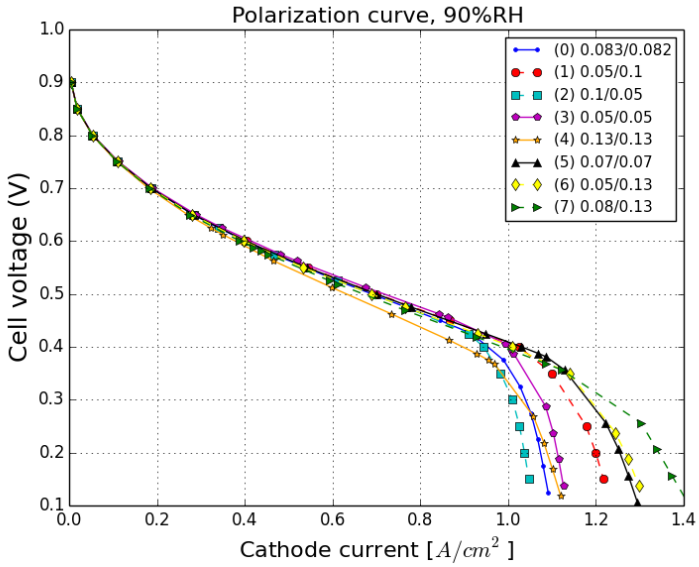

Figure 3.29: Different channel geometries cell's polarization curves for an experiment with 90%RH condition.

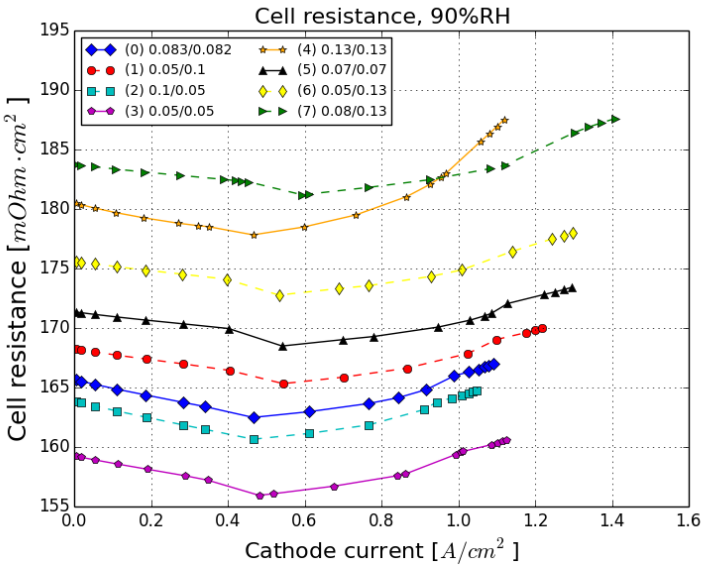

Figure 3.30: Different channel geometries cell's resistance curves for an experiment with 90%RH condition.

ure 3.32), it can be noticed that maximum saturation level, around 56%, is independent from the channel width. This is proved for all the experiments. Figure 3.33 shows the saturation level around 0.1V for all the experiments. All of them, except the number (4) with 0.13/0.13 cm, present a very similar sat-

uration map inside the CCL. This support the fact that maximum saturation level is not affected by the channel width. However, it does affect the performance. That is why some channel/current collector widths configurations obtain higher current densities. A clear example of this fact is the comparison between experiments (1), (3) and (6) at 0.25V. Figure 3.34 shows the ORR current density produced at this point by the three cells. It demonstrate that wider channels ease the oxygen supply and increase the reaction rate. Another explanation for this performance difference is the liquid water evacuation rate. Figure 3.31 shows that experiment (6) with wider channel takes higher current density to reach the same amount of liquid water. This is due to better water evacuation with larger channels.

Comparing experiments with same channel widths, i.e., (4), (6) and (7), it can be noticed that current collector width also has influence in the performance response. As shown in Figure 3.29, experiment (4) has the lowest limiting current. This is due to the bad uniformity in the oxygen distribution between two channels. The current collector thickness, 0.13 cm, limits the oxygen ability to reach the areas under the land. Thus, reducing the reaction rate. This phenomena is the same shown in Figure 3.28. Simulations (6) and (7), both improve the performance by reducing the land thickness to 0.05 and 0.08 cm, respectively. It ends up with another trade off; the electrical conductivity. That is why case (6) reduces its performance by increasing its resistance. It can be said, fixing the channel width to 0.13 cm, the optimal current collector thickness is between 0.05 and 0.13 cm.

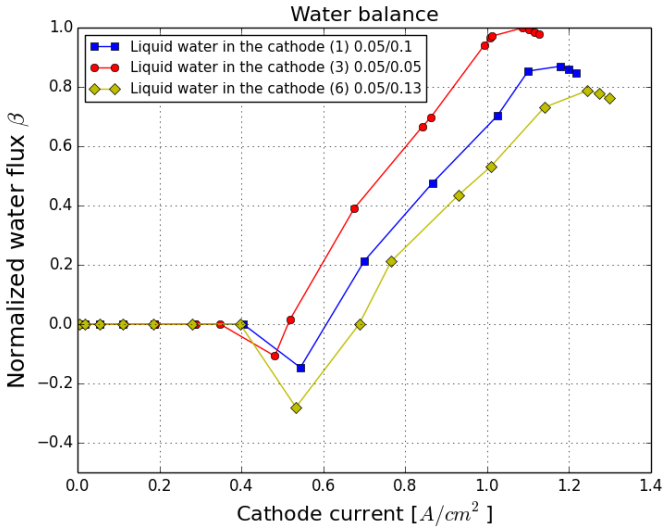

Figure 3.31: Normalized liquid water in the cathode catalyst layer for experiments (1), (3) and (6), from left to rigth. 90%RH.

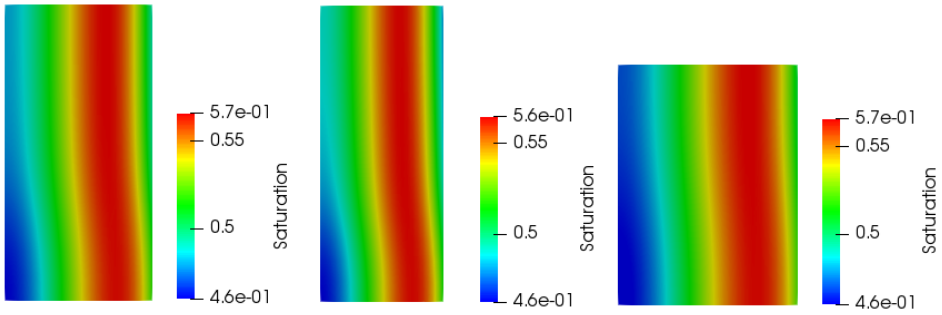

Figure 3.32: Catalyst layer saturation level for the experiments (1), (3) and (6), from left to right. 90%RH.

3.5 Electrolyte loading

The catalyst layer is composed by black carbon, platinum, electrolyte and void (referred to the absence of previous). The electrolyte used for this thesis is Nafion®. Each component in the CL has a different function when the cell is operating, e.g., electrolyte is responsible for the protonic conduction, carbon for the electronic conduction and void allows the vapor and reactants to flow. In this case, electrolyte loading is studied as it has an interesting trade off with the amount of void part in the catalyst layer.

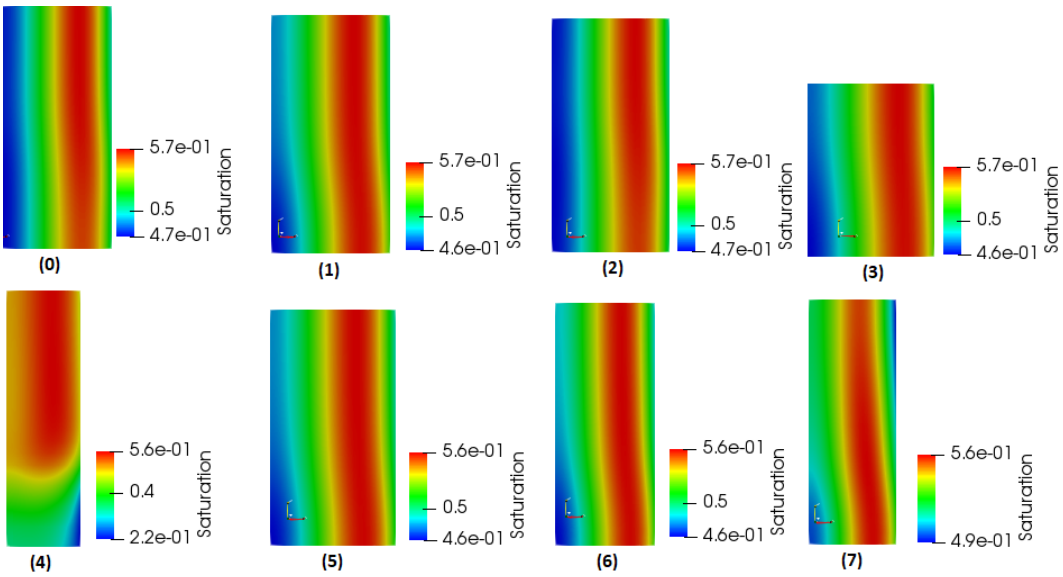

Figure 3.33: Cathode catalyst layer saturation level at 0.1V for the experiments (0), (1), (2), (3), (4), (5), (6) and (7). 90%RH.

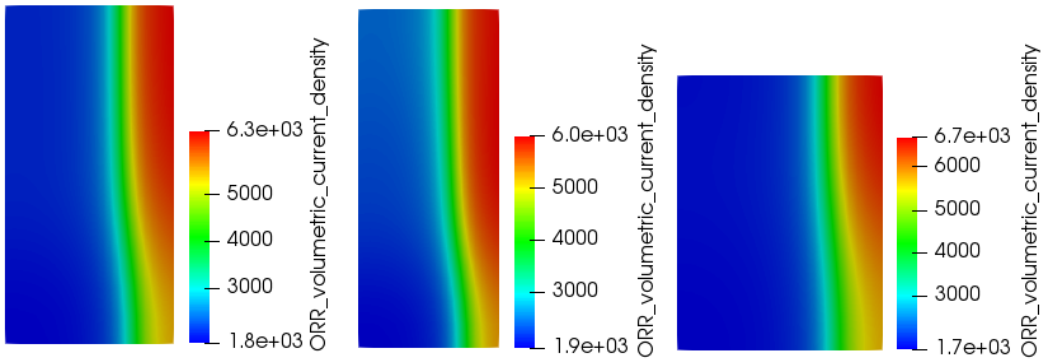

Figure 3.34: Oxygen reduction reaction volumetric current density inside the catalyst layer for the experiments (1), (3) and (6), from left to right. 90%RH.

3.5.1 Study

Three different cells are modeled for this study. All of them have, as the only difference, the cathode catalyst layer electrolyte content. The Nafion weight loading fraction in the CL, $w_{electrolyte}$, are respectively; 20, 30 and 40%. Cathode catalyst layers volume fractions for each case are computed with expressions shown in Appendix B.2 and summarized in Table 3.8. The same experiment conditions described in Section 2.3.1, but different hydrogen and air relative humidities, are reproduced over the three cells. 30%RH and

90%RH conditions are applied to the reactants in each experiment. The results are discussed below.

Table 3.8: Catalyst layer volume fractions depending on electrolyte weight loading fraction.

Experiment	$w_{electrolyte}$	ϵ_{solid}	$\epsilon_{electrolyte}$	ϵ_{void}
(1)	20%	0.2676	0.0875	0.6449
(2)	30% (BL)	0.2676	0.1500	0.5824
(3)	40%	0.2676	0.2333	0.4991

3.5.2 Results

30%RH

The electrolyte loading is, among the parameters studied in this Thesis, the one that has more influence in the dry case. The protonic conductivity, as said at some point before, is widely improved when the electrolyte is humidified. Thus for dry cases, the resistance to the protons transport becomes a limiting factor in the cell performance due to the ohmic losses. Figures 3.35 and 3.36 show the performance and the cell resistance curves for the three experiments that proves this fact. Further, taking a look into the protonic electrical potential inside the catalyst layer at 1.0 A/cm^2 when electrolyte loading is 20 and 30%wt, it can be noticed a different potential gradient. The potential gradient appears when the transport resistance induces ohmic losses. Thus, the wider gradient, the more ohmic losses. The scale values in Figure 3.37 show that the case with less amount of Nafion, ends up with higher ohmic losses, responsible for the performance decrease.

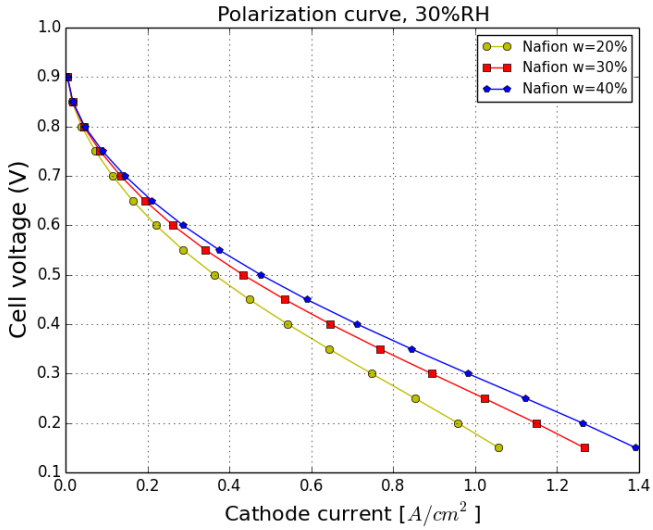

Figure 3.35: Overlapped polarization curves for $w_{electrolyte} = 20, 30$and 40% and reactants humidity condition; 30%RH.

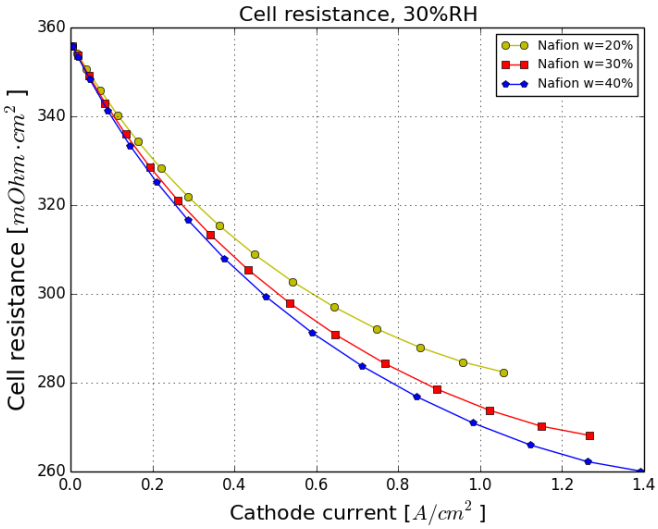

Figure 3.36: Overlapped cell resistance curves for $w_{electrolyte} = 20, 30 and 40\%$ and reactants humidity condition; 30%RH.

90%RH

The wet cases for the Nafion loading study also show convergence issues that are solved, as in previous sections, adjusting the catalyst layer porous interconnectivity. In this case, for 20 and 30%wt, $\lambda_{\text{PSD}} = 6$ is used. For 40%, the good convergence is found for $\lambda_{\text{PSD}} = 4.5$.

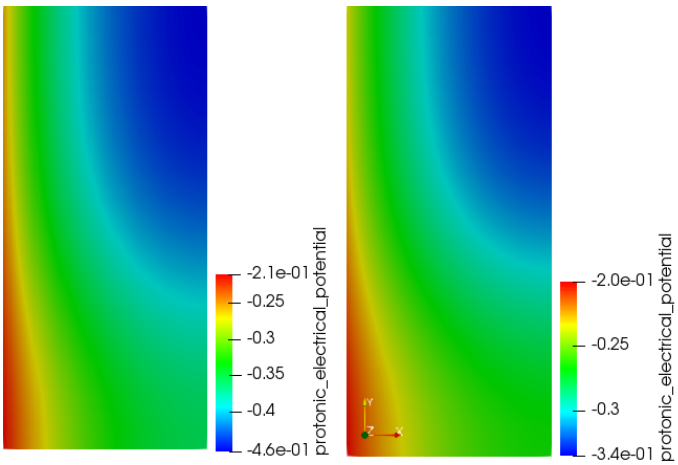

Figure 3.37: Catalyst layer protonic electrical potential at 1.0 A/cm^2 for experiments with 20 (left) and 30%wt (right) electrolyte loading. 30%RH.

Figure 3.38 shows the performance curves for the studied cases. For the same reason that electrolyte loading has wide influence in dry cases, it does not have it for the wet ones. The protonic conductivity is not a limiting factor when the Nafion is humidified. Thus, the performance variance when changing the electrolyte loading is not that significant. However, even the overall cell resistance is the same in all three experiments, Figure 3.39 show slightly differences between the protonic electrical potential gradients inside the different cathode catalyst layer. In the other hand, wet cases deal with saturation issues that limit the current. The trade off between electrolyte loading and void part in the catalyst layer makes possible a different void fraction (ϵ_{void}) between the experiments. Concretely, between experiment (1) and (3), there is a 15% of the CL volume that changes from void to electrolyte part. This has an effect on the maximum saturation level. Figure 3.40 proves that decreasing the amount of Nafion, the porous media is able to retain more liquid water without collapse the performance.

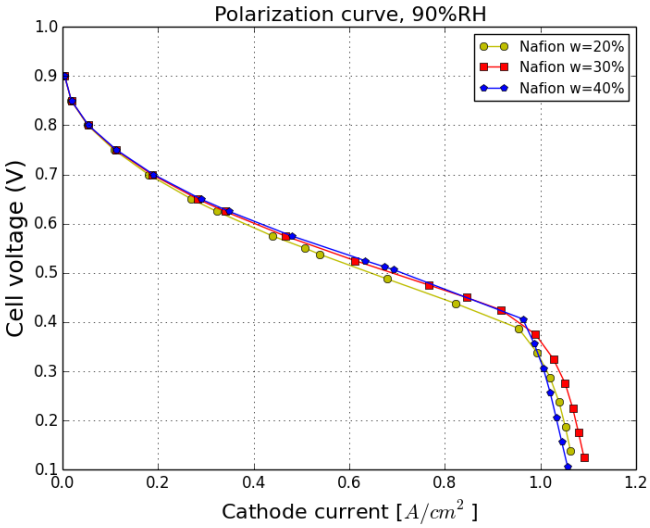

Figure 3.38: Overlapped polarization curves for $w_{electrolyte} = 20, 30 and 40\%$ and reactants humidity condition; 90%RH.

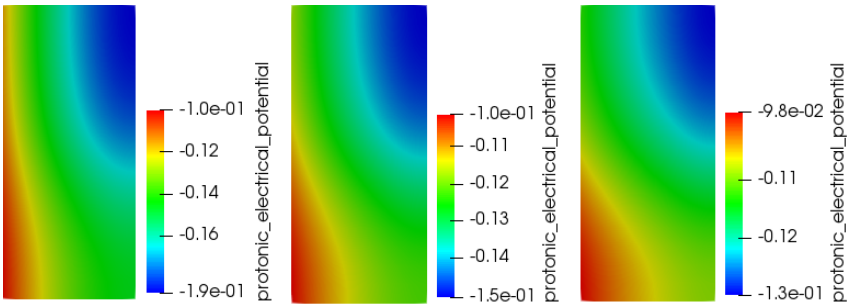

Figure 3.39: Protonic electrical potential inside the cathode catalyst layer at 0.12V for experiments (1)-20%wt, (2)-30%wt and (3)-40%wt electrolyte loading, from left to right. 90% RH.

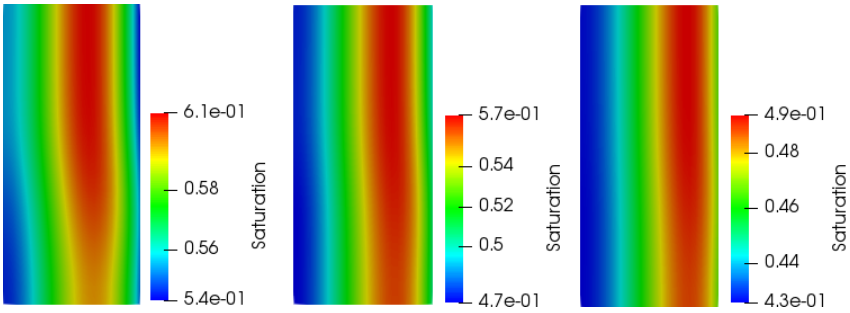

Figure 3.40: Cathode catalyst layer saturation level at 0.12V for the experiments (1)-20%wt, (2)-30%wt and (3)-40%wt electrolyte loading, from left to right. 90% RH.

3.6 Discrete graded Pt/C distribution in the cathode catalyst layer

Some literature report a performance improvement when the cathode catalyst layer composition (platinum, carbon, electrolyte and void) is varied in the space. Thus, a non-homogeneous distribution of the different materials in the layer is studied there.

The goal of this section is to prove, through the two phase flow model presented in Section 2.1, how the performance can be improved with a discrete 1D graded Pt/C distribution in the cathode catalyst layer. The experiment simulated is designed to be doable with the current ESDLab technology.

3.6.1 Study

The study is conformed by six experiments, paired in groups. Two experiments have a 12 μm thickness CCL, two more have a 6 μm and the other two a 3.75 μm one (as the baseline). In each pair, one CCL has a graded Pt/C distribution in the through-plane direction (schematized in Figure 3.41) and the other has an homogeneous distribution. The reason for thicker layers (6 and 12 μm) is to see if it affects the difference between the graded and non-graded distribution. The current collector and channel width selected, 0.08/0.13 cm, is the configuration that gives better mass transport performance in Section 3.4, for wet cases. The reason to select this configuration is to prove if graded CCL is able to improve even more this performance.

The details of each studies are summarized in Table 3.9. The parameters not specified in this table are supposed to be the ones reported in Tables 2.8 and 2.9.

Table 3.9: Catalyst layer volume fractions depending on electrolyte weight loading fraction.

Experiment	Thickness (μm)	Graded	Pt/C (%)	Current col./Channel width (cm)
(1)	12	Yes	Figure 3.41	0.08/0.13
(2)		No	40	0.08/0.13
(3)	6	Yes	Figure 3.41	0.08/0.13
(4)		No	40	0.08/0.13
(5)	3.75	Yes	Figure 3.41	0.08/0.13
(6)		No	40	0.08/0.13

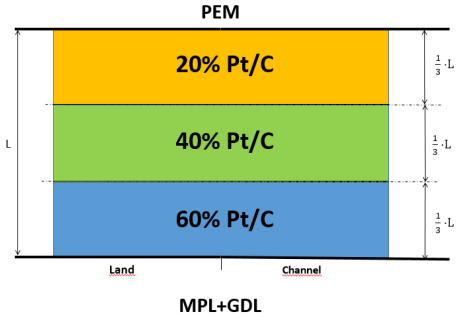

Figure 3.41: Cathode catalyst layer discrete 1D Pt/C graded distribution proposed for this study.

3.6.2 Results

Table 3.10: Maximum power (W), and power per unit of Pt mass (W/mg_{Pt}) offered by the experimented PEMFCs under the specified humidity conditions; 30, 50, 75 and 90%RH.

		30%RH	50%RH	75%RH	90%RH
Exp. (1)	(W/mg_{Pt})	0.68	1.02	1.32	1.31
	(W)	0.91	1.37	1.78	1.76
Exp. (2)	(W/mg_{Pt})	0.77	1.12	1.40*	1.26
	(W)	1.03	1.50	1.89*	1.70
Exp. (3)	(W/mg_{Pt})	1.36	1.98	2.47	2.50
	(W)	0.91	1.33	1.66	1.68
Exp. (4)	(W/mg_{Pt})	1.49	2.10	2.81*	2.53
	(W)	1.00	1.41	1.89*	1.70
Exp. (5)	(W/mg_{Pt})	2.14	3.03	4.24	4.26
	(W)	0.9	1.27	1.78	1.79
Exp. (6)	(W/mg_{Pt})	2.29	3.16	4.48*	3.81
	(W)	0.96	1.33	1.88*	1.60

*; approximated value (bad convergence)

The results obtained in this section, based in terms of maximum power and maximum power per unit of platinum mass, are summarized in Table 3.10. Notice how this results match with the ones obtained in Section 3.3, concluding that increasing the cathode catalyst layer thickness does not improve the cell performance, ending up with lower values of power per platinum loading. Thus, the discussion is basically centered in simulations (5) and (6), with 3.75 μm CCL thickness. Graded configuration increases the maximum power in the 90%RH case only worsen the performance in dryer cases (30, 50 and 75%RH). As shown in previous sections, the reaction tends to occur next to the membrane in dry cases and next to the MPL-GDL in wet cases. The experimented graded composition deposit more platinum next to the diffusion media. This is the reason for the improvement just for wet cases.
Comparing the results between the experiment (5) and the baseline presented in Section 3.1, it can be noticed an improvement in wet cases performance. The only two differences between both experiments are the channel width and the %Pt/C distribution inside the cathode catalyst layer. However, the maximum power increases from 1.56 W to 1.79 W when 90%RH in the reactants. It means a 15% increment in the maximum without changing the total amount of platinum loading. Making the same comparison between the baseline and experiment (6) (that have a platinum homogeneous distribution in the CCL), the improvement in power is from 1.60 W to 1.88 W, when 75%RH. It means a 20% of improvement in maximum power, by just changing the channel width.

The performance and cell resistance curves resulting from the comparison between the experiment (5) and the baseline are shown in Figures 3.42 and 3.43, respectively. Notice the cell resistance is lower in the baseline case, for all the humidity cases. This is mostly due to the channel and land configuration, that offers less conductivity area per bipolar plate surface. Figures 3.27 and 3.30 show this phenomena.

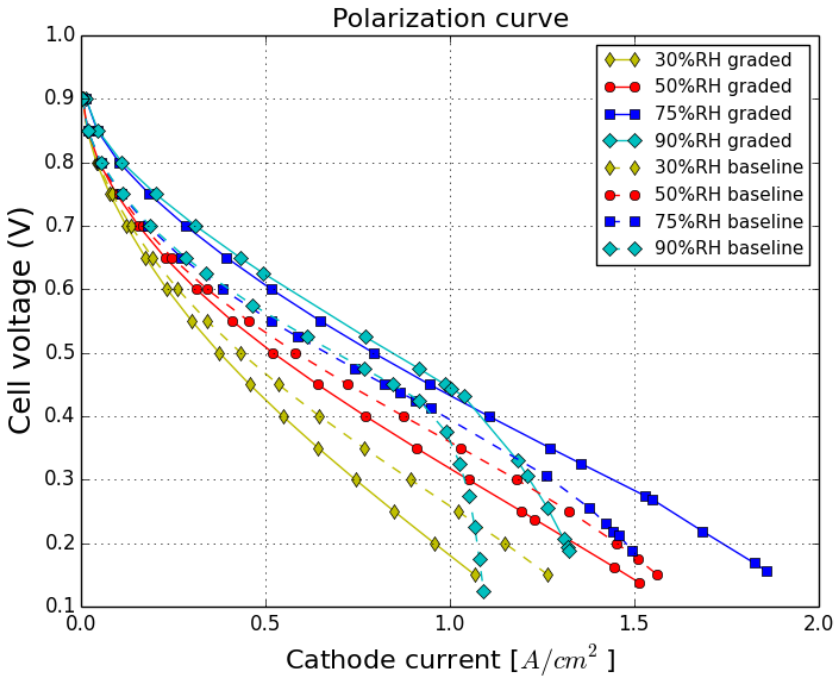

Figure 3.42: Baseline and graded CCL polarization curves for 30, 50, 75 and 90%RH conditions.

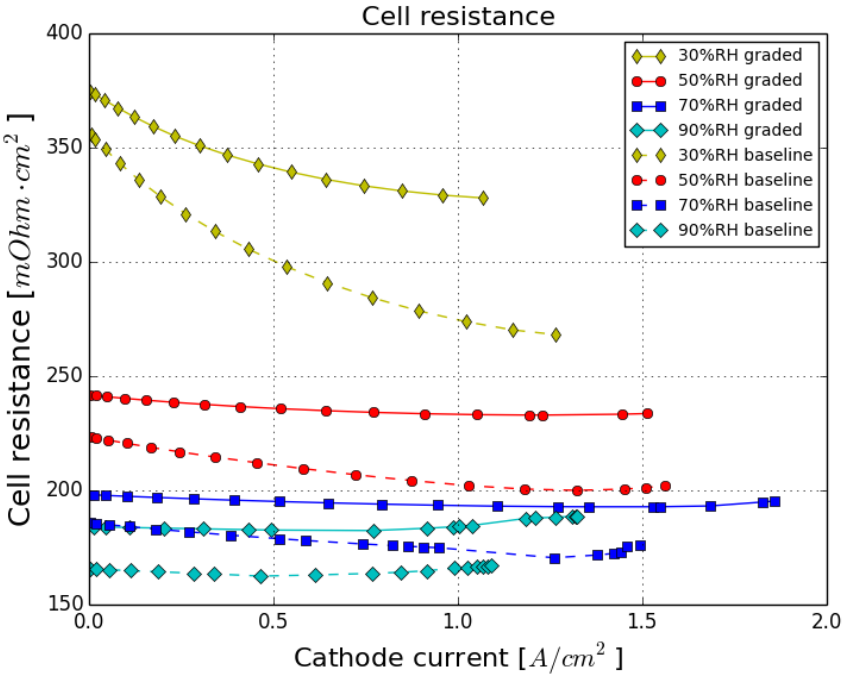

Figure 3.43: Baseline and graded CCL polarization curves for 30, 50, 75 and 90%RH conditions.

Chapter 4

Conclusion

Low loading cathode catalyst layers result to always offer higher power per unit of platinum mass ratios. This is proved by modifying the ink %Pt/C composition and also by varying the CCL thickness. In both cases the increase of platinum loading in the cell does not report enough performance improvement to increase or, at least keep, the W/mg_{Pt}. Thus, increase the Pt loading up to 0.1 mg/cm^2 ends up being hardly worth it. From the variable thickness experiment, even it is not a topic deeply treated in this Thesis, a convergence improvement is observed when thicker CCLs are defined in the simulation.

In the other hand, a sudden performance decay, induced in the wet cases by the cathode catalyst layer porous media saturation, is observed. This fact matches with experimental data measured in ESDLab under similar conditions. However, it is not proven experimentally for the case studied in this Thesis and it could be a future line to study. It is observed a maximum saturation value related with the void volume fraction in the CCL. The higher void volume fraction, the higher maximum saturation value and thus, the higher current density is able to be produced till the maximum saturation is reached. It is found that this maximum saturation level is independent on the cathode catalyst layer thickness and channel width. Experiments that variate the thickness from 3.75 μm to 12 μm show same maximum saturation level when cell performance starts to decay drastically; around 0.95 A/cm^2, and when reaches the low voltage; 0.1V. Further, experimenting with identical MEAs

and different channel widths also result with same maximum saturation level.

It is observed an increment of performance when humidified reactants are supplied to the cell. However the saturation becomes an important issue when high current is demanded. Thus, the channel and current collector widths takes importance in order to improve the mass transport performance. For this purpose, 0.13 *cm* channel width is the configuration that offers higher current densities, among the studied ones.

Grading the cathode catalyst layer platinum distribution instead of distribute it homogeneously only increases the maximum power of the cell when 90%RH in the reactants. However, it worsen the performance for lower relative humidities. The maximum power supplied by the cell is very similar when using 75%RH and 90%RH reactants. However, the higher humidity, the more saturation issues. Thus, because raising the humidity conditions over 75% does not report better performance, it is proposed to use this %RH in the reactants and non-graded CCL is necessary because does not improve the performance.

Finally, as a future line for this work, a validating experiment is proposed in order to verify the channel width affectation and prove if it actually improves the cell performance and maximum power when reactants are supplied with 75%RH.

Bibliography

[1] J. Zhou, S. Shukla, A. Putz, and M. Secanell, "Analysis of the role of the microporous layer in improving polymer electrolyte fuel cell performance," *Electrochimica Acta*, 2018.

[2] A. Baroutaji, J. Carton, M. Sajjia, and A. G. Olabi, "Materials in pem fuel cells," 10 2015.

[3] *Fuel Cell System Explained*. John Wiley & Sons Ltd, 2018.

[4] M. Secanell, *Computational Modeling and Optimization of Proton Exchange Membrane Fuel Cells*. PhD thesis, University of Victoria, 2008.

[5] J. Zhou, A. Putz, and M. Secanell, "A mixed wettability pore size distribution based mathematical model for analyzing two-phase flow in porous electrodes," *Journal of The Electrochemical Society*, 2017.

[6] J. Zhou, D. Stanier, A. Putz, and M. Secanell, "A mixed wettability pore size distribution based mathematical model for analyzing two-phase flow in porous electrodes: II. model validation and analysis of micro-structural parameters," *Journal of The Electrochemical Society*, 2017.

[7] F. C. Centibas, S. G. Advani, and A. K. Prasad, "Optimization of polymer electrolyte membrane fuel cell catalyst layer with bidirectionally-graded composition," *Electrochimica Acta*, 2015.

[8] Z. Xie, T. Navessin, K. Shi, R. Chow, Q. Wang, D. Song, B. Andreaus, M. Eikerling, Z. Liu, and S. Holdcrofta, "Functionally graded cathode catalyst layers for polymer electrolyte fuel cells ii. experimental study of

the effect of nafion distribution," *Journal of The Electrochemical Society*, 2005.

[9] M. Secanell, K. Karan, A. S. a, and N. Djilali, "Multi-variable optimization of PEMFC cathodes using an agglomerate model," *Electrochimica Acta 52 (2007) 6318–6337*, 2007.

[10] Muthukumara, P.Karthikeyanb, M.Vairavela, C.Loganathana, S.Praveenkumara, and A. Kumarb, "Numerical studies on PEM fuel cell with different landing to channel width of flow channel," *Electrochimica Acta*, 2007.

[11] M. Moore, P. Wardlaw, P. Dobson, J. Boisvert, A. Putz, R. Spiteri, and M. Secanell, "Understanding the effect of kinetic and mass transport processes in cathode agglomerates," *Journal of the Electrochemical Society*, 2014.

[12] J. X. Wang, T. E. Springe, and R. R. Adzic, "Dual-pathway kinetic equation for the hydrogen oxidation reaction on pt electrodes," *Joural of the Electrochemical*, 2006.

[13] M. Secanell, A. Putz, S. Shukla, P. Wardlaw, M. Bhaiya, L. Panta, and M. Sabharwal, "Mathematical modeling and experimental analysis of thin, low-loading fuel cell electrodes," *ECS Transactions*, 2015.

[14] J. Bear, "Dynamics of fluids in porous media," *Dover Publications*, 2013.

[15] C. Bosanquet, "Lv. on the flow of liquids into capillary tubes," *The London, Edinburgh, and Dublin Philosophical Magazine and Journal of Science*, 2006.

[16] P. García-Salaberri, J. Gostick, G.Hwang, A. Weber, and M.Vera, "Effective diffusivity in partially-saturated carbon- fiber gas diffusion layers: Effect of local saturation and application to macroscopic continuum models," *Journal of Power Sources*, 2015.

[17] M. Eikerling and A. A. Kornyshev, "Modeling the performance of the cathode catalyst layer of polymer electrolyte fuel cells," *Journal of Electroanalytical Chemistry*, 1998.

[18] M. Bhaiya, A. Putz, and M. Secanell, "Analysis of non-isothermal effects on polymer electrolyte fuel cell electrode assemblies," *Electrochimica Acta*, 2014.

[19] S. Shukla, D. Stanier, M. Saha, B. Zahiri, M. Tam, J. Stumper, and M. Secanell, "Characterization of inkjet printed electrodes with improved porosity," *ECS Transactions*, 2017.

[20] S. Shukla, K. Domican, K. Karan, S. Bhattacharjee, and M. Secanell, "Analysis of low platinum loading thin polymer electrolyte fuel cell electrodes prepared by inkjet printing," *Electrochimica Acta*, 2015.

[21] M. Khandelwal and M. Mench, "Direct measurement of through-plane thermal conductivity and contact resistance in fuel cell materials," *J. Power Sources*, 2006.

[22] T. Soboleva, K. Malek, Z. Xie, T. Navessin, and S. Holdcroft, "Pemfc catalyst layers: the role of micropores and mesopores on water sorption and fuel cell activity," *ACS Applied Materials & Interfaces*, 2011.

[23] M. Sathya, A. Becker, and J. Weidner, "Diffusion of water in nafion 115 membranes," *J. Electrochem. Soc.*, 2000.

[24] A. Makoto, T. Navessin, Z. Xie, F. Barbara, and S. Holdcroft, "Correlation of in situ and ex situ measurements of water permeation through nafion NRE211 proton exchange membranes," *J. Electrochem. Soc.*, 2009.

[25] Y. Liu, M. Murphy, D. Baker, W. Gu, C. Ji, J. Jorne, and H. Gasteiger, "Proton conduction and oxygen reduction kinetics in PEM fuel cell cathodes: effects of ionomer-to-carbon ratio and relative humidity," *J. Electrochem. Soc.*, 2009.

[26] T. Bekkedahl, "In-plane conductivity testing procedures and results, in: Doe high," *Temperature Membrane Working Group Meeting*, 2007.

[27] S. Kim and M. Mench, "Investigation of temperature-driven water transport in polymer electrolyte fuel cell: thermo-osmosis in membranes," *J. Membr. Sci.*, 2009.

[28] M. Khandelwal and M. Mench, "Direct measurement of through-plane thermal conductivity and contact resistance in fuel cell materials," *J. Power Sources*, 2006.

[29] *SIGRACET® Gas Diffusion Layers for PEM Fuel Cells, Electrolyzers and Batteries.*

[30] I. Nitta, O. Himanen, and M. Mikkola, "Thermal conductivity and contact resistance of compressed gas diffusion layer of pem fuel cell," *Fuel Cells. From Fundamental to Systems*, 2008.

[31] G. Karimi, X. Li, and P. Teertstra, "Measurement of through-plane effective thermal conductivity and contact resistance in pem fuel cell diffusion media," *Electrochimica Acta*, 2010.

[32] P. Teertstra, G. Karimi, and X. Li., "Measurement of in-plane effective thermal conductivity in pem fuel cell diffusion media," *Electrochimica Acta*, 2011.

[33] A. Pfrang, "X-ray computed tomography of gas diffusion layers of pem fuel cells: Calculation of thermal conductivity," *International Journal of Hydrogen Energy*, 2010.

[34] N. Zamel, J. Becker, and A. Wiegmann, "Estimating the thermal conductivity and diffusion coefficient of the microporous layer of polymer electrolyte membrane fuel cells," *Journal of Power Sources*, 2012.

[35] L. Pant, S. Mitra, and M. Secanell, "Absolute permeability and knudsen diffusivity measurements in pemfc gas diffusion layers and microporous layers," *Journal of Power Sources*, 2012.

[36] J. T. Gostick, M. A. Ioannidis, M. W. Fowler, and M. D. Pritzker, "Wettability and capillary behavior of fibrous gas diffusion media for polymer electrolyte membrane fuel cells," *Journal of Power Sources*, 2009.

[37] J. T. Gostick, M. W. Fowler, M. A. Ioannidis, M. D. Pritzker, Y. M. Volfkovich, and A. Sakars, "Capillary pressure and hydrophilic porosity in gas diffusion layers for polymer electrolyte fuel cells," *Journal of Power Sources*, 2006.

[38] M. Eikerling, "Water management in cathode catalyst layers of pem fuel cells a structure-based model," *Journal of the Electrochemical Society*, 2006.

[39] A. Weber, "Improved modeling and understanding of diffusion-media wettability on polymer-electrolyte-fuel-cell performance," *Journal of Power Sources*, 2010.

[40] S. Shukla, D. Stanier, M. Saha, J. Stumper, and M. Secanell, "Analysis of inkjet printed pefc electrodes with varying platinum loading," *Journal of The Electrochemical Society*, 2016.

Appendix A

Parametric study

In order to better understand the implication of each variable in the PEMFC performance, a parametric study is done for the parameters listed in Table A.3. The table shows the original parameter value (from the model reported by J.Zhou et. al., [1]) and four values firstly selected for the parametric study and based, the most, in the literature or ESDLab experience somehow. The values in parenthesis are chosen after the first study in order to get a better conclusions in a narrower range of values. All the cases are studied under two different operating conditions; dry (80^{o}C, 30%RH) and wet (60^{o}C, 90%RH). Note that possibles interactions or correlations between parameters are not shown in this study.

Table A.1: Model parameters.

Parameter		**Value**	**Reference**
Conditions			
Breakthrough capillary press. GDL/channel interface;	p_{BT}	5000 Pa	[5]
Constant cap. press. BC,	k_{BT}	0.005 Pa	ESDLab
Water surface tension,	γ	0.064 N/m	Value for 80 ^oC.
Carbon black density,	ρ_{carbon}	1.25 g/cm^3	Estimated CL thck.
Platinum density,	ρ_{Pt}	21.5 g/cm^3	Physical constant
Electrolyte density,	$\rho_{electrolyte}$	2.0 g/cm^3	Nafion®
Dimensions			
Current collector width		0.1 cm	ESDLab value
Channel width		0.1 cm	ESDLab value

Cathode CL thickness	CCL_{thk}	4.2 μm	Estimated[1]
Anode CL thickness	ACL_{thk}	1.96 μm	Proportioncal to CCL
GDL thickness	GDL_{thk}	$1.203 \cdot 10^{-2}$ cm	Estimated from [29]
MPL thickness	MPL_{thk}	$6.5 \cdot 10^{-3}$ cm	Estimated from [29]
Membrane thickness	PEM_{thk}	$2.5 \cdot 10^{-3}$ cm	NRE 211
Anode and cathode CL (IJP)			
Pt/C	(%wt)	40%	Baseline condition
Volumetric Pt loading,	Pt_{load_V}	250 mg/cm^3	Estimated ESDLab
Cathode Pt loading,	Pt_{load_S}	0.105 mg/cm^2	Baseline condition
Anode Pt loading,	Pt_{load_S}	0.049 mg/cm^2	Baseline condition
Electrolyte loading,	$w_{electrolyte}$	30%	Baseline condition
Anode $ECSA_V$		110000 cm^2_{Pt}/cm^3_{CL}	[5]
Cathode $ECSA_V$		110000 cm^2_{Pt}/cm^3_{CL}	[5]
Thermal conductivity,	κ_{CL}	0.0027 $W/cm \cdot K$	[21]
ε_{solid}		0.3116	OpenFCST
$\varepsilon_{electrolyte}$		0.1339	OpenFCST
ε_{void}		0.5544	OpenFCST
ICCP radius		50 nm	[13]
k_{O_2} (O_2 dissolution rate)		0.001 m/s	[13] (80 ^{o}C, 50%RH)
k_{H_2} (H_2 dissolution rate)		0.1 m/s	[13] (80 ^{o}C, 50%RH)
k_{sorp}		10000 $1/s$	ESDLab
PEM (NR-211)			
Electrolyte type		Nafion	NR-211
Thermal conductivity,	κ_{PEM}	0.0013 $W/cm \cdot K$	NR-211; [21]
GDL (SGL 28BC)			
Porosity		58.73%	Estimated
Electrical conductivity (TP),	σ^{TP}_{GDL}	4.5 S/cm	[29] (SGL 28AA)
Electrical conductivity (IP),	σ^{IP}_{GDL}	210 S/cm	[29] (SGL 28AA)
Thermal conductivity (TP),	κ^{TP}_{GDL}	0.0055 $W/cm \cdot K$	[29] (SGL 28AA)
Thermal conductivity (IP),	κ^{IP}_{GDL}	0.2567 $W/cm \cdot K$	Estimated from [29]
MPL (SGL 28BC)			
Porosity		60.0%	Estimated from [5]
Electrical conductivity (TP),	σ^{TP}_{MPL}	88.4 S/cm	Black carbon prop.
Electrical conductivity (IP),	σ^{IP}_{MPL}	88.4 S/cm	Black carbon prop.
Thermal conductivity (TP),	κ^{TP}_{MPL}	0.0008 $W/cm \cdot K$	Estimated from [29]
Thermal conductivity (IP),	κ^{IP}_{MPL}	0.0387 $W/cm \cdot K$	Estimated from [29]

[1] As a reference Shukla et. al., [19], reported 4.7±1.2μm for 50%Pt/C and 0.15 mg/cm^2. Also, in [20], reported 1.76±0.29 for 20%Pt/C and 0.026 mg/cm^2.

Table A.2: Model PSD parameters.

Parameter		**Value**	**Reference**
Anode and cathode CL (IJP)			
Absolute permeability,	k_{sat}	$1.00{\cdot}10^{-14}$ cm^2	[38]
PSD interconnectivity,	λ_{PSD}	6	[1]
HI volume fraction,	F_{HI}	0.3	[1]
HI static contact angle,	ϕ_{HI}	[1]	
HO static contact angle,	ϕ_{HO}	[1]	
Characteristic:			
Pore radius,	r_i $[\mu m]$	0.02, 0.025, 0.075	[1]
Pore fraction,	f_i	0.5, 0.4, 0.1	ESDLab
Pore widths,	s_i	0.55, 0.45, 1.2	[1]
GDL (SGL 28BC)			
Absolute permeability,	k_{sat}	$4.6{\cdot}10^{-8}$ cm^2	In-house MIP
PSD interconnectivity,	λ_{PSD}	2.02	Fitted for abs. perm.
HI volume fraction,	F_{HI}	0.08	[36]
HI static contact angle,	ϕ_{HI}	70°	[36]
HO static contact angle,	ϕ_{HO}	122°	[37]
Characteristic:			
Pore radius,	r_i $[\mu m]$	14.2, 34.0	[1]
Pore fraction,	f_i	0.31, 0.69	[1]
Pore widths,	s_i	1.0, 0.35	[1]
MPL (SGL 28BC)			
Absolute permeability,	k_{sat}	$1.39{\cdot}10^{-9}$ cm^2	[35]
PSD interconnectivity,	λ_{PSD}	1.0	[1]
HI volume fraction,	F_{HI}	0.01	[1]
HI static contact angle,	ϕ_{HI}	89°	[1]
HO static contact angle,	ϕ_{HO}	110°	[1]
Characteristic:			
Pore radius,	r_i	0.072, 0.125, 2.0 μm	[1]
Pore fraction,	f_i	0.45, 0.1, 0.45	[1]
Pore widths,	s_i	0.35, 0.5, 0.9	[1]

Table A.3: Parameters and its values selected for the parametric study.

Parameter	**Original**	**1**	**2**	**3**	**4**
kO_2 $[m/s]$	0.001	0.0005	0.005	0.01	0.02
		0.00075	0.002	0.003	0.005
$ECSA_V$ $[cm^2_{Pt}/cm^3_{CL}]$	110000	50000	75000	150000	250000
p_{BT} [Pa]	5000	2000	3000	40000	-
k_{BT}	0.005	0.0005	0.0025	0.001	0.05
		0.0001	0.0002	0.0003	0.0005
Current collector/	1.0/1.0	0.83/0.82	0.5/1.0	0.1/0.5	0.5/0.5
channel width $[mm]$		1.3/1.3	0.7/0.7	0.5/1.3	0.5/1.3
k_{sorp} $[1/s]$	10000	5000	1000	500	100
		10	1.0	0.1	0.01
		40	15	7	5
ACL and CCL					
κ $[W/cm \cdot K]$	0.0027	0.0015	0.002	0.0035	0.004
		0.0003	0.0008	0.03	0.08
HI vol. fraction	0.30	0.15	0.20	0.25	0.35
HI contact angle $(^o)$	84	76	80	88	92
		82	83	85	86
HO contact angle $(^o)$	91	85	88	94	97
		89	90	92	93
GDL					
Porosity	0.5873	0.5	0.55	0.65	0.7
σ^{TP} $[S/cm]$	4.5	1.125	2.25	9	18
		0.9	1.3	1.7	23
σ^{IP} $[S/cm]$	210	105	140	315	420
κ^{TP} $[W/cm \cdot K]$	0.0055	0.00055	0.0022	0.022	0.055
		0.0009	0.001	0.0015	0.1
κ^{IP} $[W/cm \cdot K]$	0.2567	0.002	0.02	2.0	20
HI vol. fraction	0.08	0.01	0.04	0.12	0.16
HI contact angle $(^o)$	70	65	68	72	75
		60	80	-	-
HO contact angle $(^o)$	122	110	117	128	134
MPL					
Porosity	0.60	0.40	0.50	0.70	0.80
σ^{TP} $[S/cm]$	88.84	10.5	50	110	270
		0.25	0.5	1.0	2.0
σ^{IP} $[S/cm]$	88.84	10.5	50	110	270
κ^{TP} $[W/cm \cdot K]$	0.0008	0.00008	0.0004	0.0016	0.008
κ^{IP} $[W/cm \cdot K]$	0.0387	0.00387	0.01935	0.0774	0.387
HI contact angle $(^o)$	89	83	86	92	95
HO contact angle $(^o)$	110	100	105	115	120

A.1 Graphical results

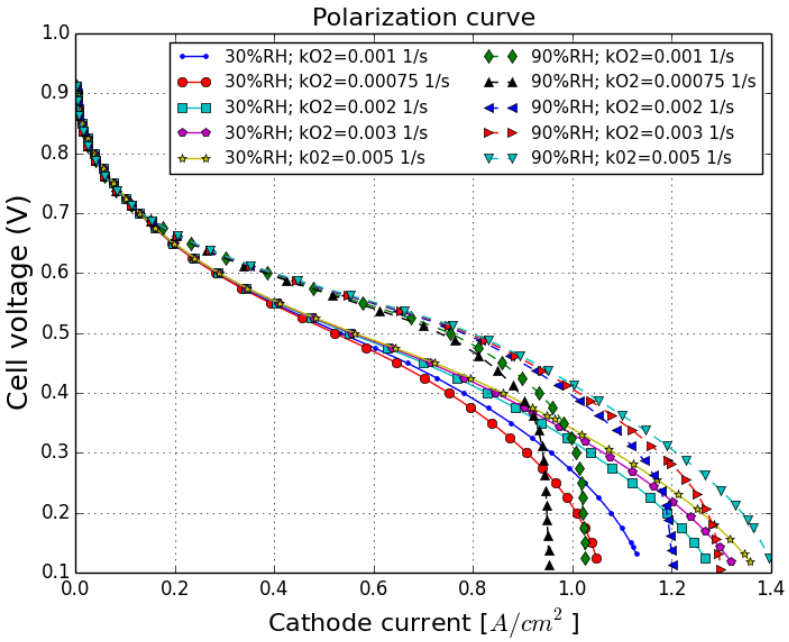

Figure A.1: Overlapped baseline polarization curves, under dry and wet operating conditions, with different kO_2 values; from 0.00075 to 0.005 1/s.

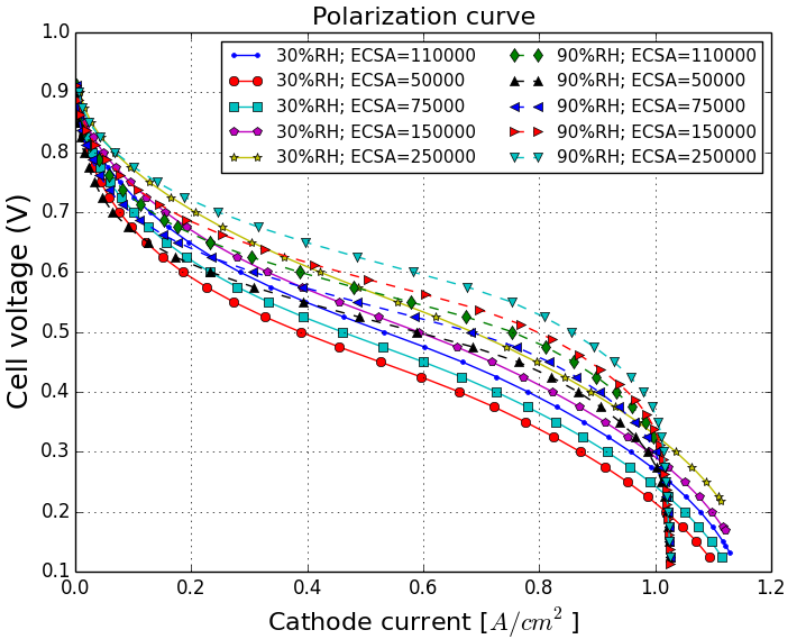

Figure A.2: Overlapped baseline polarization curves, under dry and wet operating conditions, with different ECSA values; from 50000 to 250000 cm^2_{Pt}/cm^3_{CL}.

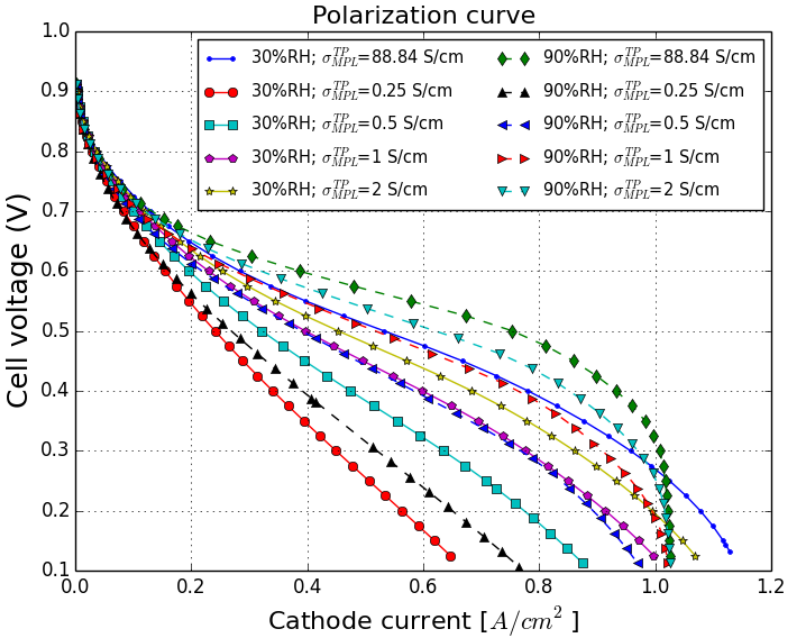

Figure A.3: Overlapped baseline polarization curves, under dry and wet operating conditions, with different MPL electrical conductivity values; from 0.25 to 2.0 S/cm .

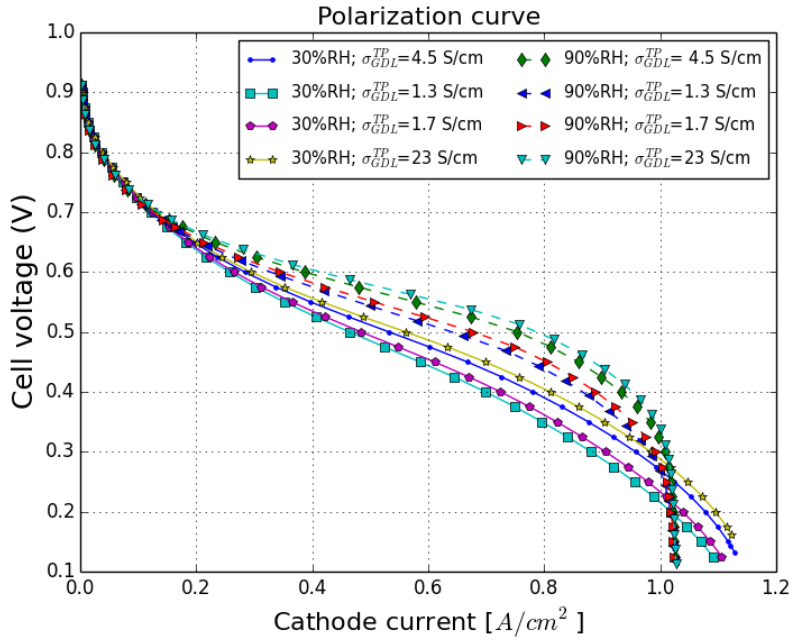

Figure A.4: Overlapped baseline polarization curves, under dry and wet operating conditions, with different GDL electrical conductivity values; from 0.9 to 23 S/cm .

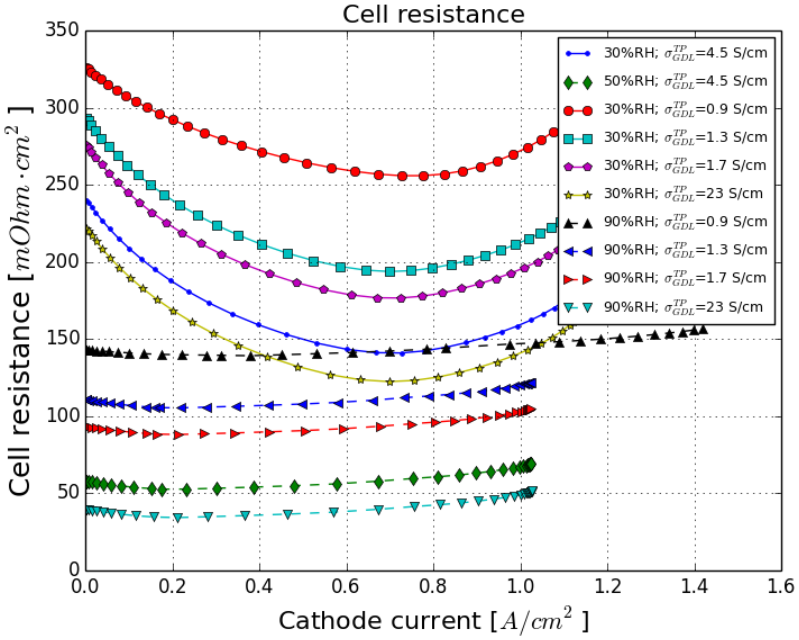

Figure A.5: Overlapped baseline cell resistance curves, under dry and wet operating conditions, with different GDL electrical conductivity values; from 0.9 to 23 S/cm .

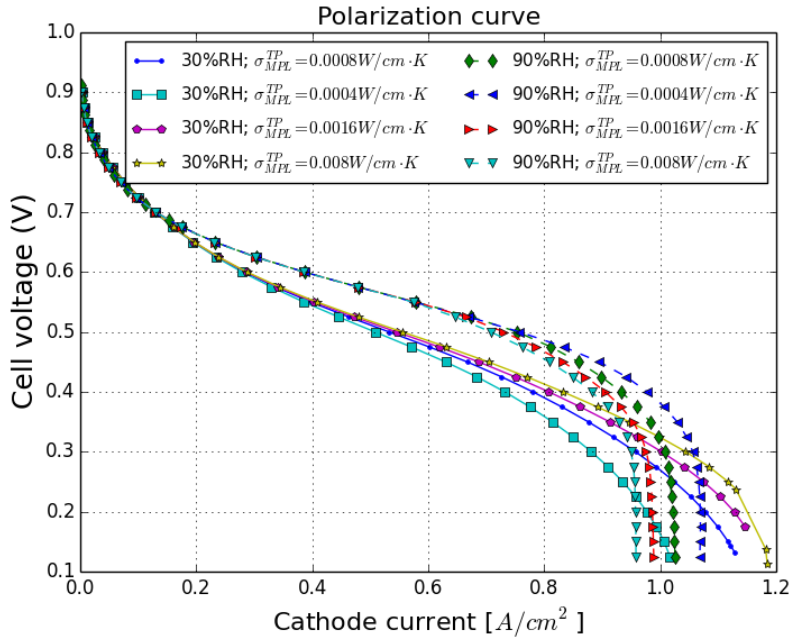

Figure A.6: Overlapped baseline polarization curves, under dry and wet operating conditions, with different MPL thermal conductivity values; from 0.0008 to 0.008 $W/cm \cdot K$.

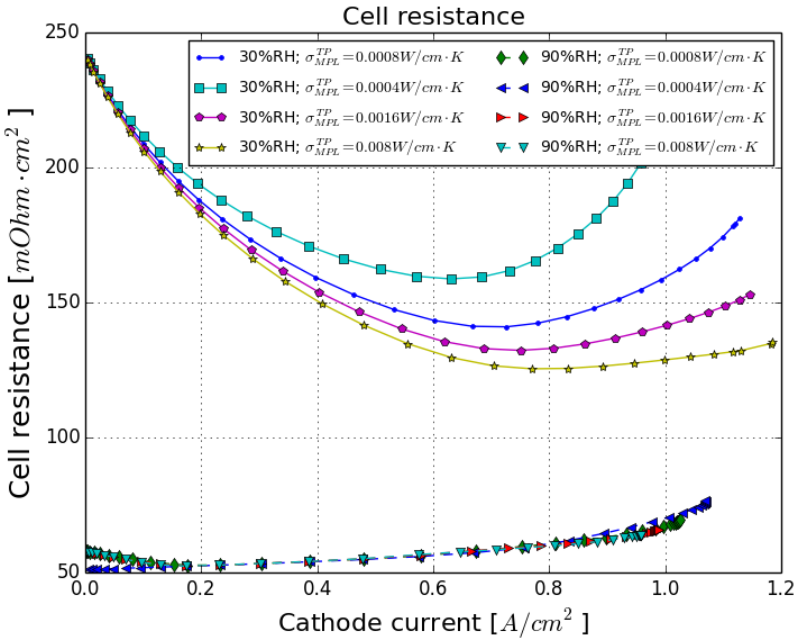

Figure A.7: Overlapped baseline cell resistance curves, under dry and wet operating conditions, with different MPL thermal conductivity values; from 0.0008 to 0.008 $W/cm \cdot K$.

Appendix B

Baseline parameters

B.1 Channel and current colector width

The bipolar plates geometry is measured with microscopy technology; see Figure B.1. Five samples of each, current collector and channel width, are measured. The samples values are shown in Table B.1.

Table B.1: Channel and current collector width values from microscopy technology measurement.

Sample	Current col. (μm)	Channel (μm)
1	816	821
2	827	821
3	829	819
4	823	817
5	838	817
AVG	**827**	**819**
STDEV	8.08	1.79

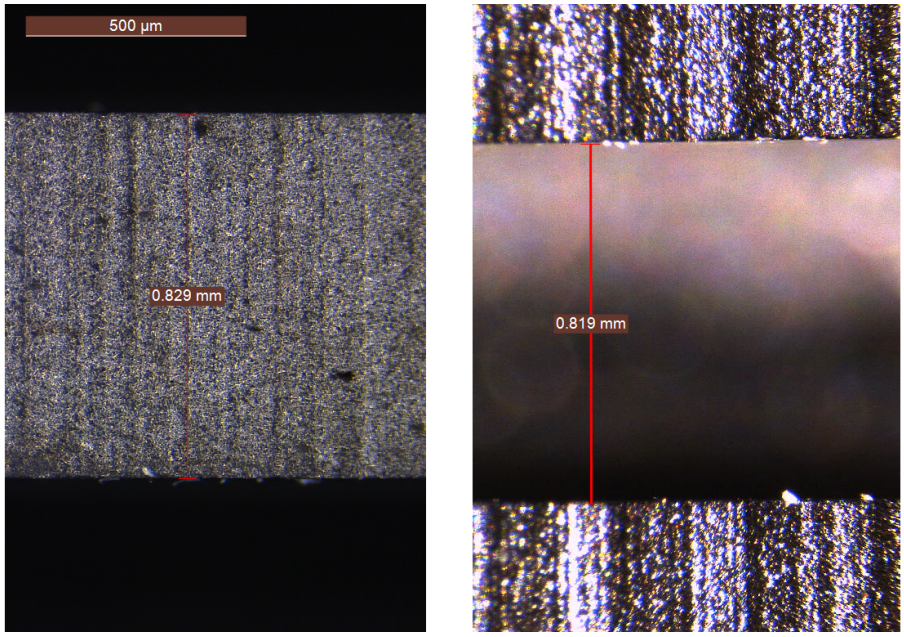

Figure B.1: Example of current collector (left) and channel (right) microscopy imaging measurement.

B.2 IJP catalyst layers volume fractions

OpenFCST compute the ink-jet printed catalyst layers volume fraction with the following equations:

$$\varepsilon_{solid} = \frac{1}{\rho_{Pt}} + \frac{(1 - Pt/C)}{Pt/C \cdot \rho_{carbon}} \cdot \frac{Pt_{load_V}}{1000} \tag{B.1}$$

$$\varepsilon_{electrolyte} = \frac{w_{electrolyte}}{(1 - w_{electrolyte})} \cdot \frac{1}{Pt/C} \cdot \frac{1}{\rho_{electrolyte}} \cdot \frac{Pt_{load_V}}{1000} \tag{B.2}$$

$$\varepsilon_{void} = 1 - \varepsilon_{solid} - \varepsilon_{electrolyte} \tag{B.3}$$

B.3 Stacked GDL thickness and porosity

As GDL properties change during the stacking process, in this section the sub-indexes $_1$ and $_2$ are used to refer before and after compression state, respectively.

B.3.1 Stacked GDL thickness

GDL and MPL thickness before stacking can be directly calculated from ESDLab MIP experiments data shown in Table 2.6:

MPL_{thk_1}= 114.7 μm,
GDL_{thk_1}= 28BC_{thk}-MPL_{thk} = 228.6 - 114.7= 113.9 μm.

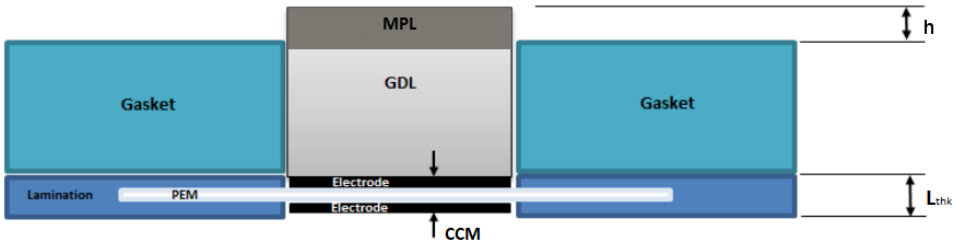

Figure B.2: ESDLab assembly configuration.

Figure B.2 shows the stack configuration before the compression. The catalyst-coated membrane is composed of polymer electrolyte membrane, anode and cathode catalyst layers. Thus, its thickness is defined as:

$$CCM_{thk} = ACL_{thk} + PEM_{thk} + CCL_{thk} = 30.4\mu m$$

The lamination thickness, L_{thk} =160 μm, is measured with microscope technology in ESDLab. The selected gasket thickness is G_{thk} = 135 μm. The GDL is assumed to be the only compressible part then, h is the GDL compressed thickness. Once all the components have been stacked and compressed, the GDL+MPL thickness is:

$$(GDL + MPL)_{thk_2} = L_{thk}/2 + G_{thk} - CCM_{thk}/2 = 160/2 + 135 - 30.4/2$$

$$(GDL + MPL)_{thk_2} = 199.8\mu m$$

As MPL thickness remains the same after stack:
GDL_{thk_2}= **85.1** μm,
MPL_{thk_2}= **114.7** μm.

B.3.2 Stacked GDL porosity

In this section, super-index ^{GDL} is suppressed in all the parameters aa all of them are referred to GDL properties.

Assuming the GDL solid volume remains constant before and after compression:

$$V_s = V_{s_1} = V_{s_2} = V_{tot_1}(1 - \varepsilon_1)$$

$$A = A_1 = A_2$$

$$V_{tot_i} = e_i A$$

$$\varepsilon_{void_2} = \frac{V_{p_2}}{V_{tot_2}} = \frac{V_{tot_2} - V_s}{V_{tot_2}} = 1 - \frac{V_s}{V_{tot_2}} = 1 - \frac{V_{tot_1}(1 - \varepsilon_{void_1})}{V_{tot_2}} = 1 - \frac{e_1 A(1 - \varepsilon_{void_1})}{e_2 A}$$

$$\varepsilon_{void_2} = 1 - (1 - \varepsilon_{void_1})\frac{e_1}{e_2} = 1 - (1 - \varepsilon_{void_1})\frac{e_1}{e_2}$$

Getting the initial values (pre-compression) from Table 2.6 and the GDL compressed thickness estimated in Section B.3.1:

$$\varepsilon_2 = 1 - (1 - 0.786)\frac{113.9}{85.1} = \mathbf{0.7135}$$

B.4 Electrochemical Active Surface Area (ECSA)

ESDLab experiments reported electrochemical active surface area values when the Pt/C is 40% and Pt loading is 0.05 and 0.1 $\frac{g_{Pt}}{cm^2_{CL}}$ in the anode and cathode, respectively. The results are reported in Table B.2.

Table B.2: Electrochemical active surface area extracted from ESDLab experiments. Pt/C=40%. Anode loading = 0.05 $\frac{g_{Pt}}{cm^2_{CL}}$. Cathode loading = 0.1 $\frac{g_{Pt}}{cm^2_{CL}}$.

Sample	$ECSA^{anode}_{mass}$ $(\frac{m^2_{Pt}}{g_{Pt}})$	$ECSA^{cathode}_{mass}$ $(\frac{m^2_{Pt}}{g_{Pt}})$
1	40.47	61.02
2	65.27	69.49
3	56.08	64.19
AVG	53.94	64.90
STDEV	12.54	4.28

Taking the averaged values from Table B.2, the electrochemical active area for the anode an cathode, ECSA_V^{anode} and $\text{ECSA}_V^{cathode}$, can be calculated with the following expression. See the results in Table B.3.

$$ECSA_V^i = \frac{ECSA_{mass}^i \cdot Pt_{load_S}^i}{CL_{thk}^i} \tag{B.4}$$

Table B.3: Electrochemical active surface area for anode and cathode based on data from Tables B.2 and 2.8.

	Anode	Cathode
$ECSA_V^i$ $(\frac{cm_{Pt}^2}{cm_{CL}^3})$	134850	162250

B.5 MPL electrical conductivity

Electrical resistance is defined as:

$$R_i = \frac{l_i}{\sigma_i \cdot S_i} \tag{B.5}$$

B.5.1 Through-plane (TP)

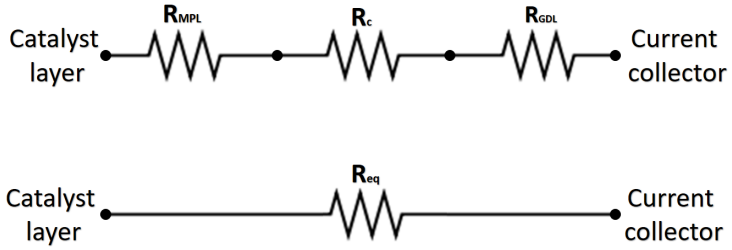

Figure B.3: Series equivalent resistance schematic for through-plane conductivity

From the schematic Figure B.3, representative of the through-plane (TP) electrical conductivity across the MPL and GDL, results equation B.6.

$$R_{eq} = R_{MPL} + R_c + R_{GDL} \tag{B.6}$$

Merging equations B.5 and B.6, the MPL through plane electrical conductivity, σ^{TP}_{MPL+c}, (containing the contact resistance between MPL and GDL) can be expressed as:

$$\sigma^{TP}_{MPL+c} = \frac{l_{MPL}}{\frac{l_{eq}}{\sigma_{eq}} - \frac{l_{GDL}}{\sigma_{GDL}}} \tag{B.7}$$

Getting the thickness values (under compression state) from Section B.3.1 as l_i and the SGL 28BC and 28BA electrical conductivity values under 1MPa from Table 2.7, the σ^{TP}_{MPL+c} can be computed as:

$$\sigma^{TP}_{MPL+c} = \frac{114.7}{\frac{199.8}{2.55} - \frac{85.1}{4.5}} = 1.93 \quad S/cm$$

B.5.2 In-plane (IP)

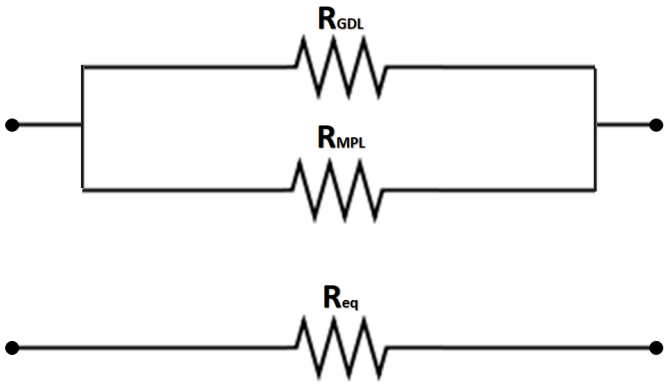

Figure B.4: Parallel equivalent resistance schematic for in-plane conductivity.

From the schematic Figure B.4, representative of the in-plane (IP) conductivity across the MPL and GDL, results the equation B.8. Note in this case there is no contact resistance.

$$\frac{1}{R_{eq}} = \frac{1}{R_{MPL}} + \frac{1}{R_{GDL}} \tag{B.8}$$

Merging equations B.5 and B.8, the MPL in-plane electrical conductivity, σ_{MPL}^{IP}, can be expressed as:

$$\sigma_{MPL}^{IP} = \frac{\sigma_{eq} l_{eq} - \sigma_{GDL} l_{GDL}}{l_{MPL}} \tag{B.9}$$

Note in the in-plane direction, l_i becomes the same between GDL and MPL. However the perpendicular section, $S = e \ x \ h$, has a different thickness value, e, for GDL and MPL. Getting the thickness values (under compression state) from Section B.3.1 as e_i and the SGL 28BC and 28BA electrical conductivity values under 1MPa reported in Table 2.7, the σ_{MPL}^{IP} can be computed:

$$\sigma_{MPL}^{IP} = \frac{190 \cdot 199.8 - 212.5 \cdot 85.1}{114.7} = 173.43 \ S/cm$$

Notice the difference between in-plane and through-plane MPL electrical conductivity should not be that big as the MPL structure is pretty isotropic. However, in this case, the through-plane MPL conductivity takes in account the contact resistance between GDL and MPL and it is probably because of that, the through-plane conductivity is much lower than in-plane one.

B.6 GDL and MPL thermal conductivity

Thermal resistance is defined as:

$$R_i = \frac{l_i}{\kappa_i A_i} \tag{B.10}$$

B.6.1 Through-plane (TP)

The same schematic, Figure B.3, used to model the electrical resistance circuit through the porous media, can be also used to model the thermal resistance circuit. Thus, from equations B.6 and B.10, MPL through-plane thermal conductivity, κ_{MPL}^{TP}, can be expressed as:

$$\kappa_{MPL}^{TP} = \frac{l_{MPL}}{\frac{l_{eq}}{\kappa_{eq}} - \frac{l_{GDL}}{\kappa_{GDL}}} \tag{B.11}$$

Getting the thickness values from Table 2.6 as l_i and the SGL 28BC and 28BA thermal conductivity values from Table 2.7, the MPL thermal conductivity under non-compressed state can be computed as:

$$\kappa_{MPL}^{TP} = \frac{114.7}{\frac{199.8}{0.006} - \frac{85.1}{0.0055}} = 0.0065\ W/cm \cdot K$$

Note that thermal conductivities are reported and calculated for non-compressed layers state. As MPL is assumed to be incompressible, its conductivity properties are not affected by the compression. In case of the GDL, it can be expected to increase the conductivity due to the porosity reduction under compression. However, Nitta et. al., [30], reported non dependence between compressed and uncompressed GDL thermal conductivity. Nevertheless, a decrease of the contact resistance is reported as the compression increase.

B.6.2 In-plane (IP)

In-plane thermal conductivity is not reported in the SIGRACET® catalog. Karimi et. al., [31], and Teertstra et. al., [32], reported values for though-plane and in-plane GDL+MPL thermal conductivity. In-plane value is roughly 11.7 times larger than through-plane. Pfrang et. al., [33], reported an IP value 12.5 times larger than TP. Therefore, the GDL+MPL in-plane thermal conductivity, κ_{eq}^{IP}, is estimated as:

$$\kappa_{eq}^{IP} = 12 \cdot \kappa_{eq}^{TP} = 0.072 W/cm \cdot K$$

In-plane MPL thermal conductivity

From Fig.11b in [34], the following relation between the MPL porosity, ε_{MPL}, and its in-plane thermal conductivity, κ_{MPL}^{IP}, has been extracted:

$$\kappa_{MPL}^{IP} = 0.01 \cdot (0.01(\varepsilon_{MPL})^2 - 0.16 \cdot \varepsilon_{MPL} + 0.81) \tag{B.12}$$

Thus, for the MPL porosity reported in Table 2.6;

$$\kappa_{MPL}^{IP}(\varepsilon_{MPL} = 0.744) = 0.0070 W/cm \cdot K$$

In-plane GDL thermal conductivity

Same Figure B.4, and therefore Equation B.8, are valid for describe the thermal conductivity through plane in the diffusion media. Merging equations B.8 and

B.10, the GDL in-plane thermal conductivity, κ_{GDL}^{IP}, can be expressed as:

$$\kappa_{GDL}^{IP} = \frac{\kappa_{eq} l_{eq} - \kappa_{MPL} l_{MPL}}{l_{GDL}} \tag{B.13}$$

Note that in the in-plane direction, l_i becomes the same between GDL and MPL. However the perpendicular section, $S = e \ x \ h$, has a different thickness value, e, for GDL and MPL. Getting the thickness values (under compression state) from Section B.3.1 as e_i, the κ_{eq}^{IP} assumed at the begging of this section and the κ_{MPL}^{IP} computed above, the κ_{MPL}^{IP} can be computed:

$$\kappa_{GDL}^{IP} = \frac{0.072 \cdot 199.8 - 0.00696 \cdot 114.7}{85.1} = 0.1597 \ W/cm \cdot K$$

Appendix C

OpenFCST parameter files

The model input parameters are organized in different parameter files, grouped by component or function. Every file is a different section in this appendix.

C.1 main

```
subsection Simulator
 set simulator name                    = meaTwoPhaseNITcapillary
 set simulator parameter file name     = data.prm
 set nonlinear solver name             = NewtonLineSearch
 set refinement method                 = AdaptiveRefinement
 set Analysis type                     = PolarizationCurve

 subsection Polarization Curve
  set Initial voltage [V] = 0.9
  set Final voltage [V] = 0.1
  set Increment [V] = 0.05
  set Min. Increment [V] = 0.01
 end
end
```

C.2 data

```
include ../../../template/data.prm

subsection Fuel cell data
 subsection Operating conditions
  set Adjust initial solution and boundary conditions  = true
  set Cathode initial oxygen mole fraction (prior to humidification) = 0.21
  set Temperature cell [K]                = 353.15 #[K]
  set Cathode pressure [Pa]               = 151325.0 #[Pa] (1.5 atm)
  set Cathode relative humidity           = 0.3
  set Anode pressure [Pa]                 = 151325.0 #[Pa] (1.5 atm)
  set Anode relative humidity             = 0.3
  set Voltage cell [V]                    = 0.6
 end

 subsection Cathode gas diffusion layer
  include ../../../template/default_GDL.prm
  set Material id = 12
 end
```

```
 subsection Cathode microporous layer
  include ../../../template/default_MPL.prm
  set Material id = 13
 end

 \# Cathode catalyst layer
 include ../../../template/cathode_CL.prm
 subsection Cathode catalyst layer
  subsection ConventionalCL
   set Active area [cm^2/cm^3] = 14:162250,  15:162250, 16:162250
  end

 \# Membrane layer
 include ../../../template/default_PEM.prm

 \# Anode catalyst layer
 include ../../../template/anode_CL.prm

 subsection Anode microporous layer
  include ../../../template/default_MPL.prm
  set Material id  = 7
 end

 subsection Anode gas diffusion layer
  include ../../../template/default_GDL.prm
  set Material id = 8
 end

 subsection Liquid Water Source Terms Equation
  set Evaporation rate constant, [mol/(Pa cm2 s)]  = 1e-4
  set Condensation rate constant [mol/(Pa cm2 s)]  = 1e-4
 end
end
```

C.2.1 /template/data

```
subsection Grid generation
 set Type of mesh = PemfcMPL
 set Initial refinement = 1
 set Sort Cuthill-McKee = false
 subsection Internal mesh generator parameters
  subsection Dimensions
   set Cathode current collector width [cm]= 0.083
   set Cathode channel width [cm]       = 0.082
   set Cathode CL thickness [cm]        = 1.25e-4, 1.25e-4, 1.25e-4
   set Cathode MPL thickness [cm]       = 1.147e-2
   set Cathode GDL thickness [cm]       = 0.851e-2
   set Membrane thickness [cm]          = 0.25e-2
   set Anode CL thickness [cm]          = 1.75e-4
   set Anode MPL thickness [cm]         = 1.147e-2
   set Anode GDL thickness [cm]         = 0.851e-2
   set Anode current collector width [cm]  = 0.083
   set Anode channel width [cm]            = 0.082
  end

  subsection Material ID
   set Cathode GDL     = 12
   set Cathode MPL     = 13
   set Cathode CL      = 14, 15, 16
   set Membrane        = 5
   set Anode CL        = 6
   set Anode MPL       = 7
   set Anode GDL       = 8
  end
```

```
  subsection Boundary ID
   set c_Ch/GDL          = 2
   set c_BPP/GDL         = 1
   set c_GDL/CL          = 255
   set c_GDL/MPL         = 255
   set c_MPL/CL          = 255
   set c_CL/Membrane     = 255
   set Membrane/a_CL     = 255
   set a_CL/GDL          = 255
   set a_CL/MPL          = 255
   set a_MPL/GDL         = 255
   set a_GDL/BPP         = 3
   set a_GDL/Ch          = 4
  end

  subsection Mesh refinement parameters
   set Initial vertical cell count               = 4
   set Horizontal division of cathode Channel    = 2
   set Horizontal division of cathode GDL        = 2
   set Horizontal division of cathode CL         = 2
   set Horizontal division of cathode MPL        = 1
   set Horizontal division of membrane           = 2
   set Horizontal division of anode MPL          = 1
   set Horizontal division of anode CL           = 1
   set Horizontal division of anode GDL          = 2
  end
 end
end

subsection System management
 set Number of solution variables = 8
 subsection Solution variables
  set Solution variable 1 = oxygen_molar_fraction
  set Solution variable 2 = water_molar_fraction
  set Solution variable 3 = protonic_electrical_potential
  set Solution variable 4 = electronic_electrical_potential
  set Solution variable 5 = membrane_water_content
  set Solution variable 6 = temperature_of_REV
  set Solution variable 7 = liquid_pressure
  set Solution variable 8 = gas_pressure
 end

 subsection Equations
  set Equation 1 = Ficks Transport Equation - oxygen
  set Equation 2 = Ficks Transport Equation - water
  set Equation 3 = Proton Transport Equation
  set Equation 4 = Electron Transport Equation
  set Equation 5 = Membrane Water Content Transport Equation
  set Equation 6 = Thermal Transport Equation
  set Equation 7 = Liquid Water Transport Equation
  set Equation 8 = Gas Transport Equation
 end
end

subsection Equations
 subsection Ficks Transport Equation - oxygen
  subsection Initial data
   set oxygen_molar_fraction = 2:0.0,3:0.0,4:0.0,5:0.0,6:0.0,7:0.0,8:0.0
  end

  subsection Boundary data
   set oxygen_molar_fraction = 2: 1.0
  end
 end

 subsection Ficks Transport Equation - water
  subsection Initial data
```

```
  set water_molar_fraction = 2:0.0,3:0.0,4:0.0,5:0.0,6:0.0,7:0.0,8:0.0
 end

 subsection Boundary data
  set water_molar_fraction = 2:1.0,4:1.0
 end
end

subsection Electron Transport Equation
 subsection Initial data
  set electronic_electrical_potential = 2:0.0,3:0.0,4:0.0,5:0.0,6:0.0,7:0.0,8:0.0
 end

 subsection Boundary data
  set electronic_electrical_potential = 1:0.0,3:0.0
 end
 subsection Boundary conditions
  set Constant Electron Current Flux Boundary Conditions = 1: -1.5
 end
end

subsection Proton Transport Equation
 subsection Initial data
  set protonic_electrical_potential = 2:0.0,3:0.0,4:0.0,5:0.0,6:0.0,7:0.0,8:0.0
 end
 subsection Boundary data
  set protonic_electrical_potential = 1:0.0
 end
end

subsection Membrane Water Content Transport Equation
 subsection Initial data
  set membrane_water_content = 2:0.0,3:0.0,4:0.0,5:0.0,6:0.0,7:0.0,8:0.0
 end

 subsection Boundary data
  set membrane_water_content = 1:0.0
 end

 subsection Boolean flags for lambda transport modes
  set Thermo-osmosis                    = true
 end
end

subsection Thermal Transport Equation
 subsection Initial data
  set temperature_of_REV = 2:0.0,3:0.0,4:0.0,5:0.0,6:0.0,7:0.0,8:0.0
 end

 subsection Boundary data
  set temperature_of_REV = 1:353.15,3:353.15
 end


 subsection Boolean flags
  set Electronic ohmic heat in GDL                = true
  set Electronic ohmic heat in MPL                = true
  set Electronic ohmic heat in CL                 = true
  set Protonic ohmic heat in CL                   = true
  set Protonic ohmic heat in ML                   = true
  set Enthalpy transport due to fickian diffusion of gases= true
  set Enthalpy transport associated with lambda transport = true
 end

 subsection Boundary conditions
  set Constant Heat Flux Boundary Conditions   =  5 : 2.5
  set Convective Heat Flux Boundary Conditions =  5 : 1.2;350
 end
```

```
 end

 subsection Liquid Water Transport Equation
  subsection Initial data
   set liquid_pressure = 2:100,3:100,4:100,5:0,6:0,7:0,8:0
  end
  subsection Boundary data
   set liquid_pressure = 4: -5e7
  end

  subsection Boundary conditions
   set Capillary pressure at GDL channel interface, [Pa]              =  151425.0
   set Breakthrough capillary pressure at GDL channel interface, [Pa] =  153425.0
   set Breakthrough phenomenon at GDL/channel interface               =  true
   set Constant capillary pressure current flux boundary conditions   =  2: 2e-3
  end
 end

 subsection Gas Transport Equation
  subsection Initial data
   set gas_pressure = 2:151325.0,3:151325.0,4:151325.0, 5:0,
               6:151325.0,7:151325.0,8:151325.0
  end

  subsection Boundary data
   set gas_pressure = 2: 151325.0, 4: 151325.0
  end

  subsection Boundary conditions
   set Gas pressure at GDL channel
               interface, [Pa] =  151325.0
  end
 end

 set Apply scaling = true
 set Equation matrix scaling = Liquid Water Transport Equation : 1e3
end

subsection Reaction Source Terms
 set Irreversible heat source due to ORR           = true
 set Irreversible heat source due to HOR           = true
 set Reversible heat source due to net reaction    = true
 set Reversible heat fraction in ORR               = 1.0
 set Water produced during ORR in vapour phase     = false
 set Water vaporization heat sink in CCL           = false
end

subsection Sorption Source Terms
 set Heat source/sink due to sorption/desorption   = true
 set Water soption time constant [1/s]                    = 500
end

subsection Discretization
 set Element = FESystem[FE_Q(2)^8 ]
 set Boundary fluxes = true
 set Interior fluxes = false

 subsection Matrix
  set Quadrature cell = -1
  set Quadrature face = -1
 end

 subsection Residual
  set Quadrature cell = -1
  set Quadrature bdry = -1
  set Quadrature face = -1
 end
end
```

```
subsection Initial Solution
 set Output initial solution              = false
 set Output solution for transfer         = false
 set Read in initial solution from file   = false
end

subsection Newton
 set Assemble threshold = 0.0
 set Debug level        = 0
 set Debug residual     = false
 set Debug solution     = false
 set Debug update       = false
 set Max steps          = 40
 set Reduction          = 1.e-8
 set Tolerance          = 1.e-8

 set Line search = false
 set Initial Overrelaxation = 0.075
 set Number of iterations with overrelaxation = 10
end

subsection Adaptive refinement
 set Refinement         = adaptive
 set Number of Refinements                = 2
 set Output initial mesh                  = false
 set Output intermediate solutions        = false
 set Output intermediate responses        = false
 set Output final solution                = true
 set Refinement threshold                         = 0.2
end

subsection Output Variables
 set Compute boundary responses = true
 set num_output_vars      = 16
 set Output_var_0         = current
 set Output_var_1         = max_temperature
 set Output_var_2         = anode_current
 set Output_var_3         = water_cathode
 set Output_var_4         = water_anode
 set Output_var_5         = Liquid_water_produced
 set Output_var_6         = Evaporated_water
 set Output_var_7         = Condensed_water
 set Output_var_8         = liquid_water_exit_cathode
 set Output_var_9         = liquid_water_exit_anode
 set Output_var_10         = vapour_water_exit_cathode
 set Output_var_11        = vapour_water_exit_anode
 set Output_var_12        = electron_ohmic_heat
 set Output_var_13        = proton_ohmic_heat
 set Output_var_14        = Evaporated_water_GDL
 set Output_var_15        = Condensed_water_GDL
end

subsection Output
 subsection Data
  set Output format      = vtk
 end

 subsection Grid
  set Format             = eps
 end
end
```

C.2.2 /template/defeault_GDL

```
set Gas diffusion layer type  = DesignFibrousGDL
subsection Generic data
 set Porosity = 0.7135
 set Use Bosanquet approx. = false
 set PSD is used in porous media = true
end

subsection PSD parameters
 subsection BasePSD
  set psd type = DualPSD
  set Gamma = 0.063
  set lambda = 1.605
  set Volume fraction Hydrophilic = 0.08
  set Volume fraction Hydrophobic = 0.92
   subsection HIPSD
    set Hydrophilic Mode probability global           = 0.214, 0.492, 0.294
    set Hydrophilic Mode characteristic radius global = 0.748e-6 , 29.2e-6, 49.5e-6
    set Hydrophilic Mode width global                 =  0.455, 2.354, 0.367
    set Static Contact Angle HI                       = 70
   end
   subsection HOPSD
    set Hydrophobic Mode probability global           = 0.214, 0.492, 0.294
    set Hydrophobic Mode characteristic radius global = 0.748e-6 , 29.2e-6, 48.5e-6
    set Hydrophobic Mode width global                 = 0.455, 2.354, 0.367
    set Static Contact Angle HO                       = 122
  end
 end
end

subsection DesignFibrousGDL
 set Porosity                                        = 0.7135
 set Anisotropic transport                           = true
 set Method effective transport properties in pores  = Gostick
 set Method effective transport properties in solid  = Percolation

 set Porosity threshold X                            = 0.118
 set Porosity network constant X                     = 3.5
 set Porosity gamma network constant X               = 0.0

 set Electrical conductivity X [S/cm]                = 1.3
 set Solid network threshold X                       = 0.0
 set Solid network constant X                        = 1.5

 set Porosity threshold Y                            = 0.118
 set Porosity network constant Y                     = 2.5
 set Porosity gamma network constant Y               = 0.0

 set Electrical conductivity Y [S/cm]                = 212.5
 set Solid network threshold Y                       = 0.0
 set Solid network constant Y                        = 1.0

 set Method effective thermal conductivity           = Given
 set Thermal conductivity X [W/(cm-K)]               = 0.0055
 set Thermal conductivity Y [W/(cm-K)]               = 0.1597

end
```

C.2.3 /template/defeault_MPL

```
set Micro porous layer type                  = DesignMPL
set Material id                              = 80
subsection Generic data
 set Porosity = 0.744
 set PSD is used in porous media = true
 set Use Bosanquet approx. = true
```

```
end

subsection PSD parameters
 subsection BasePSD
  set psd type = DualPSD
  set Gamma = 0.063
  set lambda = 0.227
  set Volume fraction Hydrophilic = 0.01
  set Volume fraction Hydrophobic = 0.99
  subsection HIPSD
   set Hydrophilic Mode probability global = 1
   set Hydrophilic Mode characteristic radius global = 5.25e-8
   set Hydrophilic Mode width global =  0.
   set Static Contact Angle HI = 84
  end
  subsection HOPSD
   set Hydrophobic Mode probability global = 1
   set Hydrophobic Mode characteristic radius global = 5.25e-8
   set Hydrophobic Mode width global = 0.606
   set Static Contact Angle HO = 115
  end
 end
end

subsection DesignMPL
 set Porosity                                  = 0.744
 set Anisotropic transport                     = true

 set Method effective transport properties in pores = Percolation
 set Porosity threshold X                      = 0.118
 set Porosity network constant X               = 2.0
 set Porosity threshold Y                      = 0.118
 set Porosity network constant Y               = 2.0

 set Method effective transport properties in solid phase= Given
 set Electric conductivity X                   = 0.5
 set Fibre network threshold X                 = 0.118
 set Fibre network constant X                  = 2.0
 set Electric conductivity Y                   = 173.43
 set Fibre network threshold Y                 = 0.118
 set Fibre network constant Y                  = 2.0

 set Method effective thermal conductivity     = Given
 set Thermal conductivity X                    = 0.0065
 set Thermal conductivity Y                    = 0.0070
end
```

C.2.4 /template/defeault_PEM

```
subsection Membrane layer
 set Material id              = 5
 set Electrolyte type         = Nafion

 subsection Materials
  subsection Nafion
   set Henry's Law Constant for Oxygen [Pa cm3/mol]    = 3.1664e10
   set Henry's Law Constant for Hydrogen [Pa cm3/mol]  = 6.69e10
   set Method to compute proton conductivity           = NRE211
   set Method to compute water diffusion               = Motupally
   set Electro-osmotic drag method                     = Springer
   set Method for sorption isotherm                    = Liu09
   set Method to compute enthalpy of sorption of water = Constant
   set Enthalpy of sorption of water [J/mol]           = 45000.0
  end
 end
```

```
 set Membrane layer type       = NafionMembrane
 subsection NafionMembrane
  set Method effective thermal conductivity    = Given
  set Thermal conductivity, [W/(cm K)]         = 0.0013
 end
end
```

C.2.5 /template/anode_CL

```
subsection Anode catalyst layer
 set Material id              = 6
 set Catalyst type            = Platinum
 set Catalyst support type    = CarbonBlack
 set Electrolyte type         = Nafion
 set Kinetics type            = DualPathKinetics

 subsection Generic data
  set Porosity = 1e20
  set Use Bosanquet approx. = true
  set PSD is used in porous media = true
 end

 subsection PSD parameters
  subsection BasePSD
   set psd type = DualPSD
   set Gamma = 0.063
   set lambda = 2.35
   set Volume fraction Hydrophilic = 0.3
   set Volume fraction Hydrophobic = 0.7
   subsection HIPSD
    set Hydrophilic Mode probability global           = 1.0
    set Hydrophilic Mode characteristic radius global = 20e-9
    set Hydrophilic Mode width global                 = 0.55
    set Static Contact Angle HI                       = 81.5
   end
   subsection HOPSD
    set Hydrophobic Mode probability global           = 0.65, 0.28, 0.07
    set Hydrophobic Mode characteristic radius global = 20e-9, 25e-9, 75e-9
    set Hydrophobic Mode width global                 = 0.55, 0.45, 1.2
    set Static Contact Angle HO                       = 92.5
   end
  end
 end

 subsection Materials
  subsection Platinum
   set Reference hydrogen concentration (HOR) = 0.59e-6
  end
  subsection CarbonBlack
   set Density [g/cm3]                         = 1.65
  end
  subsection Nafion
   set Henry's Law Constant for Oxygen [Pa cm3/mol]  = 3.1664e10
   set Henry's Law Constant for Hydrogen [Pa cm3/mol]= 6.69e10
   set Method to compute proton conductivity         = Iden11
   set Method to compute water diffusion             = Motupally
   set Electro-osmotic drag method                   = Constant
   set Electro-osmotic drag coefficient              = 1.0
   set Method for sorption isotherm                  = Liu09
   set Method to compute enthalpy of sorption of water = Constant
   set Enthalpy of sorption of water [J/mol]         = 45000.0
  end
 end
```

```
 set Catalyst layer type              = MultiScaleCL
 subsection ConventionalCL
  set Platinum loading on support (%wt)                    = 6:0.40
  set Platinum loading per unit volume (mg/cm3)            = 6:280
  set Electrolyte loading (%wt)                            = 6:0.30
  set Method to compute active area                        = given
  set Active area [cm2/cm3]                                = 6:134850
  set Method effective transport properties in pores       = Percolation
  set Porosity threshold                                   = 0.25
  set Porosity network constant                            = 1.3
  set Porosity gamma network constant                      = 0.0
  set Method effective transport properties in solid phase = Percolation
  set Solid network threshold                              = 0.118
  set Solid network constant                               = 2.0

  set Method effective transport properties in electrolyte phase = Iden11
  set Electrolyte network threshold                                = 0.0
  set Electrolyte network constant                                 = 2.0
  set Method effective thermal conductivity                        = Given
  set Thermal conductivity, [W/(cm K)]                             = 6:0.0027
 end

 subsection MultiScaleCL
  subsection MicroScale
   set Microscale type = ICCP
   subsection ICCP
    set Radius [nm] = 50
    set Non Equilibrium BC Rate constant = 0.1
    set Use non equilibrium BC = true
   end
  end
 end
end
```

C.2.6 /template/cathode_CL

```
subsection Cathode catalyst layer
 set Material id            = 14, 15, 16
 set Catalyst type          = Platinum
 set Catalyst support type  = CarbonBlack
 set Electrolyte type       = Nafion
 set Kinetics type          = DoubleTrapKinetics

 subsection Generic data
  set Porosity = 0.52
  set Use Bosanquet approx. = true
  set PSD is used in porous media = true
 end

 subsection PSD parameters
  subsection BasePSD
   set psd type = DualPSD
   set Gamma = 0.063
   set lambda = 2.35
   set Volume fraction Hydrophilic = 0.3
   set Volume fraction Hydrophobic = 0.7
   subsection HIPSD
    set Hydrophilic Mode probability global          = 0.65
    set Hydrophilic Mode characteristic radius global = 20e-9
    set Hydrophilic Mode width global                = 0.55
    set Static Contact Angle HI                      = 81.5
   end
   subsection HOPSD
    set Hydrophobic Mode probability global          = 0.65, 0.28, 0.07
    set Hydrophobic Mode characteristic radius global = 20e-9, 25e-9, 75e-9
```

```
    set Hydrophobic Mode width global                  = 0.55, 0.45, 1.2
    set Static Contact Angle HO                        = 92.5
   end
  end
 end

 subsection Materials
  subsection Platinum
   set Method for kinetics parameters (ORR) = Double_trap
  end
  subsection CarbonBlack
   set Density [g/cm3]                        = 1.65
  end
  subsection Nafion
   set Henry's Law Constant for Oxygen [Pa cm3/mol]    = 3.1664e10
   set Henry's Law Constant for Hydrogen [Pa cm3/mol]  = 6.69e10
   set Method to compute proton conductivity           = Iden11
   set Method to compute water diffusion               = Motupally
   set Electro-osmotic drag method                     = Constant
   set Electro-osmotic drag coefficient                = 1.0
   set Method for sorption isotherm                    = Liu09
   set Method to compute enthalpy of sorption of water = Constant
   set Enthalpy of sorption of water [J/mol]           = 45000.0
  end
 end

 subsection Kinetics
  subsection DoubleTrapKinetics
   set Reference prefactor, [A/cm2] = 1600.0
  end
 end

 set Catalyst layer type   = MultiScaleCL
 subsection ConventionalCL
  set Platinum loading on support (%wt)         = 14:.40, 15:.40, 16:.40
  set Platinum loading per unit volume (mg/cm3) = 14:280, 15:280, 16:280
  set Electrolyte loading (%wt)                 = 14:0.30, 15:0.30, 16:0.30
  set Method to compute active area             = given

  set Method effective transport properties in pores  = Percolation
  set Porosity threshold                              = 0.25
  set Porosity network constant                       = 1.3
  set Porosity gamma network constant                 = 0.0

  set Method effective transport properties in solid phase = Percolation
  set Solid network threshold                                = 0.118
  set Solid network constant                                 = 2.0

  set Method effective transport properties in electrolyte phase = Iden11
  set Electrolyte network threshold                                = 0.0
  set Electrolyte network constant                                 = 2.0

  set Method effective thermal conductivity = Given
  set Thermal conductivity, [W/(cm K)]      = 14:0.0027, 15:0.0027, 16:0.0027
  set Effective saturation                  = false
 end

 subsection MultiScaleCL
  subsection MicroScale
   set Microscale type = ICCP
   subsection ICCP
    set Radius [nm] = 50
    set Non Equilibrium BC Rate constant = 0.001
    set Use non equilibrium BC = true
   end
  end
 end
end
```